7.11 Use of Hyperspectral Infrared Radiances to Infer Atmospheric Trace Gases

C Crevoisier, CNRS-LMD, Ecole polytechnique, Palaiseau Cedex, France

7.11.1 Introduction

For the past three decades, satellite observations have provided a continuous survey of the state of the atmosphere. Current space-borne instruments deliver essential observations to weather forecasting models, contribute to climate assessment, and monitor rapid changes in stratospheric and tropospheric compositions. Among the various satellite-borne instruments that can provide information on the composition and state of the atmosphere (such as UV–visible instrument, short-wave infrared spectrometers, etc.), thermal infrared sounders flying onboard polar-orbiting satellites in Low-Earth Orbit (LEO) have been used since the early days of Earth observation from space.

Since 1978, the TOVS (TIROS-N Operational Vertical Sounder) system has carried the infrared sounder HIRS (High-Resolution Infrared Sounder) onboard the successive NOAA polar platforms. Covering the thermal infrared spectral region with 19 channels characterized by a spectral resolution of 10–20 cm^{-1} for long-wave channels, this first generation of infrared sounders has been essential to numerical weather prediction. Alongside the retrieval of temperature and water vapor profiles, as well as surface temperature, and cloud properties, these instruments have also given information on a few greenhouse gases (Chédin et al., 2002, 2003b). Concentration measurements based on infrared Fourier transform spectroscopy have been performed using ground-based (e.g., De Maziere et al., 1999), balloon-borne (e.g., Té et al., 2002), and airborne experiments (e.g., Worden et al., 1997), which were characterized by a much higher spectral resolution. Following several pioneering research studies (Smith et al., 1991; Wetzel et al., 1995; Chédin et al., 2003a), the advent of a new generation of infrared sounders characterized by a very high spectral resolution (one hundred or a thousand times higher than for HIRS) has enabled the retrieval of a whole series of trace gases, including greenhouse gases, while improving the thermodynamic characterization of the atmosphere and study of clouds and aerosols. Several instruments such as correlation radiometers, spectrometers, or interferometers have now all flown successfully onboard space-based platforms.

In particular, since the late 1990s, hyperspectral infrared missions have been flying in polar orbit with various spectral, radiometric, and geometric characteristics: IMG onboard ADEOS (1996–1997), AIRS onboard Aqua (since 2002), TES onboard AURA (since 2004), and CrIS onboard Suomi-NPP (since 2011), which form the US Earth Observing System afternoon constellation of satellites; the two IASI instruments onboard the European Metop suite of midmorning satellites (Metop-A since 2006 and Metop-B since 2012); TANSO-FTS on the Japanese GOSAT platform (since 2009); and finally the 2 limb-viewing instruments MIPAS onboard the European EnviSat platform (2002–2012) and ACE-FTS onboard the Canadian SciSat platform (since 2003).

Hyperspectral infrared sounders measure the thermal radiation emitted by the Earth's surface and atmosphere in terms of radiance spectra that exhibit signatures associated with spectroscopic absorption/emission lines of molecules located along the optical path between the Earth's surface and the satellite detectors. From these spectral signatures, geophysical data can be retrieved using numerical inverse methods. Performing atmospheric remote sensing in the thermal infrared spectral domain offers many advantages. First, several atmospheric species can only be observed in this spectral range. Second, observations in the thermal infrared can be made during both day and night. Therefore, as opposed to observations made in the ultraviolet, visible, or short-wave infrared spectral regions, diurnal cycles of various atmospheric and surface variables can be measured. Third, vertical information can be retrieved from the observations. This is due to the fact that atmospheric temperature drives the processes of absorption and emission of infrared radiation by molecules, through Planck's law and the dependency to temperature of the population of the molecular energy levels.

Several categories of geophysical variables can be retrieved from observations in the thermal infrared: thermodynamic variables (temperature and water vapor profiles), surface characteristics (surface temperature and spectral emissivity), clouds, aerosols, and trace gases. Among the latter, a distinction can be made between greenhouse gases, also called climate gases (CO_2, N_2O, CH_4, CFC11, CFC12, HCFC22), and chemical reactive gases, that may also be important for climate (O_3, CO, HNO_3, OCS, SO_2, NO_2, SF_6, HOCl, H_2O_2, etc.).

To be either detected or retrieved from space, a molecule needs to have a spectral signature within the spectral range covered by the instrument and to have a sufficient atmospheric concentration. The latter depends on the sources and sinks (both natural and anthropogenic) of each species, whose balance ultimately drives their concentration. It is subject to variations, both geographically and vertically, in relation with the spatiotemporal distribution of sources and sinks, and atmospheric circulation. Atmospheric gases range from those that are constant or predictable in time to those that are variable and unpredictable. Greenhouse gases that are influenced by human activities (CO_2, CH_4, N_2O, CFCs) are usually well-mixed gases, with slowly varying concentrations. On the contrary, water vapor varies enormously in time and space. In between, ozone and other trace gases are intermediate to varying degrees.

For long-lived atmospheric species, such as greenhouse gases, highly accurate measurements of the mixing ratios are made by ground stations around the globe and enable the monitoring of background gas amounts. However such networks are sparse.

With dense spatial and temporal sampling, satellite measurements of the distribution of global atmospheric greenhouse gas concentration can improve our knowledge of both natural and anthropogenic surface fluxes. The required precision is nonetheless very high since the trends as well as the diurnal, synoptic, seasonal, and interannual variations are two orders of magnitude lower than the background levels. The challenge for the remote sensing of long-lived gases from space is thus to retrieve data products that have sufficient precision and accuracy.

For short-lived species and species having sources that exhibit strong spatial and temporal variability, the global measurement of constituents from remote-sounding instrumentation onboard-orbiting space-based platforms provides a unique opportunity to monitor atmospheric pollution and biogeochemical cycles. Recent studies have shown that by exploiting weak absorption lines observed in radiance spectra measured in the thermal infrared by the IASI instrument, it is possible to retrieve total columns of low abundant gases such as sulfur dioxide, ammonia, methanol, or formic acid. It is especially the case when special events happen, such as volcanic eruption, large fires, and pollution events, for which a series of molecules can be retrieved simultaneously (e.g., Clarisse et al., 2011).

This chapter focuses on the retrieval of atmospheric trace gases. However, since the uncertainty on the retrieved gas contents depends first on that of thermodynamics variables (temperature and water vapor profiles, as well as surface temperature and spectral emissivity), and to a lower extend on the aerosol absorption contribution, some information is also presented for these variables. "Remote Sensing in the Thermal Infrared Region" section describes the general principle of remote sensing in the thermal infrared region, together with the typical instruments used to perform the measurements. "Analysis of Spectral Signatures of Trace Gases in the Thermal Infrared" section focuses on the spectral signatures of trace gases in the observations made in the thermal infrared. Based on the forward computation of atmospheric transmission and spectral radiances, this section introduces the radiative transfer models that are then used to study the sensitivity of hyperspectral infrared instruments to variations of gas mixing ratios along the atmospheric column. "Inverse Radiative Transfer" section presents the general retrieval procedures that are used to interpret the measured spectra in terms of gas abundance. Finally, "Gas Retrieval Accuracy" section describes the impact of the spectral and radiometric characteristics of the instruments on the accuracy of the retrieved variables and presents typical validation procedures of the retrieved quantities.

7.11.2 Remote Sensing in the Thermal Infrared Region

7.11.2.1 The Thermal Infrared Domain

Thermal infrared corresponds to the spectral region from about 100–3000 cm^{-1} (about 3–100 μm). In this spectral range, radiation from the Earth is emitted during both day and night, which provides observations throughout the whole day. Thermal infrared is also a part of the solar spectrum and can thus be exploited for satellite measurements that operate in solar occultation mode.

While going through the atmosphere, thermal infrared radiation is absorbed or emitted by atmospheric constituents. The emission spectrum of the Earth's atmosphere contains many spectral features due to the different molecules that absorb and emit radiation. Fig. 1 shows the spectral distribution of radiance in terms of wavenumber and the equivalent brightness temperature that could be measured at the top of the atmosphere. The envelope of the emission spectrum is very close to the spectrum that would be emitted by a black body with a temperature of 300 K, which is close to the average surface temperature of the Earth.

The main absorption features in the thermal infrared spectral range are associated with rotational transition lines related to the fundamental vibrational bands of H_2O, CO_2, O_3, N_2O, CH_4, and CO. Rotational–vibrational transitions particularly lead to a change of the molecular dipole moment upon absorption or emission of radiation. Due to the vertical variability of the temperature profile in the atmosphere, the observed spectrum is a superposition of all these processes at different altitudes, which make the computation and analyze of infrared atmospheric spectra challenging.

In the thermal infrared, most polyatomic molecules (e.g., H_2O, CO_2, O_3, N_2O, CH_4, NO_2, HNO_3, OCS, SO_2, etc.) and heteronuclear diatomic molecules (e.g., CO, HCl, etc.) exhibit strong absorption and emission. On the contrary, homonuclear diatomic molecules like N_2 or O_2 do not show strong spectral features in this spectral range. However, broad-band features such as pressure-induced absorption or emission (that are especially important for N_2, O_2, and CO_2) and absorption continua of N_2, O_2, and H_2O (see "Radiative transfer forward codes" section) exist and need to be taken into account when interpreting infrared spectra.

7.11.2.2 Classification of Trace Gases

Atmospheric species that absorb radiation in the thermal infrared can be divided into four categories, depending on both their infrared absorption and their atmospheric variability (which is linked to surface and atmospheric sources and sinks as well as atmospheric lifetimes).

Species combining low spatial and temporal atmospheric variabilities (associated with long atmospheric lifetimes) and high infrared absorptions (associated with high current concentration levels and intense absorptions in the infrared) are often referred to as greenhouse gases or climate gases. They include CO_2, N_2O, and CH_4. The former two present the lowest atmospheric variability. Their retrieval is challenging since their small signal variabilities have to be retrieved from larger signal contributions. Therefore, a high accuracy, defined by trueness and precision, of the retrieved variable is required for climate research (Keith et al., 2001). For infrared sounders, the trueness, which can be defined as the deviation of the retrieved gas concentration from

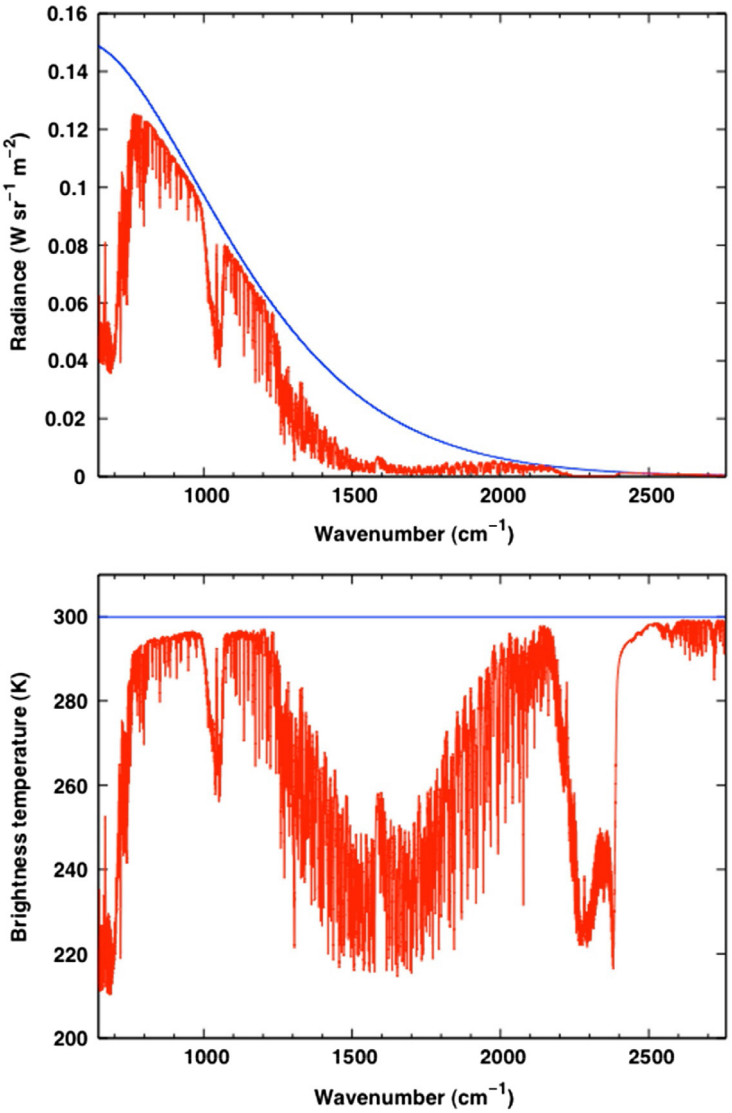

Fig. 1 Top: Spectral distribution of radiance in terms of wavenumber at the top of the atmosphere for a spectral resolution of 0.005 cm^{-1}. Also shown in blue is the radiance of a black body at 300 K computed using the Planck equation. Bottom: Spectral distribution of the equivalent brightness temperature.

the true value, is mostly associated with the uncertainty on the spectroscopic parameters, whereas the precision, which is the random error associated to the retrieval, is mostly associated with the radiometric noise and spectral resolution of the instrument, as well as with the underlying assumptions on the atmospheric state in the retrieval process.

Species combining high spatial and temporal atmospheric variabilities (associated with short atmospheric lifetimes) and high infrared absorptions (associated with high current concentration levels and intense absorptions in the infrared) are especially important for pollution monitoring and atmospheric chemistry. They include CO, tropospheric O_3, and volcanic SO_2. As compared to greenhouse gases, the instrument accuracy can be relaxed for these species, but the temporal coverage is extremely important because of the high temporal variability.

Species combining high spatial and temporal atmospheric variabilities (associated with short atmospheric lifetimes) and low infrared absorptions (associated with low current concentration levels and/or limited absorption bands in the infrared) are also important for pollution monitoring and atmospheric chemistry. For nadir instrument, they can only be detected when high atmospheric abundances occur, or for specific conditions such as high thermal contrasts (see "Retrievals in the Boundary Layer" section). They include HNO_3, NO_2, NH_3, SO_2, PAN, VOC.

Species combining low spatial and temporal atmospheric variabilities (associated with long atmospheric lifetimes) and low infrared absorption (associated with low current concentration levels) are characterized by weak spectral signature (CFCs, OCS, etc.). The question is then the possibility to detect their signatures given the instrument specifications.

7.11.2.3 Principle

An instrument operating in the thermal infrared spectral range measures the light passing through different atmospheric layers. From the measured radiance spectrum, it is thus possible to extract information on the vertical concentration of each atmospheric constituent absorbing at a given altitude. Two viewing geometries can be used: (i) nadir viewing, with instrument looking down from space toward the nadir direction and scanning across the satellite track (generally up to ± 50 degrees). Examples of hyperspectral infrared sounders using this geometry include IMG, AIRS, IASI, TANSO-FTS, CrIS, and IASI-NG (see "Measurement Techniques" section); (ii) limb-viewing, with instrument observing the limb at different tangent altitudes from which vertical trace gas concentration profiles can be inferred. Examples of hyperspectral infrared instruments using this geometry include MIPAS and ACE-FTS. The viewing geometry directly impacts the characteristics of the retrieved variables.

Nadir-viewing thermal infrared instruments can measure the atmospheric radiation down to the ground, when neither cloud nor aerosol is located in the radiation pathway ("clear-sky" situation). Provided that the spectral resolution is high enough, some vertical information can be derived from the shape of the absorption lines. The amount of vertical information that can be retrieved for a given species, which is characterized by an uneven sensitivity to the atmospheric layers, depends on the instrumental characteristics (spectral resolution and radiometric noise) as well as on the thermal contrast between the surface and the boundary layer, which determines to what extent species can be detected near the surface (see "Retrievals in the Boundary Layer" section). **Fig. 2** shows spectra of brightness temperatures for a typical tropical situation computed using the spectral resolution and coverage of various hyperspectral infrared sounders described in "Measurement Techniques" section. The difference in spectral resolution and spectral coverage of these instruments is well seen in **Fig. 2**.

Limb-viewing instruments that observe the atmosphere along tangential optical paths provided extremely high sensitivity to trace constituents due to the long atmospheric paths and provide excellent vertical resolution of the order of a few kilometers, thus much better than what can be achieved with nadir sounding instruments. However, due to the path geometry in the atmosphere, the horizontal resolution is limited: limb-viewing instruments provide information in the middle and upper atmosphere where general transparency is high, but give limited or no information at lower altitude (typically below 5 km), due to the presence in the light path of strong absorbers, such as water vapor for which most of the atmospheric burden in present in the troposphere, or also of clouds and heavy aerosols. Interpreting limb-viewing observations in terms of atmospheric variables requires accurate knowledge of instrument pointing parameters (tangent heights) and pressure/temperature vertical profiles. Temperature and tangent heights can be viewed as independent parameters, whereas pressure can be calculated from temperature and altitude by using the hydrostatic equilibrium equation. Reactive trace gases are the usual target species of limb-viewing instruments, so pointing parameters are simultaneously retrieved with pressure and temperature by the analysis of properly selected gas absorption lines.

Hyperspectral infrared instruments generally allow measurements to be made with a global coverage on long time scales for several species at the same time and location. The main drawbacks are: (i) the viewing geometry that provides either a weighted integral of atmospheric properties along the optical path with limited vertical resolution (nadir-viewing) or a limited spatial coverage with few information in the mid-low troposphere (limb-viewing); (ii) the low revisit time (2 times per day) for a given location, which restricts the usefulness for chemically reactive species. This last drawback could be overcome by an infrared sounder placed on a geostationary (GEO) orbit, such as the future InfraRed Sounder (IRS) on MeteoSat Third Generation (MTG) (Tjemkes, 2016).

7.11.2.4 Measurement Techniques

Two main concepts of passive remote sensors using the Earth's thermal emission as a source have demonstrated their ability to provide measurements of atmospheric key species: dispersing spectrometers and Fourier transform infrared interferometers. The design and technical specifications (spectral range, spectral resolution, footprint on the ground, scanning mode) of each instrument are optimized as a function of the scientific objectives to be achieved during the mission.

7.11.2.4.1 Dispersive spectrometer

A dispersive spectrometer aims at optically dispersing incoming radiation into its spectral components in order to generate a spectrum (**Fig. 3**). Common dispersive elements include prisms and gratings. Arrangements of several detectors in a line can be used to record the disperse light on the focal plane. Multiaperture array grating spectrometers provide high spectral resolution with wide spectral coverage, using advanced imaging design, with wide spectral coverage. Upwelling radiance enters the system via a cross-track scan mirror, where it is directed into a telescope. The collimated energy exiting the telescope is incident on the spectrometer entrance slit plane containing individual apertures. Ultimately, these slits are imaged onto the focal plane, where each slit image contains the energy from one selected grating order.

7.11.2.4.2 Fourier transform infrared spectrometer

Fourier transform infrared (FTIR) spectrometers collect the thermal infrared radiation emitted from the Earth-atmosphere system and splits it into two beams by a half-transparent mirror called a beam-splitter (**Fig. 4**). The beams travel different optical paths, are reflected on moving mirrors, and are then combined again. This combination of two shifted coherent waves produces interferences. The interferogram is the measure of these interferences that vary with the Optical Path Difference (OPD) stemming from the time delay between the 2 beams. The overall intensity of the light is thus measured at different time delay settings. From the

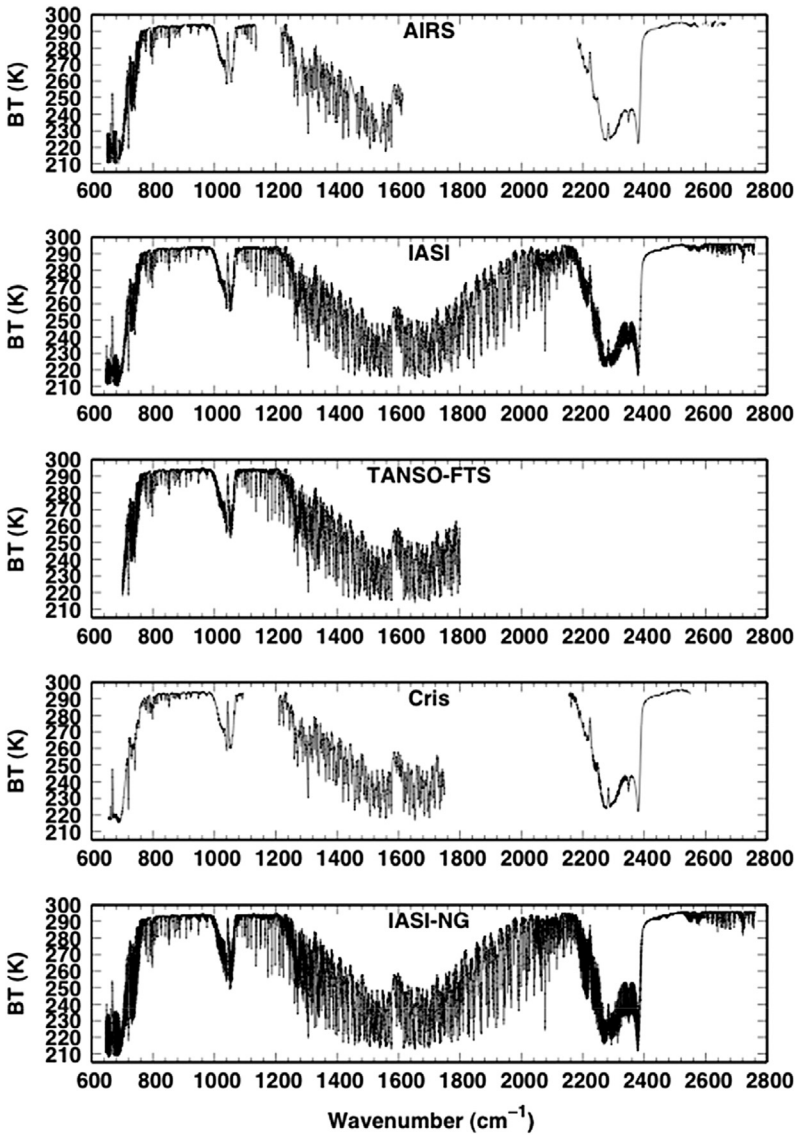

Fig. 2 Spectra of brightness temperature (BT) for a typical tropical situation computed with the 4A radiative transfer code for the spectral resolution and coverage of five hyperspectral infrared sounders: AIRS, IASI, TANSO-FTS, CrIS, and IASI-NG.

interferogram, the source spectrum is reconstructed using the inverse Fourier transform. In order to avoid oscillations around spectral lines that are due to the finite length of the interferograms, the latter are usually multiplied by a numerical function that decreases to zero at maximum delay; this operation is called "apodization" and slightly reduces the spectral resolution.

The main advantage of an FTIR instrument over dispersive spectrometers is that a single detection element can be used to record a broadband spectrum with high spectral resolution. For dispersive spectrometers, a scanning or large array detector must be used. One of the main drawbacks of an FTIR is its mechanical complexity, which requires moving optical elements which have to be guided with a very high precision over an extended distance, and very high alignment stability required for all optical components in the interferometer.

7.11.2.5 Hyperspectral Infrared Sensors for Earth Observation

7.11.2.5.1 IMG

The Interferometric Monitor for Greenhouse gases (IMG) (Kobayashi et al., 1999a,b, http://www.eoc.nasda.go.jp/guide/satellite/sendata/img-e.html) launched onboard ADEOS in August 1996 was the first high-resolution nadir infrared instrument allowing the simultaneous measurement from space of a series of trace gases: H_2O, CO_2, O_3, N_2O, CO, CH_4, and CFCs. Developed by the Japan Resources Observation System Organization (JAROS) for the Ministry of International Trade and Industry (MITI), IMG was a nadir-viewing Fourier transform interferometer that recorded the thermal emission of the Earth-atmosphere system

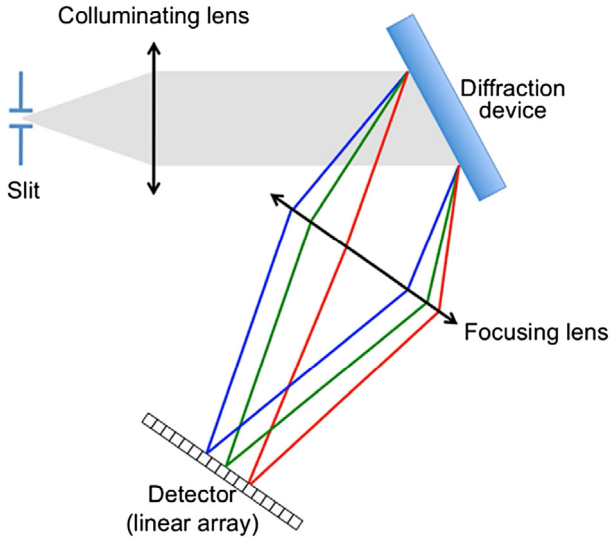

Fig. 3 Principle of a dispersive spectrometer.

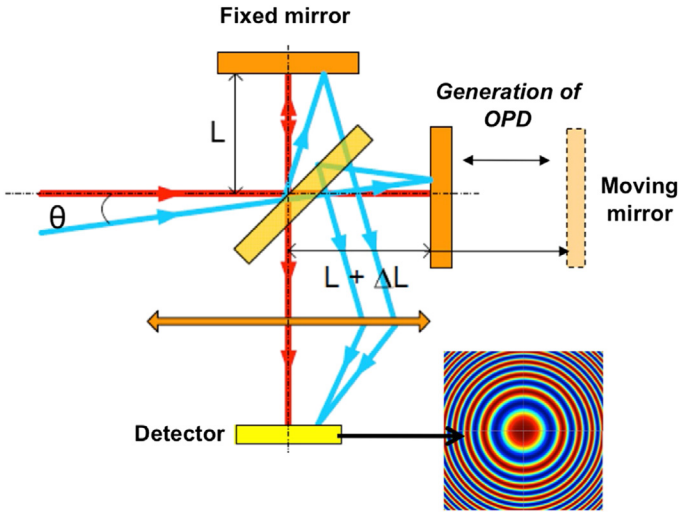

Fig. 4 Principle of a Fourier transform infrared spectrometer.

between 600 and 3030 cm^{-1}, with a maximum optical path difference of 10 cm. The footprint on the ground was 8 km × 8 km, in three spectral bands (band 1 from 2387 to 3030 cm^{-1}, band 2 from 2000 to 2500 cm^{-1}, and band 3 from 600 to 2000 cm^{-1}), corresponding to three different detectors and three geographically adjacent footprints.

Unfortunately, the ADEOS satellite ceased to collect and transmit data due to a power failure in its solar panel in June 1997. ADEOS was a sun-synchronous (equator local crossing time at descending node at 10:30 AM), ground track repeat, polar-orbiting satellite. The instrument performed a global coverage of the Earth, making 14 orbits per day with series of six successive measurements separated by 86 km (every 10 s.) along track, followed by the observation of deep space and of an internal blackbody for calibration purposes. Due to the huge data flow rate, the operational mode of IMG was set to 4 days operation out of 10 days, except for one specific period from 1 to 10 April 1997 for which 10 consecutive days were available.

7.11.2.5.2 MIPAS

The Michelson Interferometer for Passive Atmospheric Sounding (MIPAS) was launched by the European Space Agency (ESA) on ENVISAT in March 2002. MIPAS was a Fourier transform infrared (FTIR) spectrometer for the detection of limb emission spectra in the middle and upper atmosphere (Fischer and Oelhaf, 1996; Fischer et al., 2008). Thanks to its spectral resolution and coverage from 685 to 2070 cm^{-1} (4.15–14.6 μm, **Fig. 5**), MIPAS detected and spectrally resolved a large number of emission features of atmospheric minor constituents playing a major role in atmospheric chemistry (Raspollini et al., 2006; Carli et al., 2004). The primary geophysical parameters of interest were vertical profiles of atmospheric pressure, temperature, and volume mixing ratios of at least 25 trace constituents. The vertical resolution of the measured vertical profiles is in the order of some kilometers, but

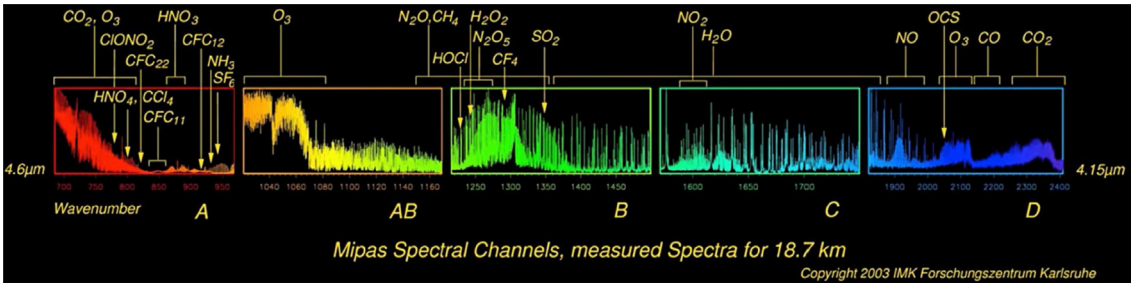

Fig. 5 Measured spectra by MIPAS in 5 spectral intervals (A, AB, C, and D) covering the spectral domains (685–2070 cm^{-1}; 4.15–14.6 μm) at 18.7 km tangent altitude. The large number of spectral emission lines highlights the resolving power of MIPAS, which enables the detection of a large number of trace constituents. Fischer, H., Birk, M., Blom, C., et al. (2008). MIPAS: An instrument for atmospheric and climate research. *Atmospheric Chemistry and Physics* **8**, 2151–2188. http://dx.doi.org/10.5194/acp-8-2151-2008

information on tropospheric parameters is limited. MIPAS is used for scientific investigations in various research fields: dynamics and chemistry of the upper troposphere, stratosphere, mesosphere, and lower thermosphere; weather forecasting using upper atmospheric levels for data assimilation; study of specific atmospheric physical processes such as nonlocal thermodynamic equilibrium at high altitude.

7.11.2.5.3 AIRS

The Atmospheric Infrared Sounder (AIRS) is a polar-orbiting nadir-viewing high-resolution infrared sounder operating in a cross-track-scanning mode (Aumann et al., 2003; https://airs.jpl.nasa.gov/). It was launched onboard the EOS Aqua satellite in May 2002, with two operational microwave sounders, AMSU (Advanced MicroWave Sounder) and HSB (Humidity Sounder Brazil). Operational since September 2002, it is a high-spectral resolution, grating multispectral infrared sounder with 2378 channels. Its spectral domain ranges from 650 to 2665 cm^{-1} (from 15.4 to 3.8 μm) and is divided into three spectral bands, from 650 to 1135 cm^{-1}, from 1215 to 1615 cm^{-1}, and from 2180 to 2665 cm^{-1}, yielding the uneven coverage of the thermal infrared domain shown in Fig. 2. AIRS has a spectral resolving power of 1200 (i.e., a spectral resolution ranging from 0.5 cm^{-1} at 650 cm^{-1} to 2 cm^{-1} at 2600 cm^{-1}). The different spectral resolution between the 3 bands is well seen in Fig. 2. AIRS cross-track scanning is 1650 km and covers 70% of the earth every day. The instantaneous field of view (IFOV) is sampled by 3×3 circular pixels whose ground resolution is 13 km at nadir. Aqua is in a sun-synchronous orbit and provides both a daytime ascending orbit with a local overpass time of 13:30 mean solar time and a nighttime descending orbit with a corresponding 01:30 local overpass time. Measurements from the three instruments are analyzed jointly to filter out the effects of clouds from the IR data in order to derive clear-column air-temperature profiles and surface temperatures with high vertical resolution and accuracy (1 K per 1 km layer in the troposphere). It also provides global distributions of several trace gases, as shown in Fig. 6 (Chahine et al., 2008; McMillan et al., 2005; Wright et al., 2005).

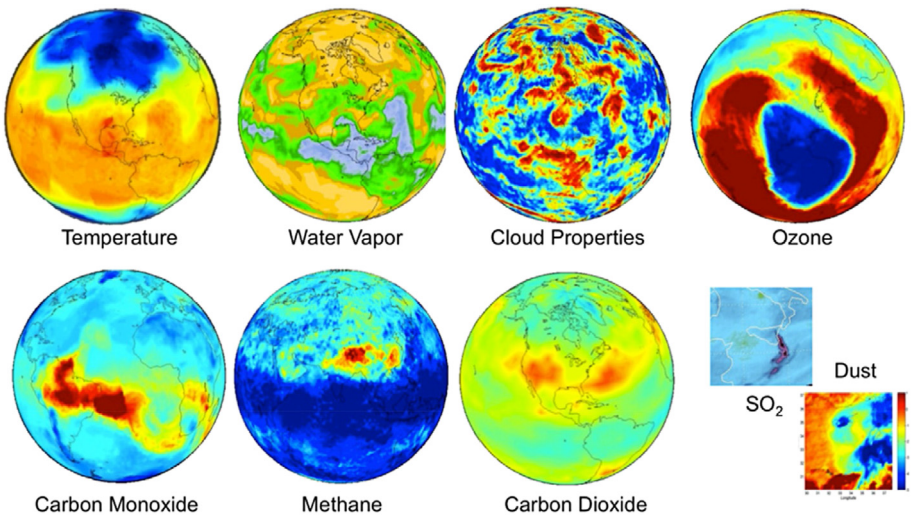

Fig. 6 Climatologies of AIRS retrieved geophysical parameters. Courtesy of T. Pagano and J. Teixeira.

7.11.2.5.4 ACE-FTS

The Atmospheric Chemistry Experiment Fourier transform spectrometer (ACE-FTS, http://www.ace.uwaterloo.ca/) is a limb sounder that records solar occultation measurements (up to 30 occultations each day). It was launched in August 2003 on board the Canadian SCISAT platform into a high-inclination (74 degrees), circular low-earth (650 km from the surface), which gives SCISAT coverage between approximately 85°N and 85°S (Bernath et al., 2005), with more observations at high latitudes than over the tropics (Bernath, 2006). ACE-FTS is an infrared Fourier Transform Spectrometer with a high spectral resolution (0.02 cm^{-1} corresponding to a maximum optical path difference of 25 cm) and a signal-to-noise ratio higher than 300:1 over a large portion (1000–3000 cm^{-1}) of the spectral range covered (750–4400 cm^{-1}). ACE-FTS measures sequences of atmospheric absorption spectra during sunrise and sunset (15 of each per day). These spectra, measured in the limb viewing geometry with different slant paths and tangent heights are inverted to obtain vertical profiles of temperature, pressure and the volume mixing ratios for several dozen molecules and related isotopologues (O_3, CH_4, H_2O, NO, NO_2, $ClONO_2$, HNO_3, N_2O, N_2O_5, HCl, CCl_3F, CCl_2F_2, HF, and CO) (Boone et al., 2005; Bernath, 2017) with a vertical resolution of about 4 km from the cloud tops up to about 150 km. ACE-FTS provides accurate measurements with high vertical sampling, but its horizontal resolution is limited by the 500 km path length of solar occultation technique. **Fig. 7** shows the evolution of the atmospheric spectra, expressed in terms of atmospheric transmission, that have been measured by ACE-FTS during one solar occultation at different tangent height in the 1–0 CO absorption band between 2060 and 2240 cm^{-1}.

7.11.2.5.5 TES

The Tropospheric Emission Spectrometer (TES) (Beer et al., 2001) is a high-resolution infrared-imaging Fourier transform spectrometer aboard NASA's Aura satellite, with spectral coverage of 650–2650 cm^{-1} (3.2–15.4 μm) at a spectral resolution of 0.025 cm^{-1}, thus offering line-width-limited discrimination of essentially all radiative active molecular species in the Earth's lower atmosphere (NO_y, CO, O_3, H_2O, SO_2, H_2, CO_2, etc.) (http://eoschem.gsfc.nasa.gov/instruments/tes/introduction.html). TES has the capability to make both limb and nadir observations. In the limb mode, TES has a vertical resolution of 2.3 km, with coverage up to 34 km. In the nadir mode, TES has a spatial resolution of 0.53×5.3 km with a swath of 5.3×8.5 km. TES is a pointable instrument and can access any target within 45 degrees of the local vertical, or produce regional transects up to 885-km length without any gaps in coverage. TES employs both the natural thermal emission of the surface and atmosphere and reflected sunlight, thereby providing day–night coverage anywhere on the globe. TES has less dense spatial coverage than scanning satellites such as AIRS or IASI but has a higher spectral resolution. TES is in a sun-synchronous orbit and provides both a daytime ascending orbit with a local overpass time of 13:30 mean solar time, providing favorable conditions for high thermal contrast and thus increased sensitivity to boundary layer for a few gases, and a nighttime descending orbit with a corresponding 01:30 local overpass time. The smaller satellite footprint of TES (5–8 km) also allows for the potential to detect localized surface sources (Shephard et al., 2015).

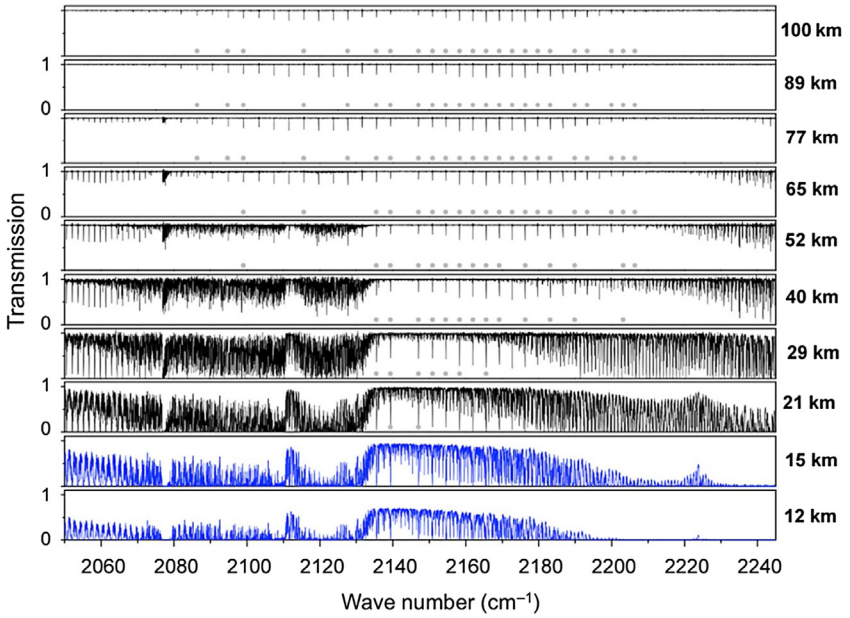

Fig. 7 Spectra of atmospheric transmission measured by ACE-FTS on the CO absorption band for various tangent heights (from 12 to 100 km). Adapted from Clerbaux, C., M. George, S. Turquety, et al. (2008). CO measurements from the ACE-FTS satellite instrument: Data analysis and validation using ground-based, airborne and spaceborne observations. *Atmospheric Chemistry and Physics* **8**, 2569–2594.

7.11.2.5.6 IASI

The Infrared Atmospheric Sounding Interferometer (IASI) is a high-resolution Fourier Transform Spectrometer based on a Michelson Interferometer coupled to an integrated imaging system that measures infrared radiation emitted from the Earth (https://iasi.cnes.fr/en/IASI/index.htm). Developed by the Centre National d'Etudes Spatiales (CNES) in collaboration with the European Organisation for the Exploitation of Meteorological Satellites (EUMETSAT), IASI was launched in October 2006 onboard the polar-orbiting Meteorological Operational Platform (Metop-A), and in September 2012 onboard Metop-B. A third IASI will be launched onboard Metop-C in October 2018. IASI provides 8461 spectral samples, ranging from 645 to 2760 cm^{-1} (15.5 and 3.6 μm), with a spectral sampling of 0.25 cm^{-1}, and a spectral resolution of 0.5 cm^{-1} after apodization (Fig. 2). IASI is an across track scanning system, whose swath width is of 2200 km, allowing global coverage twice a day. The IFOV is sampled by 2×2 circular pixels whose ground resolution is 12 km at nadir at 9:30 am/pm local time.

In addition to its contribution to numerical weather prevision, IASI has demonstrated the possibility to retrieve or detect several chemistry and climate variables from hyperspectral infrared observation in nadir-viewing mode (Fig. 8) such as water vapor (H_2O), carbon dioxide (CO_2), carbon monoxide (CO), methane (CH_4), ozone (O_3), sulfur dioxide (SO_2), hydrogen

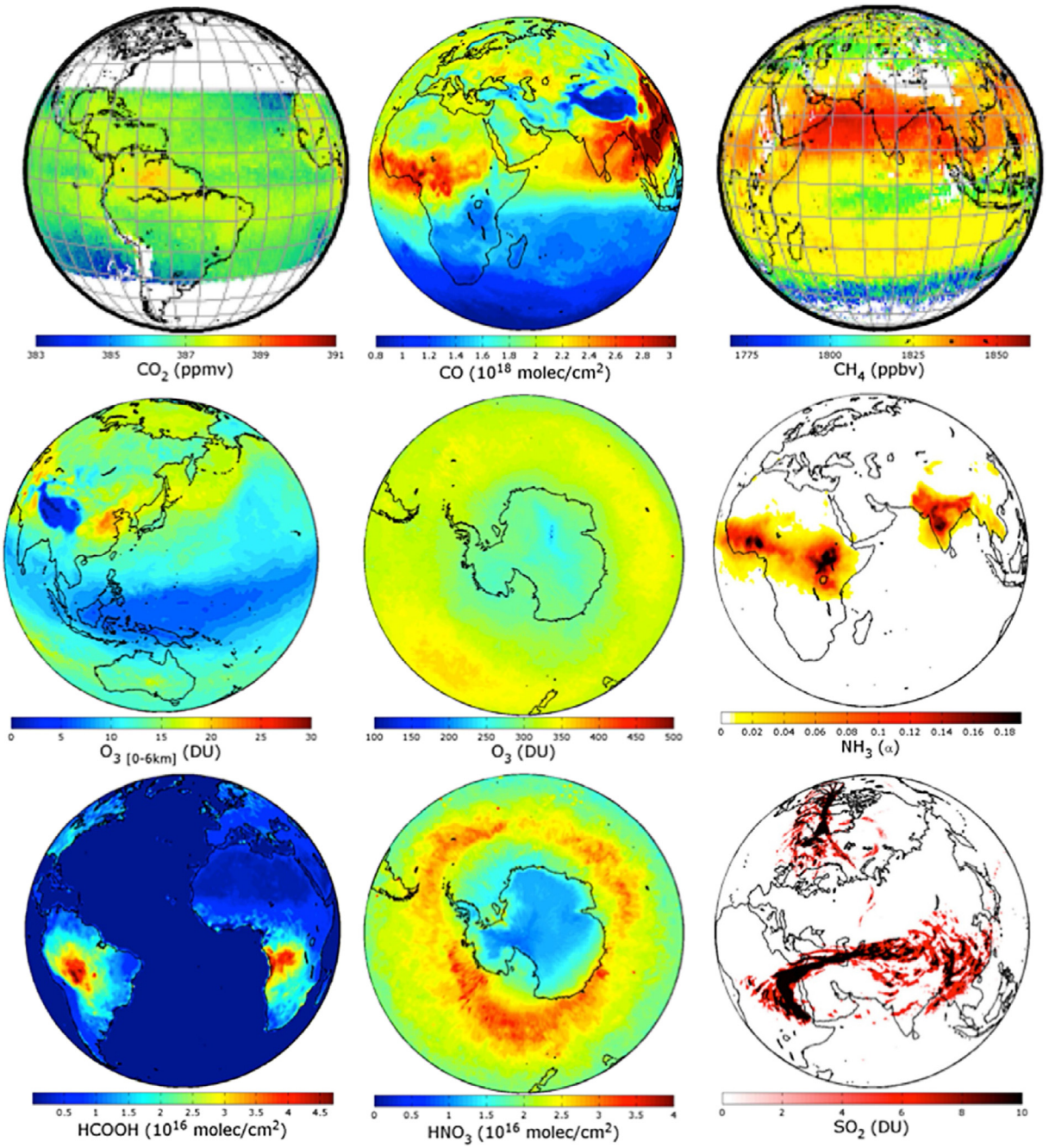

Fig. 8 Climatologies of the major atmospheric species retrieved from IASI onboard Metop-A.

sulfide (H_2S), ammonia (NH_3), nitric acid (HNO_3), volatile organic compounds (VOCs), and aerosols (Clerbaux et al., 2009; Crevoisier et al., 2009a,b; Hilton et al., 2012; Clarisse et al., 2011; Clerbaux and Crevoisier, 2013; Capelle et al., 2014) on regional and global scales. IASI has given access to species that had never previously been observed from space on a global scale (Clarisse et al., 2009; Razavi et al., 2011; Duflot et al., 2013) and enables the monitoring of key gases for climate and atmospheric chemistry in near real time.

7.11.2.5.7 TANSO-FTS

The Thermal And Near infrared Sensor for carbon Observations-Fourier Transform Spectrometer (TANSO-FTS) has been launched in January 2009 onboard GOSAT, which is a joint satellite project of the National Institute for Environmental Studies (NIES), Ministry of the Environment (MOE), and Japan Aerospace Exploration Agency (JAXA) for the purpose of making global observations of greenhouse gases such as CO_2 and CH_4 (Hamazaki et al., 2005; Yokota et al., 2009). TANSO-FTS covers three bands in the short-wave infrared region (12,900–13,200, 5800–6400, 4800–5200 cm^{-1}) and one band in the thermal infrared region (700–1800 cm^{-1}) at a spectral resolution of 0.2 cm^{-1} (Fig. 2). It operates in a nadir or near-nadir-viewing geometry. To improve coverage, its field of view sweeps longitudinally, and TANSO-FTS makes several measurements along each cross track, five measurements prior to August 2010, and three since then (Kuze et al., 2012). Also flown on GOSAT, the TANSO-Cloud and Aerosol Imager (CAI) aims at detecting clouds and aerosols in the TANSO-FTS field of view (Kuze et al., 2009). A persistent spectral bias in the thermal infrared domain, which appears to be mainly caused by an uncertainty in polarization correction, has hampered the use of this band, even if retrievals of CO_2 and CH_4 have been made from using the 4th band in addition to retrieval of total columns from its 3 bands located in the short-wave infrared (Saitoh et al., 2009).

7.11.2.5.8 CrIS

Launched onboard the Suomi National Polar-orbiting Partnership platform on October 28, 2011, the Cross-track Infrared Sounder (CrIS) is a Fourier transform spectrometer with a total of 1305 infrared sounding channels covering the long-wave (655–1095 cm^{-1}), mid-wave (1210–1750 cm^{-1}), and short-wave (2155–2550 cm^{-1}) infrared spectral regions (https://jointmission.gsfc.nasa.gov/cris.html, Goldberg et al., 2013), as shown in Fig. 2. The CrIS instrument has an 8 cm clear aperture and utilizes plane mirror interferometer technology. CrIS can also be operated in a full spectral resolution mode, in which the MWIR and SWIR band interferograms are recorded with the same maximum path difference as the LWIR band and with spectral resolution of 0.625 cm^{-1} for all three bands (total 2211 channels).

CrIS is in a sun-synchronous orbit (824 km) with a mean local daytime overpass time of 13:30 in the ascending node, and a mean local nighttime overpass time of 01:30 in the descending node. CrIS is an across-track scanning instrument with a 2200 km swath width, with the total angular field of view consisting of a 3×3 array of circular pixels of 14 km diameter each (nadir spatial resolution). It provides global distributions of several trace gases, as shown in Fig. 9.

7.11.2.5.9 IASI-NG

As part of the Earth Polar System Second Generation (EPS-SG) program of EUMETSAT, CNES has initiated the study of the IASI-New Generation (IASI-NG) mission. Its main objectives are: (i) continuity of the IASI/Metop series; (ii) improvement of the vertical coverage and resolution, especially in the lower troposphere; and (iii) improvement of the precision and detection threshold of atmospheric and surface components. To fulfill these goals, IASI-NG will measure infrared radiation emitted by the Earth with improved spectral resolution and radiometric noise as compared to IASI (Crevoisier et al., 2014).

IASI-NG will be a high-resolution Fourier Transform Spectrometer based on a Mertz Interferometer (Luitot et al., 2013) that will cover the spectral range 645–2760 cm^{-1}. It will provide 16,923 spectral samples, with a spectral sampling of 0.125 cm^{-1}, and a spectral resolution of 0.25 cm^{-1} after apodization (Fig. 2). The radiometric noise of IASI-NG will be improved by a factor 2 (for long-wave channels) to 4 (for short-wave channels) as compared to IASI. With a swath width of 2200 km, allowing global coverage twice a day, the IFOV will be sampled by circular pixels with ground resolution of 12 km at nadir. IASI-NG will be flown onboard the three Metop-SG-A platforms, scheduled for launch in 2022, 2028, and 2035.

7.11.3 Analysis of Spectral Signatures of Trace Gases in the Thermal Infrared

7.11.3.1 Forward Modeling

Radiative transfer forward models aim at simulating the radiances that should be measured by a considered instrument, given: (i) an atmospheric situation, described by its vertical profiles of temperature, water vapor, atmospheric gases and surface characteristics; (ii) the instrument specifications (instrumental spectral response function, scan geometry). The simulation is based on the radiative transfer equation ("Radiative transfer equation" section), using a radiative transfer code ("Radiative transfer forward codes" section) with input from a spectroscopic database ("Line parameters and line shapes" section) and atmospheric databases ("Atmospheric databases" section).

7.11.3.1.1 Radiative transfer equation

The general radiative transfer can be written as:

$$I_\nu^{sat} = I_\nu(s_0)t_\nu(s_0, s_L) + \int_{S_0}^{s_L} B_\nu(T(s))\frac{\partial t_\nu(s, s_L)}{\partial s}ds \quad (1)$$

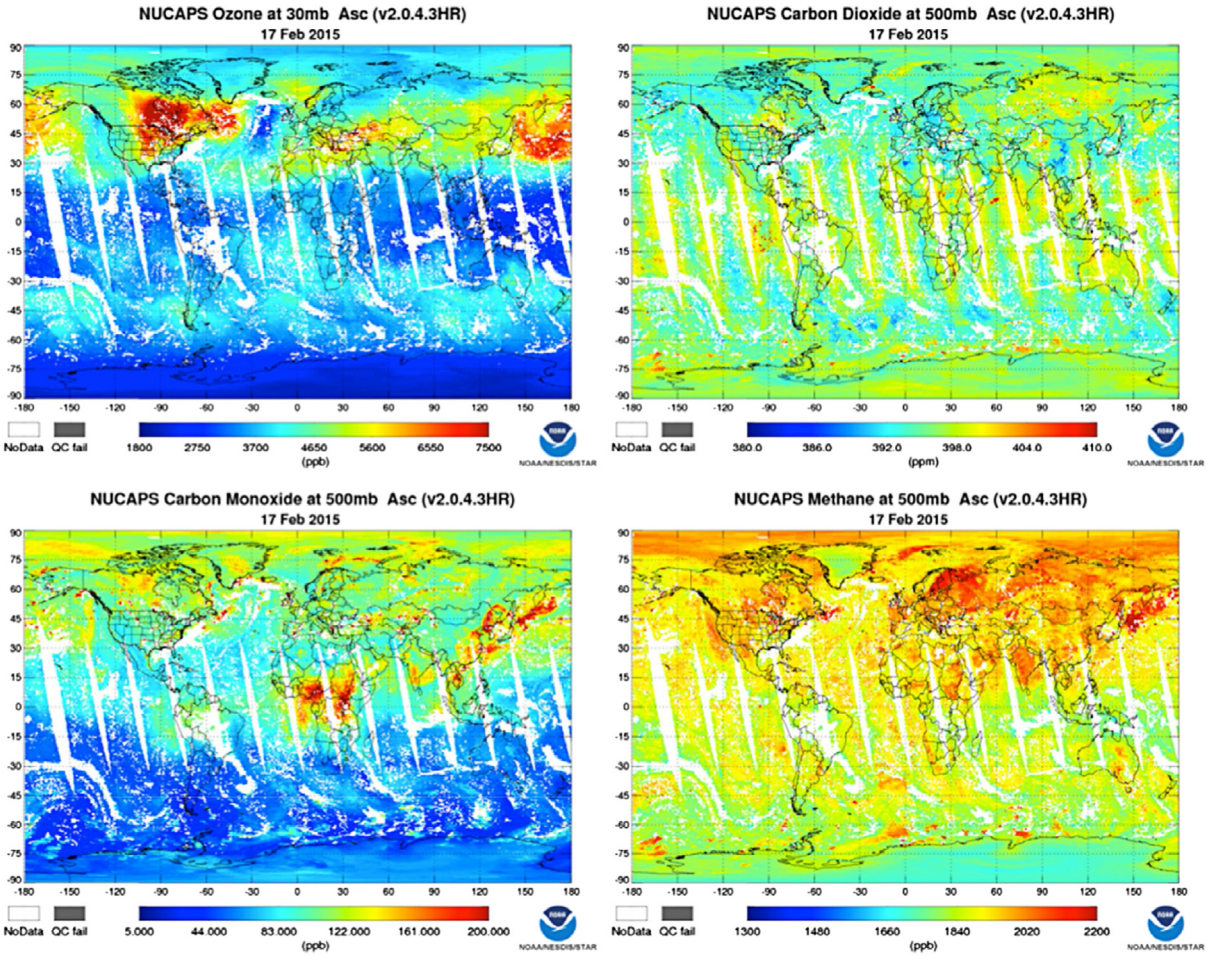

Fig. 9 Daily maps for February 17th 2015 of ozone at 30 hPa, carbon dioxide at 500 hPa, carbon monoxide at 500 hPa, and methane at 500 hPa retrieved from CrIS using an upgraded version of the NUCAPS algorithm (Gambacorta et al., 2014). Courtesy of Flavio Iturbide Sanchez.

where I_ν^{sat} is the radiance measured by the instrument at frequency ν, s is the atmospheric layer thickness, $B_\nu\ (T(s))$ is the Planck black-body function at temperature T, and t_ν is the atmospheric transmission along the optical path $[s_0, s_L]$ which can be written using the Lambert's Law as

$$t_\nu(s, s_L) = \exp\left[-\int_s^{s_L} \alpha_\nu(s')ds'\right] \tag{2}$$

where α_ν is the absorption coefficient in a given atmospheric layer. It is obtained by summing all the individual molecular absorption coefficients of the gases present in the layer.

In the case of a nadir-viewing instrument, s_0 and s_L are the ground and the top of the atmosphere, respectively. The radiance measured by the instrument is thus the sum of two terms: (i) the radiation coming from the surface and that is not absorbed by the atmosphere and (ii) the sum of the thermal emissions of each layer of the atmosphere, which is partly absorbed by the layers located above. For limb-viewing instruments operating in solar occultation, the first term dominates the equation and $I_\nu(s_0)$ represents the solar radiance.

To compute I_ν^{sat}, the atmosphere is divided into several atmospheric layers that are considered homogeneous. Once the absorber amount of each radiative molecule present in the layer is specified, representative values for temperature and pressure in the layer are used to compute the gas absorption coefficient for each point of a chosen spectral grid. Using the length of the path across the layer, the absorption coefficient is converted into the corresponding optical depth, and by combining the contribution of all radiating species, the corresponding profile of atmospheric transmittances can be easily obtained from Eq. (2). The monochromatic radiance is then computed using Eq. (1). Finally, the radiance that would be measured by a given instrument is computed by convolutic the radiance from Eq. (1) with the corresponding instrumental spectral response function.

It is important to stress that the radiative transfer modeling of atmospheric spectra in the thermal infrared is a very challenging task, that can take up to several minutes—even on very modern computers—for a broad spectral region (e.g., some 100 cm^{-1}) at high spectral resolution (e.g., 0.001 cm^{-1}). This is especially important for the inverse problem where concentration profiles of

atmospheric trace gases are determined from spectra, since they usually require massive radiative transfer calculations, either during the iterative retrieval procedure or to compute training databases (see "Inverse Radiative Transfer" section).

Alongside atmospheric transmission and radiances, another radiative quantity is required in the retrieval procedure of any gas: the Jacobians. A Jacobian is defined as the partial derivative of the channel brightness temperature with respect to a layer physical variable such as a gas mixing ratio, a temperature, or the emissivity. We will see that they play a significant role in the inversion of the radiative transfer equation (see "Inverse Radiative Transfer" section).

7.11.3.1.2 Radiative transfer forward codes

Three main types of radiative transfer models can be used to exploit radiances measured by hyperspectral infrared sounders: line-by-line models, pseudo-line-by-line models, and fast models.

Line-by-line (LBL) models are based on the full computation of the radiative transfer equation to accurately simulate atmospheric transmittances and radiance spectra at a spectral resolution much higher than the instrument resolution. While very accurate, they are computationally expensive. LBL models can be coupled to full scattering codes to simulate the radiative effects of atmospheric scattering due to particles like aerosols, water droplets, and ice crystals. Available LBL models include GENLN2 (Edwards, 1992), KOPRA (Stiller, 2001), LBLRTM (Clough et al., 2005), RFM (Dudhia, 1997), and STRANSAC (Scott, 1974).

Alongside full LBL models, pseudo LBL models have been developed. They are more computationally efficient but less accurate than full LBL models. For these models, monochromatic absorption coefficients are computed using a database of look-up tables created using a full LBL model. Because the monochromatic absorption coefficient varies slowly with temperature and is directly proportional to the absorber amount, the monochromatic absorption coefficients stored in the look-up table can be interpolated in temperature and modified for changes in absorber amount to give the most appropriate absorption coefficients for a given profile. Such models can perform calculations up to two orders of magnitude faster than LBL models, with an accuracy similar to the underlying LBL model. Available pseudo-LBL models include 4A (Scott and Chédin, 1981), FORLI (Hurtmans et al., 2012), kCARTA (DeSouza-Machado et al., 1997), and σ-IASI (Amato et al., 2002).

Fast radiative transfer models, which are also based on LBL models, use computationally efficient parameterizations in order to simulate radiances at a much reduced computation time than LBL models. Fast RT models can reproduce LBL radiances to an accuracy typically below the instrument noise, but their use is restricted to the considered instrument. Among the several types of fast RT models, one of the most widely used type uses regression coefficients derived from accurate LBL computations to compute atmospheric optical depths as a linear combination of profile-dependent predictors that are functions of temperature, absorber amount, pressure, and viewing angle. The regression coefficients are computed using a training set of diverse atmospheric profiles chosen to represent the range of variations in temperature and absorber amount found in the atmosphere. The optical depths can be computed at fixed pressure levels as in the RTTOV (Matricardi et al., 2004) and SARTA (Strow et al., 2003) models or at levels of fixed absorber amount as in the OPTRAN model (McMillin et al., 1995).

7.11.3.1.3 Line parameters and line shapes

The computation of the absorption coefficient α_ν requires the accurate knowledge of the molecular parameters (e.g., central position, strength, half width) of the absorption/emission lines associated to all known discrete molecular transitions of each atmospheric molecule, as well as the specification of the line shape.

Molecular line parameters (positions, intensities, lower state's energies, pressure broadening, and pressure shift parameters) are available from spectroscopic databases such as HITRAN (Rothman et al., 2009, 2013) or GEISA (Jacquinet-Husson et al., 2011, 2016) that are updated on a regular basis. These databases also contain some parameters for aerosols (refractive indices) and absorption cross sections for molecules with very dense spectra that are not easily resolved into individual lines (e.g., CFCs).

It is worth mentioning that the regular improvement of the content of spectroscopic databases stemming from the improvement of the characterization of the absorption lines themselves, as well as of the interactions between the lines (such as line-mixing) is mandatory to fully exploit space missions and their ever increasing spectral and radiometric characteristics. This point is illustrated by **Fig. 10**, which shows the impact of the knowledge of spectroscopy on the retrieval of nitric acid (HNO_3) from MIPAS. Two spectral regions can be used for the retrieval of this trace gas in the thermal infrared: the 11 and 7.6 μm. For many years, a discrepancy was nonetheless observed between the volume-mixing ratio profiles retrieved using these two bands, the profile retrieved from the 11 μm band being considered to be the reference. Thanks to improved HNO_3 line positions and intensities generated for the 7.6 μm spectral region, HNO_3 volume mixing ratio profiles retrieved independently from MIPAS limb emission radiances in the 11 and 7.6 μm domains now show a good agreement (Perrin et al., 2016), and the "obs-calc" residuals between observed and simulated radiances are improved. A retrieval procedure using simultaneously the 11 and 7.6 μm microwindows is now envisaged.

Modeling of atmospheric spectrum is particularly sensitive to the good knowledge of the line profile parameters. For the lowest pressures (top of the atmosphere), line broadening is dominated by the Doppler effect. For the highest pressures (close to the surface), collisional effects (illustrating the interactions of the studied molecule with the others like N_2 and O_2) are the most important and yields the so-called Lorentz profile. For intermediate pressure range, the line profile is a mix of the both effects, which is the Voigt profile. This standard line profile results from the convolution of the Lorentz and Doppler profiles.

Small deviations from the Voigt profile, known as collisional narrowing effects, have been observed in the laboratory and in atmospheric spectra and need to be taken into account in the analysis of high-resolution atmospheric spectra in order to avoid impacting the accuracy of the simulated spectra. In particular, the effect of line-mixing, which is the change in line shape due to the redistribution of radiation in over-lapping spectral lines, needs to be included. This is notably the case for CO_2 Q branches

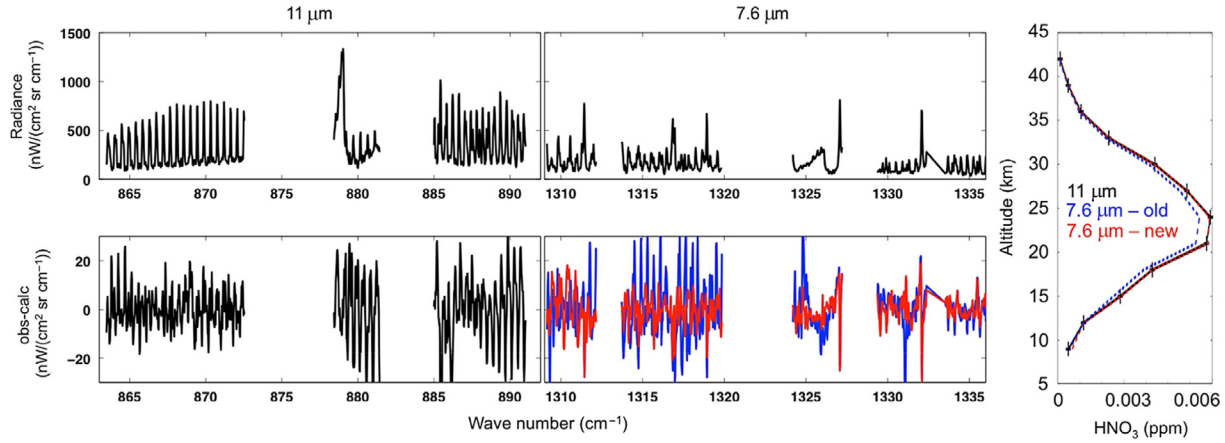

Fig. 10 Impact of improvement of spectroscopic knowledge on the retrieval of HNO_3 profiles using microwindows in the 11 and 7.6 μm spectral range observed by MIPAS. (*Top*) Radiances measured by MIPAS (*black*). (*Bottom*) Differences between radiances observed by MIPAS and radiances simulated by a radiative transfer code based on two version of the spectroscopy, either from GEISA-2011 (*blue*) or from GEISA-2015 (*red*). The content of both versions of the spectroscopic database is the same for the 11 μm band. (*Right*) Profiles retrieved from either the 11 μm microwindows (*black*) or the 7.6 μm microwindows (*blue* for GEISA-2011 and *red* for GEISA-2015).

(Strow and Reuter, 1988) and *P*/*R* branches (Niro et al., 2005), as well as for the ν_3 (3000 cm^{-1}) and ν_4 (1300 cm^{-1}) absorption bands of methane (Tran et al., 2006) and for a very limited number of transitions in the *P* and *R* branches of the water vapor ν_2 band centered at 1594 cm^{-1} (Brown et al., 2005). For very high spectral resolution, the shift of the line centre as a function of total pressure (typically a few 0.001 cm^{-1} per atmosphere) has also to be taken into account. To include these effects, replacements of the Voigt profile (e.g., Ngo et al., 2014) have been proposed. The International Union of Pure and Applied Chemistry (IUPAC) has recently recommended that the partially Correlated quadratic-Speed-Dependent Hard-Collision Profile (pCqSD-HCP) (Tran et al., 2013), known as the Hartmann–Tran profile (HTP), should be adopted as the appropriate model for high-resolution spectroscopy (Tennyson et al., 2014). Using a new standard profile would require significant updates to LBL models as well as to spectroscopic databases content.

7.11.3.1.4 Atmospheric databases

Retrieval schemes of geophysical parameters, design of new missions, or training of fast radiative transfer models are all built on a priori knowledge of typical atmospheric situations. Several databases exist that comprise realistic profiles of atmospheric temperature, gas concentrations, surface characteristics, and information on clouds and aerosols.

Radiosondes are the primary source of data for temperature and water vapor profiles. Temperature profiles are normally reliable up to 10 hPa although above 200 hPa corrections may have to be applied to remove consistent biases in the measurements due to radiative heating. Uncertainties are usually provided along with the temperature values. Additional information might come from rocketsondes providing upper stratospheric and mesospheric temperatures of radio-occultation measurements. The accuracy of water vapor radiosonde measurements is usually quite small, in particular in the vicinity of rapid transitions (e.g., top of boundary layer, transitions in and out of cloud, etc.). Moreover, no measurement is possible above 300 hPa. Stratospheric water vapor profiles are thus usually taken from limb sounders retrievals. Radiosondes can also provide profiles of O_3, or other gases, even if information generally comes from specific measurement campaigns or profiles retrieved from space missions. For other gases, atmospheric profiles are mostly provided by few dedicated aircraft campaigns (see "Validation" section), even if new instruments are being developed to provide measurements up to 30 km using metetorological balloons (Karion et al., 2010; Membrive et al., 2017).

Widely used by the remote-sensing community is the Thermodynamic Initial Guess Retrieval (TIGR) database (Chédin et al., 1985; Chevallier et al., 1998) that comprises 2311 atmospheric situations, each of them described by its profiles of temperature, water vapor, and ozone and provides a statistically representative description of the atmosphere. The ARSA (Analyzed RadioSoundings Archive) database (http://ara.abct.lmd.polytechnique.fr/index.php?page=arsa) is based on observations by worldwide distributed radiosonde stations, combined with surface and other auxiliary observations (Scott et al. in prep.). Physically coherent quality control tests have been developed to detect and eliminate gross errors: format problems, redundant radiosoundings and levels, unrealistic jumps, physically implausible values, temporal and vertical inconsistencies in temperature and dew point temperatures. Furthermore, every radiosonde report kept has been selected to be fully compatible with the forward radiative transfer simulations of the high-spectral resolution observations. The current ARSA database (about 6 million elements) starts in January 1979 and is extended onward, on a monthly basis.

In recent years, forecasting systems from Numerical Weather Prediction centers have been increasingly used to produce datasets of atmospheric profiles of temperature, atmospheric species, and surface parameters. In particular, in the framework of the Monitoring Atmospheric Composition and Climate (MACC) project that has now evolved in the European Copernicus Atmospheric Service (CAMS, https://atmosphere.copernicus.eu/), several datasets have been produced. In particular, Eresmaa et al. (2012)

have created a database that comprises 40,000 vertical profiles on 60 model levels and that includes 10 atmospheric variables (temperature, specific humidity, mixing ratios of ozone, carbon dioxide, methane, sulfate, organic matter, black carbon, sea salt, and desert dust aerosols) together with information on surface parameters.

7.11.3.2 Study of Atmospheric Transmissions

Fig. 11 shows a typical atmospheric transmission spectrum along with the detailed individual transmission spectra due to various trace gases. The spectrum has been computed at the IASI resolution with the 4A radiative forward model for an average nonpolluted tropical situation taken from the TIGR dataset. The main absorption features in the 645–2750 cm^{-1} spectral range are associated with rotational transition lines related to the fundamental vibrational bands of H_2O, CO_2, O_3, N_2O, CH_4, and CO. Each of these species combines intense absorption lines in this spectral range with high levels of atmospheric concentration. Weaker absorption contributions, which correspond to transmittance lower than 10%, are due to the presence of SO_2, CFCs (CFC11, CFC12, HCF22), NH_3, and HNO_3. All these molecules either have weak infrared absorptions or have low atmospheric mixing ratios. From these atmospheric transmissions and using the radiative transfer equation, it is straightforward to compute the radiances (or equivalently the brightness temperatures) that would be measured by the instrument, which correspond to the spectra plotted in Fig. 2.

The H_2O molecule is an asymmetric top configuration, which implies the existence of a permanent dipole moment, and thus a pure rotation spectrum that ranges from 0 to 1000 cm^{-1}. The most important vibrational–rotational band of water vapor is the ν_2

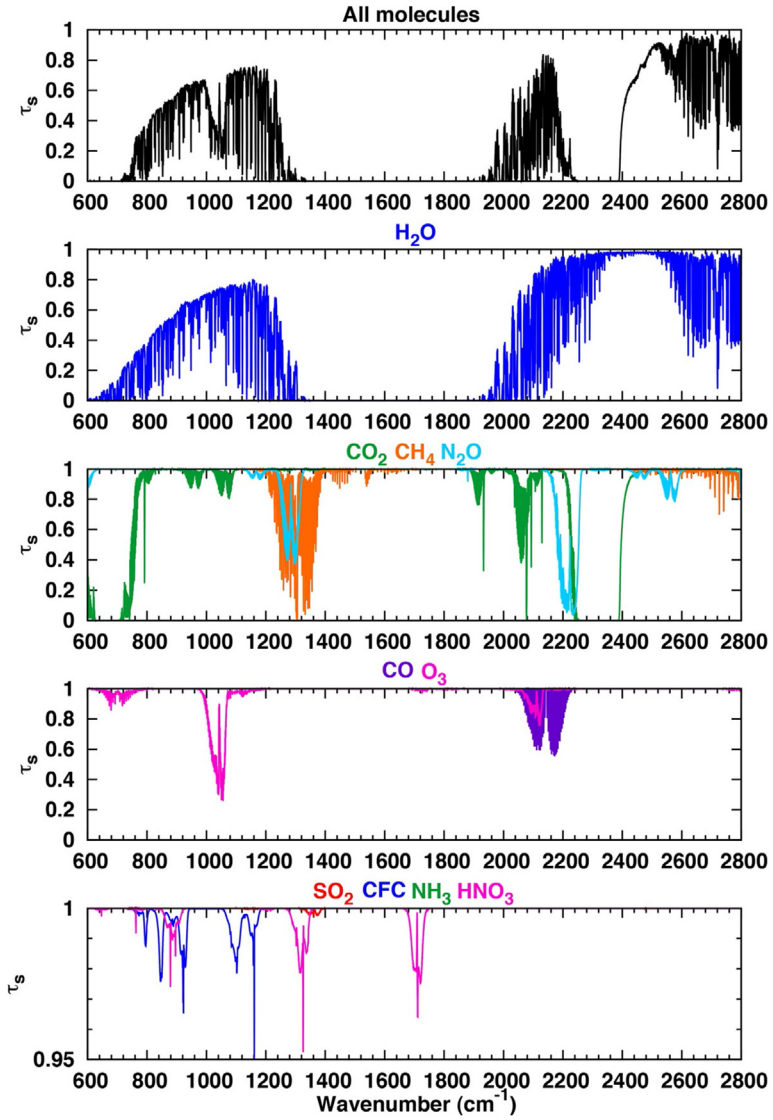

Fig. 11 Atmospheric transmission for a typical tropospheric situation computed with the 4A radiative transfer code for a nadir-viewing instrument at the spectral resolution of IASI, when taking into account all atmospheric molecules (*top*) or when considering one molecule at a time. Note that the scale of the y-axis of the bottom panel is much smaller that for the other panels.

fundamental band centered at 1594.78 cm^{-1} (6.25 μm), which extends approximately between 1200 and 2000 cm^{-1}. The two other fundamental bands, ν_1 and ν_3, are close to each other and are located at the edge of the thermal infrared region, at 3657 cm^{-1} (2.74 μm) and 3756 cm^{-1} (2.66 μm), respectively. For the 3 bands, H_2O isotopes, such as HDO, have been identified.

The spectral region from 800 to 1200 cm^{-1} (8–14 μm), which is usually referred to as the thermal infrared window, is characterized by a continuum of absorption due to water vapor species. The origin of this continuum is still debated. It has been suggested that it results from the cumulated absorption of far wings of strong absorption lines outside the infrared region, as well as to absorption by dimmers or larger molecular clusters.

The CO_2 linear molecule has no permanent dipole and no pure rotation spectrum. It has two fundamental vibration modes: the ν_2 mode, which is degenerated and coupled with rotational transitions leading to spectral lines referred to as the P, Q, and R branches, is centered at 667.0 cm^{-1} (15 μm); the ν_3 mode is centered at 2349.0 cm^{-1} (4.3 μm). While the former is characterized by a very strong Q branch, the latter does not have a Q branch. Two moderately strong bands are centered at 1063.8 and 961.0 cm^{-1}; their combination leads to the weak CO_2 laser emission band.

The methane molecule has a spherical top configuration, with no permanent dipole and thus no pure rotational spectrum. In the thermal infrared region, that means that only the ν_3 and ν_4 modes are active; they are located at 3020.3 and 1306.2 cm^{-1}, respectively.

The nitrous oxide molecule has a linear and asymmetric structure, with detectable rotational spectrum. It has three fundamental modes, ν_1, ν_2, and ν_3 which are located at 1285.6 cm^{-1} (7.8 μm), 588.8 cm^{-1} (17 μm), and 2223.5 cm^{-1} (4.5 μm). The former overlaps the ν_4 fundamental band of methane.

The ozone molecule is also an asymmetric top. Its most important absorption band is the ν_3 fundamental mode at 1042 cm^{-1} (9.6 μm). Two weaker bands are the ν_1 mode located at 1110 cm^{-1} (9 μm) and the ν_2 mode at 701 cm^{-1} (14.3 μm), which is superposed to the CO_2 ν_2 band.

The carbon monoxide molecule is a small linear structure. It absorbs the thermal infrared radiation mainly in its 1–0 vibrational band. Originating from unsymmetrical vibration modes, it is centered near 2140 cm^{-1} (4.7 μm) and covers the range 2080–2200 cm^{-1}.

The CFCs (chlorofluorocarbons) have absorption bands in the spectral region 800–1300 cm^{-1}. Easily identified in Fig. 11 is the absorption band of dicholorodifluoromethane (CF_2Cl_2), which is centered at 1161 cm^{-1} (8.6 μm) and has a band at 1095 cm^{-1} (9.1 μm), as well as the ν_1 and ν_4 fundamental transitions of trichlorofluoromethane ($CFCl_3$) which are located at 848.0 cm^{-1} (11.8 μm) and 1085 cm^{-1} (9.2 μm), or the 2 bands of methyl chloride (CH_3Cl) located at 732.0 cm^{-1} (13.7 μm) for ν_3 and located at 1350.0 cm^{-1} (7.4 μm) for ν_2.

Sulfur dioxide (SO_2) absorbs thermal infrared radiation in the ν_1 band around 1150 cm^{-1}, the ν_3 band around 1350 cm^{-1}, and the $\nu_1+\nu_3$ band around 2500 cm^{-1}. The ν_3 band is the most prominent but lies in a range where strong absorptions by methane and water vapor occur. Ammonia (NH_3) absorbs infrared radiation in the ν_2 vibrational band with a clear signature around 950 cm^{-1} and lines covering the full region 750–1200 cm^{-1}.

7.11.3.3 Analysis of Channel Sensitivities to Trace Gases

For a given frequency, the variation of radiances, or equivalently of brightness temperatures, measured by a given instrument stems from the strength of the absorption band of this molecule at the frequency, as well as from the variation of the concentration of the molecule. The capability of a hyperspectral infrared instrument to retrieve a given atmospheric variable will depend on three criteria that depends on the spectral and radiometric characteristics of the instrument: the level of the target signal, the signals due to other variables impacting the radiances on the same range (these signals will be referred to as "interferences"), and the altitude from which the absorption/emission levels come from. The first two criteria can be studied through the computation of the sensitivity of the channels to various atmospheric variables ("Integrated sensitivity of channels" section); the last one can be studied through the analysis of the channel Jacobians ("Vertical sensitivity" section).

7.11.3.3.1 Integrated sensitivity of channels

For a given atmospheric situation, the variation of the brightness temperature (BT) induced by a given variation of atmospheric and surface variables can be computed as

$$\Delta BT(\nu, \Delta T) = \sum_{j=1}^{nl} \frac{\partial BT}{\partial T}(\nu, j) \times \Delta T(j) \tag{3}$$

for temperature, and

$$\Delta BT(\nu, \Delta q_{gas}) = \sum_{j=1}^{nl} \frac{\partial BT}{\partial q_{gas}}(\nu, j) \times \Delta q_{gas}(j) \tag{4}$$

for a gas, where $\frac{\partial BT}{\partial T}(\nu, j)$ and $\frac{\partial BT}{\partial q_{gas}}(\nu, j)$ are, respectively, the temperature and gas Jacobians at pressure level j and nl is the number of pressure layers.

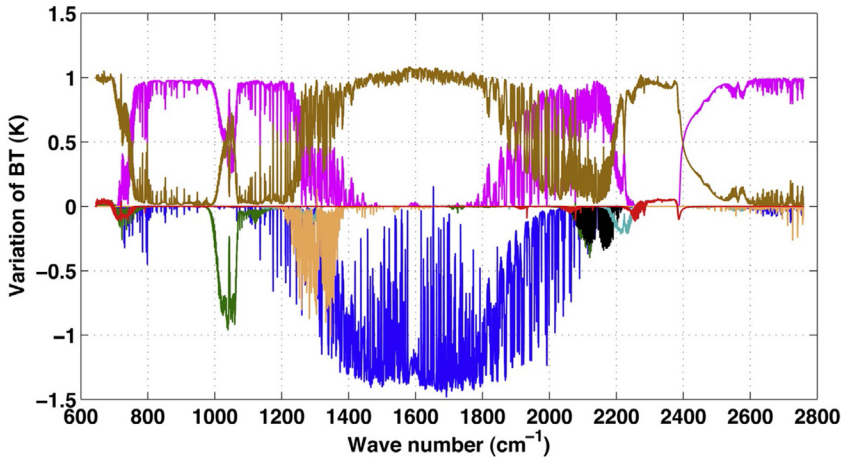

Fig. 12 Sensitivities of infrared channels at the spectral resolution and sampling of IASI (0.5 and 0.25 cm^{-1}, respectively, with 8461 channels) to various atmospheric and surface variables for a typical tropical atmospheric situation. Variations of 1 K of temperature (brown), 20% of water vapor (*blue*), 1% of CO_2 (*red*), 10% of O_3 (*green*), 2% of N_2O (*cyan*), 10% of CO (*black*), 10% of CH_4 (*orange*), and 1 K of surface temperature (*pink*). The computation of channels sensitivities is based on simulations performed using the forward radiative transfer model 4A based on the GEISA-2015 spectroscopic database.

Fig. 12 displays the channel sensitivity of IASI for typical variations of major atmospheric and surface variables, for the averaged tropical situation of the TIGR database. Variations of 1 K for atmospheric and surface temperatures, 20% for H_2O, 10% for O_3, 1% for CO_2, 10% for CH_4, 10% for CO, 2% for N_2O, and 0.05% for surface emissivity (ε_s) are considered. For a given channel, a negative sensitivity for a gas indicates that an increase of the gas concentration induces a colder BT, and thus a channel mostly sensitive to tropospheric variation of the gas concentration. Conversely, a positive sensitivity indicates a channel mostly sensitive to the stratosphere. The signatures of each variable given by the variation of BT can be compared to the radiometric noise computed at the brightness temperature of the scene according to the following equation

$$NE\Delta T[BT(\nu),\nu] = NE\Delta T\left[BT_{ref},\nu\right]\frac{\frac{\partial B}{\partial T}\left[BT_{ref},\nu\right]}{\frac{\partial B}{\partial T}\left[BT(\nu),\nu\right]} \tag{5}$$

where $NE\Delta T$ is the equivalent noise temperature taken at the brightness temperature BT, of the channel located at frequency ν, and B is the radiance. The reference noise corresponding to a reference temperature is usually provided by the space agency in charge of monitoring the instrument in flight.

Fig. 12 highlights the dominant role played by temperature and water vapor in the thermal infrared spectral range. The absorption bands of the other gases are also well seen in Fig. 12 and match the locations of the bands in Fig. 11. However, it is important to note that, even if the absorption of trace gases in the thermal infrared is large (total transmittances close to 0 in Fig. 11), the variation of brightness temperatures associated with a typical variation of their concentration is weak. Infrared channels are intrinsically sensitive to temperature; greenhouse gases, such as CO_2, CH_4, or N_2O, have a significant but minor impact, difficult to separate from this dominant signal. For instance, a variation of 1% (~4 ppm) of CO_2 only induces a variation of 0.1 K at 670 cm^{-1}. Moreover, the typical radiometric noise of the IASI channels is 0.25 K at this wavelength (more than twice the CO_2 signal), and the channels are mostly sensitive to atmospheric temperature variations, with a moderate variation of 1 K of the atmospheric temperature profile inducing an 0.8 K variation of brightness temperature! This extremely low signal-to-noise ration illustrates the challenge of retrieving the concentration of carbon dioxide, and of the other trace gases, from hyperspectral infrared sounders at the precision needed for climate studies. The radiometric noise level will particularly matter for gases having very small signature, whereas for other species, it will be more the spectral resolution that will matter in order to isolate the signature of each gas in the measured radiances (see "Impact of Spectral and Radiometric Specifications" section).

7.11.3.3.2 Vertical sensitivity

The channel sensitivities studied in the previous section are integrated quantities over the entire atmospheric column. In order to fully identify the spectral signatures of gas absorption, it is thus necessary to also consider how the modification of the mixing ratio of a given gas in one atmospheric layer contributes to the variation of the observed brightness temperature. This is done by studying the shape and value of gas Jacobians.

Fig. 13 shows an example of CO_2 Jacobians for specific channels located in the 15 μm ν_2 absorption band in the spectral range of 645–745 cm^{-1}. These Jacobians cover a large part of the atmospheric column. Channels located between 645 and 670 cm^{-1} are characterized by Jacobians mostly sensitive to the stratosphere, with a maximum sensitivity at 40 hPa and an extended coverage to most of the stratosphere. At higher wavenumbers, Jacobians mostly cover the troposphere with, for some of them, still a weak sensitivity to the lower stratosphere. In the troposphere, the Jacobians have their maximum between 200 and 400 hPa.

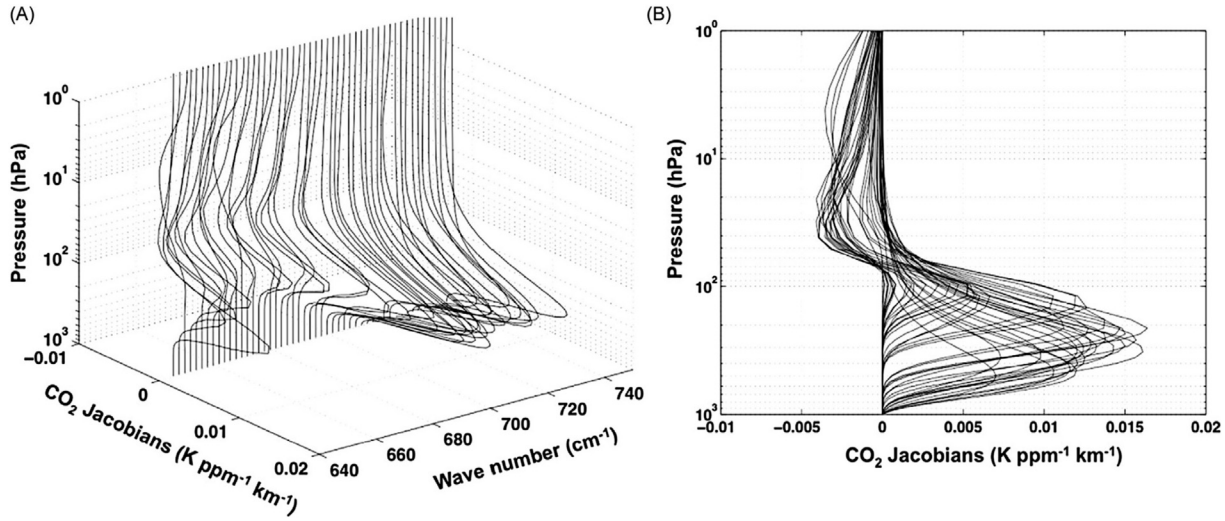

Fig. 13 CO_2 Jacobians for a typical tropical atmospheric situation computed using the forward radiative transfer model 4A for several IASI channels located in the spectral range of 645–745 cm^{-1}, plotted either against wave number and pressure (A) or against pressure only (B).

As seen in Fig. 13, long-wave infrared channels sensitive to variations of CO_2 in the troposphere are quite insensitive to two specific regions of the atmosphere: the lower troposphere (roughly below 400 hPa) and the tropopause (Crevoisier et al., 2003). For the latter, a channel peaking around the tropopause generally mixes the contribution of two parts of the temperature profile, one with a positive slope (lower stratosphere) where the emission is more important, and one with a negative slope (upper troposphere) where the absorption is more important. A vatition of CO_2 thus induces two signals that compensate one another. The same behavior is observed for most of the trace gases.

Concerning the lower troposphere, the shape of the Jacobian depends on the thermal contrast. As mentioned previously, the particularity of the thermal infrared domain is that for the main intense vibrorotation band of absorption of many molecules (as it is the case for CO_2 and CH_4), the radiation coming from the surface is totally absorbed by the first layers close to the surface. This implies that most of the information contained in the spectra measured by the spaceborne instruments is coming from higher levels in the atmosphere (essentially the mid- and upper troposphere). However, when the radiation coming from the surface or from the boundary layer is increased, the information close to the surface also increases. It is particularly the case when the thermal contrast, which is the difference between the surface temperature and the temperature of the first pressure level, is high. For a positive thermal contrast, the radiation coming from the surface is more important; for a negative thermal contrast, the radiation coming from the boundary layer is more important that the one coming from the surface.

In the case of CO_2, and other strong absorbers, the absorption of the part of the emission coming from the surface and the first atmospheric layers is totally absorbed. The Jacobians are thus equal to 0 near the surface. For weak absorbers, such as CO, it is possible to find situations for which the thermal contrast is high enough to overcome the full absorption of the emissions coming from the surface. Therefore, as shown by Deeter et al. (2007) for MOPITT, the vertical sensitivity to CO varies especially near the surface with the thermal contrast.

For instance, Fig. 14A shows 3 CO Jacobians corresponding to AIRS channels having strong sensitivities to CO. They have been computed with no thermal contrast. Fig. 14B shows the difference between these Jacobians and those computed with a $+10$ or -10 K thermal contrast. The higher the thermal contrast, the higher the sensitivity to CO in the lower part of the troposphere, particularly near the surface, with an opposite change of the sensitivity in the upper part of the troposphere. Negative and positive thermal contrasts have symmetric effects. We will study the impact of thermal contrast on the capacity of an infrared sounder to probe the boundary layer in "Retrievals in the Boundary Layer" section.

7.11.3.3.3 Examples for nadir-viewing instruments

In this section, we focus the analysis of the channel sensitivities and of the Jacobians to specific spectral regions corresponding to the major greenhouse gases and reactive gases.

7.11.3.3.3.1 Carbon dioxide (CO_2)

In the two major absorption bands, the CO_2 signature for a 1% variation comes to 0.15 K at 15 μm (ν_2 band) and 0.2 K at 4.3 μm (ν_3 band) as seen in Fig. 14. In comparison, a 1 K variation of the atmospheric temperature yields a variation of BT between 0.7 and 0.9 K at 15 μm and 0.7 and 1 K at 4.3 μm. Any CO_2 retrieval thus requires the decorrelation between temperature and CO_2 signals. In order to make this possible, channels with the lowest sensitivity to other components must be found (Chédin et al., 2003a; Crevoisier et al., 2003). In the weakest laser band centered at 1064 cm^{-1} (9.4 μm), the channel sensitivity to CO_2 variations is very low and the interferences with other species (H_2O, O_3, etc.) are quite high, preventing the use of the corresponding channels in the retrieval of CO_2.

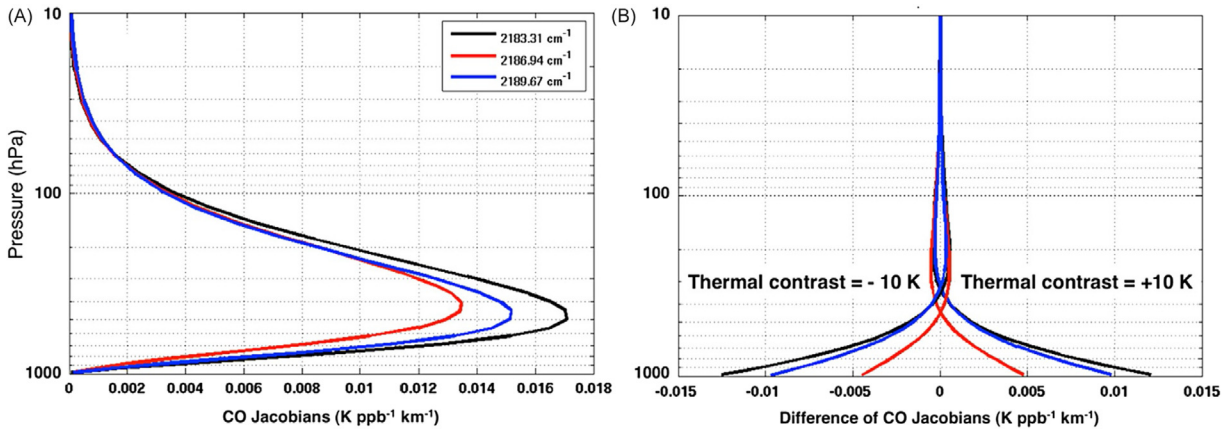

Fig. 14 (A) CO Jacobians for 3 AIRS channels computed with 4A for the average tropical situation of the TIGR database and assuming a thermal contrast equal to 0. (B) Difference between the Jacobians plotted in (A) and the Jacobians computed with a thermal contrast equal to ± 10 K.

In the ν_2 absorption band, the use of the 640–690 cm^{-1} range requires taking into account the line-mixing effect (*P*, *Q*, *R* branches at 660 cm^{-1}). Moreover, channel sensitivities to CO_2 are particularly weak (less than 0.1 K), and the channels are sensitive to stratospheric variations of CO_2. Therefore, most of the retrieval techniques of CO_2 are based on the use of the 690–730 cm^{-1} spectral range since, for wave numbers higher than 690 cm^{-1}, channels with lower sensitivities to ozone and water vapor can be found (**Fig. 15A**). In the ν_3 absorption band, the channels are mostly free of interferences, but for a sensitivity to N_2O (**Fig. 15C**), and most of the channels are sensitive to the stratosphere as shown by their Jacobians (**Fig. 15D**). Around 2390 cm^{-1}, channels present a relatively high CO_2 signal together with Jacobians covering higher pressure than those in the ν_2 absorption band.

The Jacobians of tropospheric channels presenting the lowest sensitivities to atmospheric variables other than CO_2 cover the pressure range of 110–400 hPa (7–15 km), with an average mid-height width of 210 hPa (**Fig. 15B**). Therefore, only information on CO_2 in the mid-to-upper troposphere is available with channels located at 15 μm. The ν_3 absorption band at 4.3 μm complements well the ν_2 absorption band at 15 μm since it gives information on CO_2 in a lower part of the atmosphere, closer to the surface (Crevoisier et al., 2003). CO_2 Jacobians at 4.3 μm peak between 350 and 600 hPa (4–8 km), with an average mid-height width of 400 hPa.

7.11.3.3.3.2 Methane (CH_4)

In the ν_4 absorption band methane at 1306.2 cm^{-1}, the main interference, as far as CH_4 is concerned, comes from H_2O, which largely dominates, with mean sensitivities of 1 K for a 20% variation of its mixing ratio (**Fig. 16**). The CH_4 signature for a 10%

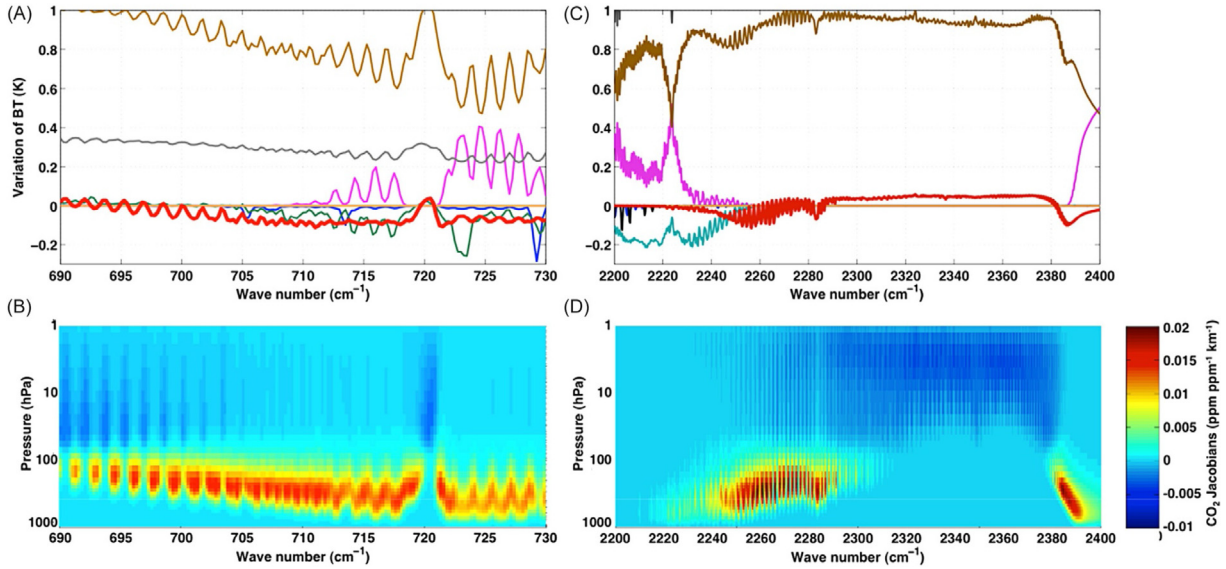

Fig. 15 Channel sensitivities and CO_2 Jacobians for the ν_2 and ν_3 absorption bands of CO_2 (A) Same as **Fig. 12** but for the CO_2 ν_2 absorption band between 690 and 730 cm^{-1}. The CO_2 signal is plotted in red. Also shown in grey is the IASI radiometric noise computed at the brightness of the scene according to Eq. (3). (B) CO_2 Jacobians plotted against wavenumber and pressure for the CO_2 ν_2 absorption. (C) Same as (A) but for the CO_2 ν_3 absorption band between 2200 and 2400 cm^{-1}. (D) Same as (B) but for the CO_2 ν_3 absorption band.

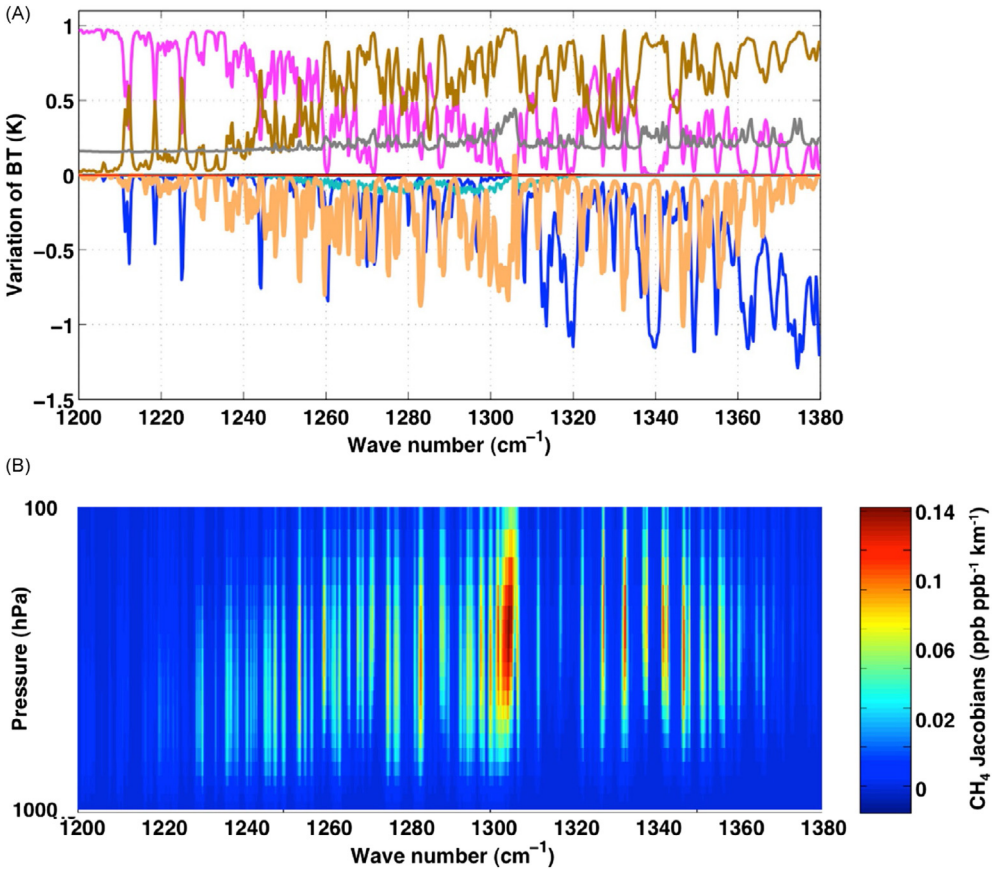

Fig. 16 Same as **Fig. 15** but for the CH_4 ν_4 absorption band between 1200 and 1380 cm^{-1}. The CH_4 signal is plotted in orange in Fig. 16A.

variation of the gas mixing ratio is about 1.5 K. Channels are also sensitive to nitrous oxide (N_2O) and surface characteristics. Since water vapor variability is quite high, especially in the tropics, and knowledge of its tropospheric distribution still limited, separating the CH_4 signal from water vapor is quite challenging and limits the retrieval performances. Only a few successive channels located in the 1301–1305 cm^{-1} interval present a low-enough sensitivity to water vapor to assure a limited impact on the retrieved methane of the uncertainties affecting water vapor (Crevoisier et al., 2009b, 2017). The spectral range where these channels are located can nonetheless be affected by two phenomena: line mixing and, to a lesser extent, water continuum, need to be taken into account in the simulations. Increasing the spectral resolution of the instrument is a real asset since it allows finding spectral intervals where the CH_4 signal "comes out" of the H_2O signal (Crevoisier et al., 2014).

Methane Jacobians are plotted in **Fig. 16B**. They peak at 250 hPa and cover the range 150–500 hPa. Infrared channels are not sensitive to variations of methane in two parts of the atmosphere: the lower troposphere (roughly below 500 hPa) and the tropopause (Crevoisier et al., 2003). This lack of sensitivity to the lower part of the atmosphere is a well-known feature of emission-based sounding instruments and occurs because of the lack of temperature contrast between the surface and the boundary layer.

In the ν_3 absorption band at 3.3 μm, which gives access to channels sensitive to the lower troposphere, atmospheric and surface temperatures, emissivity and reflectivity have the major impact and dominate the CH_4 signal. Hence, the use of this band requires a good knowledge of surface characteristics. Retrieving CH_4 atmospheric content from this part of the spectrum, which is also strongly sensitive to solar radiation, thus remains very challenging and might only be possible in particular conditions. The use of the ν_3 absorption band may potentially bring some information on the lower atmosphere under very specific conditions such as high reflected solar radiation (Razavi et al., 2009). The use of the ν_4 band only, although yielding constraints in the middle troposphere only, allows the retrieval of methane in all clear conditions, yielding an homogeneous long time record of tropospheric methane.

7.11.3.3.3.3 Ozone (O_3)

Ozone (O_3) has several absorption bands throughout the thermal infrared. The most suitable channels for O_3 retrievals are located in the strongest ozone absorption band near 1042 cm^{-1} (ν_3 9.7 μm band), with the most prominent band extending from 980 to 1100 cm^{-1}, almost free of interferences by any other atmospheric gas (**Fig. 17**). In the weaker ν_2 absorption band centered at 701 cm^{-1}, ozone signatures are mixed with those of H_2O and CO_2.

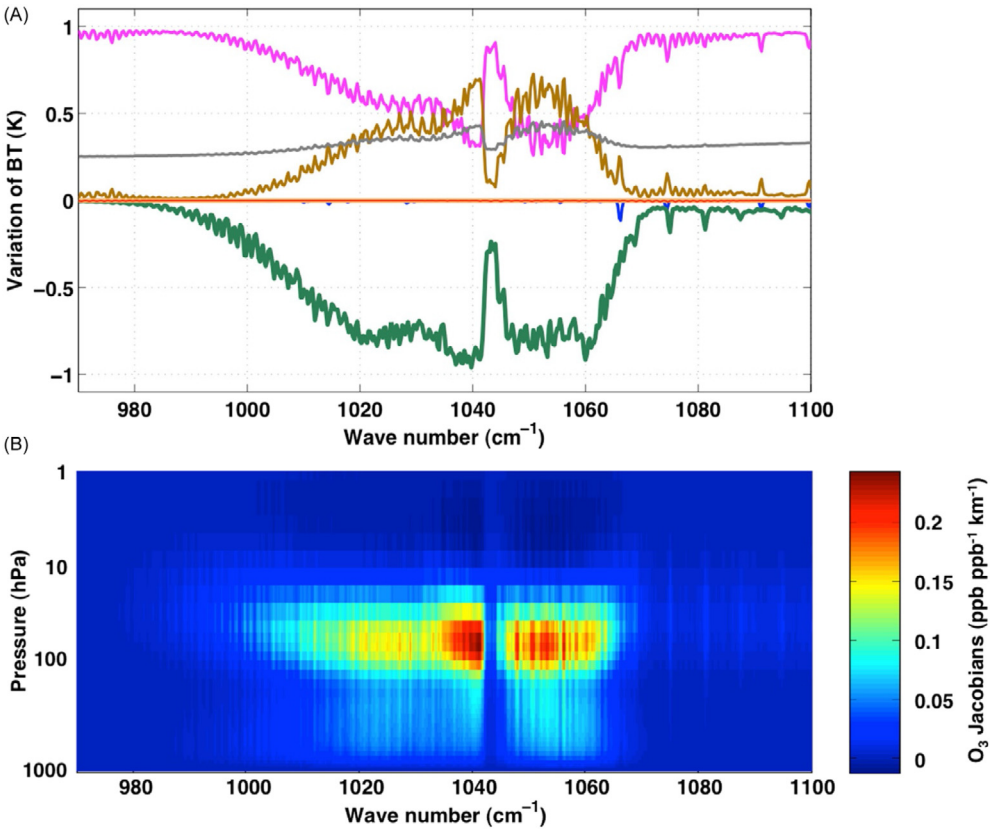

Fig. 17 Same as **Fig. 15** but for the O_3 ν_3 absorption band between 970 and 1100 cm^{-1}. The O_3 signal is plotted in green in Fig. 17A.

Most of the radiance signal comes from the free troposphere, although a nonnegligible part comes from the stratosphere (due to high concentrations), as seen on the O_3 Jacobians plotted in **Fig. 17B**. Previous experiences have demonstrated that the TIR measurements provide information on the ozone vertical profile from the ground up to an altitude of about 40 km, with a maximum sensitivity located in the mid-troposphere (Worden et al., 2007; Boynard et al., 2009; Dufour et al., 2012). The density of the spectra makes it difficult to discriminate individual lines and hence information in the boundary layer can hardly be obtained.

7.11.3.3.3.4 Carbon monoxide (CO)

The absorption band of CO, from 2080 to 2200 cm^{-1}, has interferences with lines associated with H_2O, CO_2, N_2O, and O_3 absorptions (**Fig. 18**). The CO signal is characterized by a well-defined comb-like feature. All channels suffer from weak to medium contaminations not only from these absorbing molecules but also from the surface. The strongest sensitivities to CO are found in the 2160–2200 cm^{-1} range, but the end of this band is impacted by stronger interferences from other absorbers. The best compromise between information content and interferences with other gases is thus the 2143–2181.25 cm^{-1} spectral range (De Wachter et al., 2012). From **Fig. 2**, it may be noted that AIRS spectral domain does not cover completely the CO absorption band (AIRS third spectral band begins at 2181.5 cm^{-1}). Channels located in the CO band are also strongly sensitive to surface temperature and to surface emissivity. Moreover, as the sensitivity to these two surface parameters gets weaker, the sensitivity to temperature and water vapor gets stronger. The sensitivity to N_2O is about 0.2 K at the end of the band and the sensitivity to O_3 is quasinull.

The averaged CO Jacobians computed with 4A on the TIGR tropical situations are plotted in **Fig. 18B**. For a null thermal contrast, the shape of the Jacobians is similar for all these channels, with a maximum at about 450 hPa (~6.5 km), and half the maximum between about 750 (~2.5 km) and 200 hPa (~12 km). Only the tropospheric contribution is seen in the radiance.

7.11.3.3.4 Specificity of limb-viewing instruments

For limb-viewing instruments, the study of the channel sensitivities to atmospheric species is performed for every tangent height. As opposed to nadir-viewing channels, for which sensitivities are integrated over the whole atmospheric column by summing the contribution from every atmospheric layer along the column, the sensitivities of limb-viewing channels are integrated over the long tangential optical paths for each tangent height. An example is shown in **Fig. 19** for ACE-FTS in the 1–0 CO absorbtion band between 2140 and 2200 cm^{-1}. The variations of radiances computed for given variations the

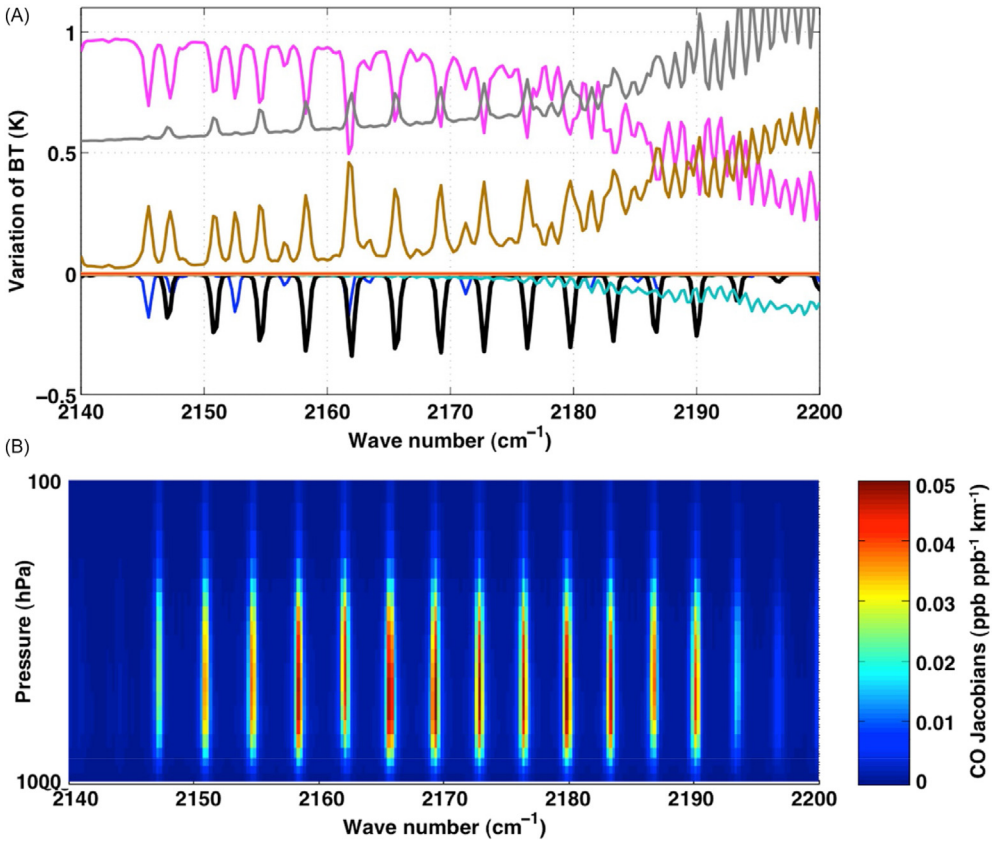

Fig. 18 Same as **Fig. 15** but for the CO 1–0 absorption band between 2140 and 2200 cm^{-1}. The CO signal is plotted in black in **Fig. 17A**. Co Jacobians have been computed with a null thermal contrast.

mixing ratios of CO and of the main interfering species located in this spectral range (N_2O, H_2O, and O_3) are plotted for tangent heights between 5 km (the lowest tangent height achievable) and 40 km (above which no CO signal is seen any more). These sensitivities are similar to the column-integrated ones obtained for IASI (**Fig. 18A**) and follow the evolution of IASI CO Jacobians plotted in **Fig. 18B**, with a maximum sensitivity around 7 km. Thanks to the extremely high sensitivity offered by limb-viewing, it is possible to retrieve a well-resolved vertical profile, with a CO mixing ratio being retrieved for each tangent height for altitudes higher than 5 km. Below this altitude, the absorption by water vapor (well seen in **Fig. 19**) and the presence of clouds strongly limit the retrieval of CO.

7.11.4 Inverse Radiative Transfer

7.11.4.1 Gas Retrieval Schemes

Retrieving geophysical variables, such as gas concentrations, from remotely sensed observations is a problem that is ill-conditioned, meaning that it has no unique solution, and nonlinear, since the radiative transfer equation is nonlinear. Moreover, in the case of the retrieval of trace gases concentration products (total columns, partial columns, or a vertically resolved atmospheric profiles), retrieval schemes have to deal with weak signal to noise ratio, as illustrated in "Analysis of Channel Sensitivities to Trace Gases" section.

In addition, as stated above, infrared observations are first and foremost sensitive to atmospheric temperature. The core of any retrieval technique thus consists in decorrelating the temperature signal from the gas signal in the radiances. This can be done either by including the temperature profile in the variables to be retrieved (the "state vector") or by using auxiliary information on temperature. The latter usually come from three distinct sources: (i) the temperature profile retrieved previously from the hyperspectral infrared instrument itself (either during the retrieval process, or independently, using the official level 2 temperature product of the instrument for instance). This may lead to significant correlations between the retrieved atmospheric parameters that need to be checked; (ii) the temperature profile from reanalyses that are interpolated at the date and location of the observation. However, the noise associated with these fields, at least 1.0 K, makes this information hard to use. In addition, climate-correlated biases associated with retrieved temperatures are particularly difficult to quantify and, thus, to eliminate; (iii) simultaneous measurements made in the microwave by companion instruments, which are mostly sensitive to temperature and not to atmospheric trace gases

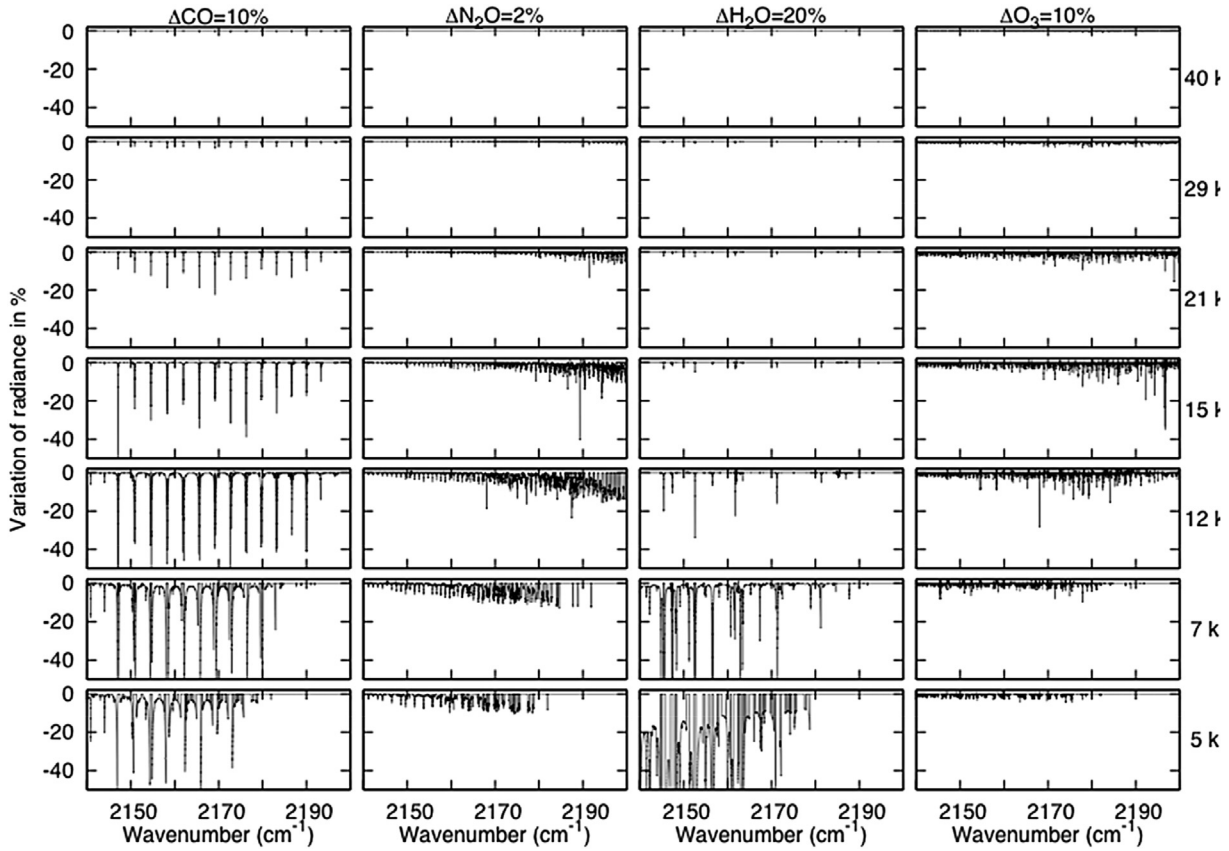

Fig. 19 Sensitivity of ACE-FTS to variation of atmospheric components in the CO 1–0 absorption band, between 2140 and 2200 cm^{-1}, shown as a variance of the radiance due to an increase of 10% of CO (*first column*), 2% of N_2O (*second column*), 20% of H_2O (*third column*), and 10% of O_3 (*fourth column*) for 7 height tangents from 5 to 40 km. Simulations have been performed with 4A.

(for instance, observations from the AMSU microwave sounder are synchronized with those made in the infrared by AIRS on Aqua or IASI on the Metop satellites).

A variety of methods have been developed to retrieve gas concentration products from hyperspectral infrared observations. They all rely on a forward radiative transfer model, using a specific version of a spectroscopic database. Based on a minimization scheme optimized for the instrument and species to be retrieved, they all aim at retrieving a likely solution by regularizing the retrieval with a priori information on the variables, which can take different forms. The most widely used retrieval techniques for trace and greenhouse gases can mostly be split into two categories: the Optimal Estimation Method (OEM) and nonlinear inference schemes based on neural networks. Before presenting them in "Optimal Estimation Method" and "Non Linear Inference Schemes Based on Neural Networks" sections, the preliminary steps required to perform the retrievals are described in "Preliminary Steps" section.

7.11.4.2 Preliminary Steps

7.11.4.2.1 Archiving of the observations

First of all, the observed radiances must be downloaded and stored. Usually, it is not raw radiances (level 0 data), but calibrated radiances (level 1 data) that are used in retrieval processes. The calibration is done by the space agency in charge of satellite operations. The data stream associated with hyperspectral sounders is directly proportional to the number of channels and number of fields of view that need to be stored. Level 1 data can then be used either in near-real time for operational applications, or at a later stage for specific studies, reprocessing, or climate applications.

7.11.4.2.2 Channel selection

Only a restricted number of channels are actually sensitive to the targeted gas. These are the channels located in the gas absorption band. A gas retrieval is thus usually based on a restricted number of channels, which are the ones optimal for retrieving the variables included in the state vector: the channels sensitive to the targeted gas, as well as the channels required to constrain atmospheric temperature, surface, and any other gas that might interfere with the targeted gas. Several methods have been designed to select the optimal channels for gas retrievals (Crevoisier et al., 2003; Gambacorta et al., 2014). Basically, two approaches can be used.

7.11.4.2.2.1 Selection of individual channels

The most common approach to reduce the length of the state vector is to select only the channels that provide the majority of the information related to the state vector. The number of channels more or less depends on the application. For gases characterized by many large absorption bands and impacted by many interfering species, many channels need to be chosen and selection algorithms are required. For species with only a few absorption lines within the spectral range of the instrument, the selection of the channels can be performed based on spectroscopic knowledge only.

The use of an algorithmic approach to channel selection is based on the choice of suitable selection criteria, which can be optimized for the particular species of interest. Three criteria might be used to identify the spectral regions offering the optimal characteristics for the retrieval: the target signal must be the highest possible, the target signal must be greater than the interferences (signals due to other variables), and the channels must harmoniously cover the whole atmospheric column. This is the approach chosen by the Optimal Sensitivity Profile method (Crevoisier et al., 2003) that has been used to select several AIRS channels for near-real time distribution to users interested in trace gases. Based on a common approach used in NWP centers (e.g., Collard, 2007), degrees of freedom for signal (see "Formalism" section), optimized with respect to the information content of the selected channels for the targeted gas, can be used (Chédin et al., 2003a).

7.11.4.2.2.2 Selection of spectral microwindows

A microwindow is a small set of contiguous channels over a very limited spectral interval. Its purpose is to isolate the absorption features of a given molecule within the small spectral interval for use in a retrieval scheme. Since only a few spectral lines need to be considered, the radiative transfer computations performed over contiguous channels are reduced. For instance, **Fig. 20** shows the microwindows selected on the spectra recorded by ACE-FTS for the retrieval of CO_2 profiles between 5 and 25 km (Foucher et al., 2011).

Combining the two previous methods, techniques for optimal selection of a microwindow have been developed for MIPAS and for other chemistry mission instruments (e.g., Dudhia et al., 2002). The general principle is based on sequential channel selection methods used for individual channel selection. Once a selection of candidate channels has been chosen using a figure of merit, each is used to create a microwindow by adding adjacent channels until subsequent channels fail to add any more information.

7.11.4.2.3 Cloud and aerosol detection

Observations in the infrared are strongly sensitive to clouds and aerosols. In order to avoid biasing the retrieved gas concentration (an undetected cloud will have the effect of decreasing the brightness temperature of the channels, which could be interpreted as an

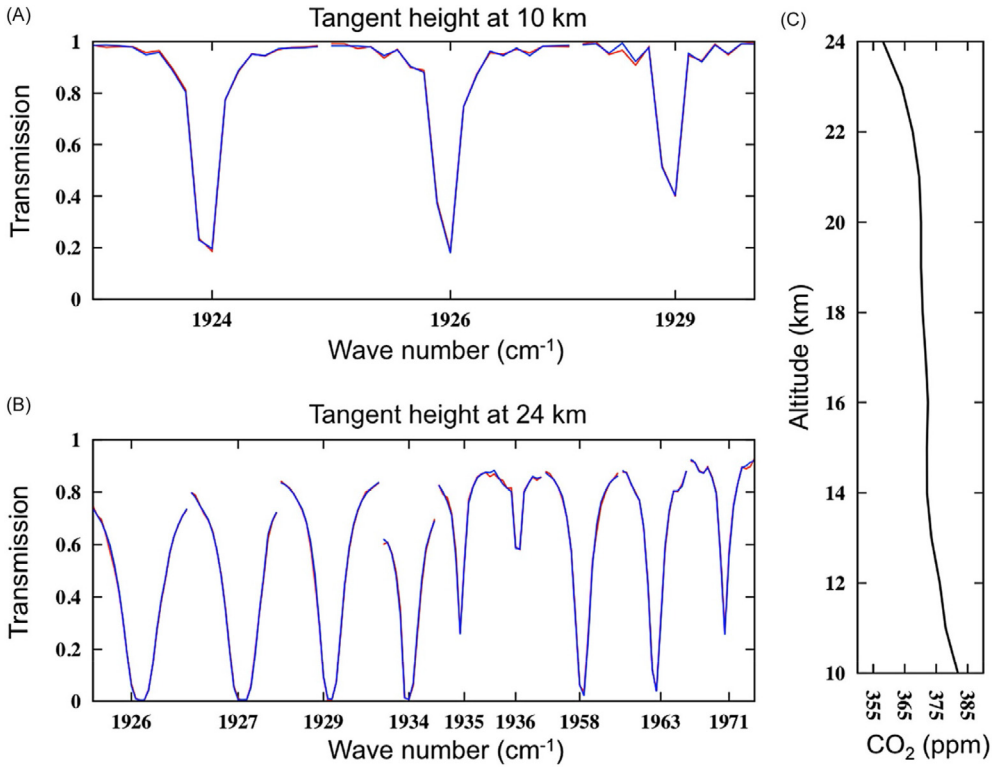

Fig. 20 Example of spectral microwindows selected for the retrieval of a CO_2 profile from ACE-FTS on February 2002 at 60°N (A) Transmission of ACE-FTS as a function of wavenumber for the occultation and for a tangent heights of 10 km. (B) Same as (A) but for a tangent height of 24 km. Note that the microwindows selected at both tangent height are not the same. (C) Retrieved CO_2 profile.

increase in gas concentration), it is required to discard any situation that might be contaminated by clouds or aerosols: gas retrievals are thus performed in clear-sky conditions. Detection procedures can either be based on the sounder observations themselves (e.g., using threshold tests based on differences between channels) or on simultaneous observations from an imager onboard the same platform. It has to be noted that while several cloud detection procedures have been developed since the early age of infrared sounding, it is not the case for aerosols for which detection schemes are not always available. This may impact the retrieval of gas concentration.

An alternative approach to cloud detection is to construct a clear-sky radiance from a group of partially cloudy pixels. The information from adjacent observations (or combined with subpixel information from an imager) is used to construct a clear-sky radiance from a group of partially cloudy pixels. For instance, this approach is used at NOAA in the processing of AIRS and IASI radiances. One difficulty that arises when using cloud-cleared radiances is the complex error characteristics that need to be taken into account in the retrieval.

7.11.4.3 Optimal Estimation Method

7.11.4.3.1 General description

In the Optimal Estimation Method (OEM), which is described in detail by Rodgers (2000), a priori information is used to represent the best statistical knowledge of the state of the atmosphere to be retrieved, prior to any measurement. The purpose of the retrieval is then to find the approximation of the true state of the atmosphere that agrees best with both the measurements and the a priori information.

7.11.4.3.1.1 Formalism

Given the radiative transfer equation, the measurements **y** (radiances of brightness temperatures of selected channels or microwindows) can be expressed according to

$$y = F(x, \beta) + \varepsilon \tag{6}$$

where **F** is the forward radiative transfer function given by Eq. (1), **x** is the state vector (gas column or vertical profile, auxiliary variables), and ε is the measurement noise.

The derivative of the measurement with respect to the gas to be retrieved, the gas Jacobian, or with respect to model parameters will be denoted K and K_β, respectively, and are given by

$$\begin{aligned} k &= \frac{\partial y}{\partial x} \\ k_\beta &= \frac{\partial y}{\partial \beta} \end{aligned} \tag{7}$$

Assuming a linear problem, and representing the a priori information by the mean prior state $\mathbf{x}_a$ and an a priori covariance matrix $\mathbf{S}_a$, the optimal solution can be written as (Rodgers, 2000):

$$\hat{x} = \left(K^T S_\varepsilon^{-1} K + S_a^{-1}\right)\left(K^T S_\varepsilon^{-1} y + S_a^{-1} x_a\right) \tag{8}$$

where S_ε is the measurement covariance matrix.

Introducing the gain and averaging kernels matrices, denoted G and A, respectively, using

$$G = \frac{\partial \hat{x}}{\partial y} = \left(K^T S_\varepsilon^{-1} K + S_a^{-1}\right) K^T S_\varepsilon^{-1} \tag{9}$$

$$A = \frac{\partial \hat{x}}{\partial x} = GK \tag{10}$$

Eq. (6) becomes

$$\hat{x} = x_a + A(x - x_a) + G\left(\varepsilon + K_\beta\left(\beta - \hat{\beta}\right)\right) \tag{11}$$

The retrieval scheme outlined above is generally known as 1D-Var when it is used in an iterative retrieval setup. One of the main problems with using hyperspectral sensors is the huge amount of spectral radiance data points these instruments produce. OEM and other iterative methods require costly forward model calculations at each iteration, and work best when an accurate a priori is available.

7.11.4.3.1.2 Characterization of the retrievals

The characterization of the retrieved quantities in terms of vertical sensitivity and error sources is essential to determine the quality of the results. In the case of the linear approximation, three quantities are particularly used for characterizing the retrieved state: (i) the total error variance–covariance matrix, which gives the a posteriori uncertainty; (ii) the averaging kernels; (iii) the Degrees Of Freedom for Signal (DOFs).

The averaging kernel describes the sensitivity of the retrieval to the true state, as seen by the current observing system. For a profile retrieval, the element $A(i,j)$ of the averaging kernel matrix A is the relative contribution of the element $x(j)$ of the true state to the element $\hat{x}(i)$ of the retrieved state. The remainder information comes from the a priori. A perfect observing system would directly observe each element of the retrieval vector, and the averaging kernel would tend toward the identity matrix. For satellite radiance observations, K is highly nondiagonal and the measurement in a given channel is sensitive to a wide layer of the atmosphere. Moreover, the error in the a priori profile is often highly correlated between levels, so S_ε is also highly nondiagonal. Therefore, the information from the true atmospheric state is smoothed in the vertical by the retrieval system; the averaging kernel describes this smoothing function. The vertical resolution of the retrieved profile can thus be defined as the full width at half maximum of the averaging kernels. The averaging kernel is required for various applications such as assimilation of retrieved products, as it is part of the observation operator (see "Validation" section).

The number of independent elements of information that can be retrieved from the measurement can be estimated through the quantity known as Degrees Of Freedom for Signal (DOFS), which is the trace of the averaging kernel matrix. This concept is quite useful to determine the vertical resolution of products. For instance, a DOFS of 2 means that 2 independent pieces of information of the vertical distribution of the gas can be retrieved from the measurements. DOFS can also be used as a criterion to select channels (see "Selection of individual channels" section).

Finally, the total error variance–covariance matrix S_e can be expressed as the sum of three individual contributions, according to

$$S_e = (I - A)S_a(I - A)^T + GS_\varepsilon G^T + S_{\text{model}} \tag{12}$$

where I is the identity. The first term of Eq. (12) is the smoothing error, which accounts for the vertical sensitivity of the measurements to the retrieved profile and is related to the a priori covariance matrix S_a. The second term is the measurement error, associated with the radiometric noise described by its covariance matrix S_ε. The third term represents the imperfect knowledge of the model parameters.

7.11.4.3.1.3 An example

An example of the OEM is given in **Fig. 21** for the retrieval of CO profiles from IASI observations, which is based on the FORLI code (Hurtmans et al., 2012; Clerbaux et al., 2015). From an a priori profile (**Fig. 21A**) and an a priori variance–covariance matrix (**Fig. 21B**), the OEM aims at minimizing through an iterative process the residual spectrum plotted in **Fig. 21C**, which is the difference between the observed spectrum in the spectral range of 2145–2180 cm^{-1} (where CO absorption lines are located) and the simulated spectrum computed by FORLI. **Fig. 21D** shows the departure of the retrieved CO profile from the a priori profile, due to the information provided by IASI. The points of the profile are not independent: **Fig. 21E** shows the averaging kernels associated to the retrieved profiles. In this example, the DOFS is close to 1 meaning that all points are representative of the same part of the atmosphere.

Even though the averaging kernel matrix is unitless and the degrees of freedom for signal the same whatever the unit of the profile is the shape of the averaging kernels depends on the unit. For instance, **Fig. 22** shows the difference of an averaging kernel matrix associated with the retrieval of CO from IASI calculated from profiles given in molecules cm^{-2} and from profiles given in volume mixing ratio (here in ppb). The impact of the change in unit is well seen when pressure decreases, following the evolution of air density.

7.11.4.3.2 Choice of the a priori: Optimal estimation and Tikhonov regularizations

The OEM will always provide the optimum solution that is statistically the most probable based on the existing data that are represented by the a priori covariance matrix S_a. Such retrieval schemes thus always start with some prior estimate of the atmospheric state. The various retrieval schemes used to interpret hyperspectral observations in the thermal infrared mostly differ from the choice of x_a and S_a.

A priori can be derived from climatologies or from recent forecasts of the atmospheric state. In the former case, if S_a provides too loose a constraint, the solution can tend toward the unconstrained least square solution, which can results in jackknifing. Conversely if the constraint is too tight, the solution will follow x_a and get no contribution from the observation. To solve this problem, the introduction of a global inflation parameter λ, which properly scales S_a^{-1}, can help to get a regularized solution (Masiello et al., 2012). In this approach S_a^{-1} is substituted with λS_a^{-1} in Eq. (8) and (12).

In some cases, when no precise a priori covariance matrix is available, or when the constraint of the retrieval needs to be optimized for a particular vertical region, a regularization matrix R can be used instead of the a priori covariance matrix S_a to constrain the solution. This is known as the Tikhonov regularization (Tikhonov, 1963). This method has been applied to the analysis of several limb and nadir infrared sounders (Kulawik et al., 2006; Bowman et al., 2006; Worden et al., 2007; Eremenko et al., 2008; Fischer et al., 2008). The formalism of the OEM and the Tikhonov regularization is globally the same. The difficulty of the latter concerns the construction of regularization matrices that provide physically meaningful results, in particular to avoid excessive or too weak constraints. Whereas the strength of the constraint in the classical regularization method (Tikhonov, 1963; Phillips, 1962) is the same for all the altitudes, it may be dependent of the altitude for particular atmospheric retrieval methods (Doicu et al., 2004; Kulawik et al., 2006).

7.11.4.3.3 Specification of observation error

The observation error usually combines several sources of error that are assigned to the observation rather than to the a priori. The most important sources of error to be accounted for are instrument noise and forward model errors. The correlations between the channels and the error variance also need to be specified.

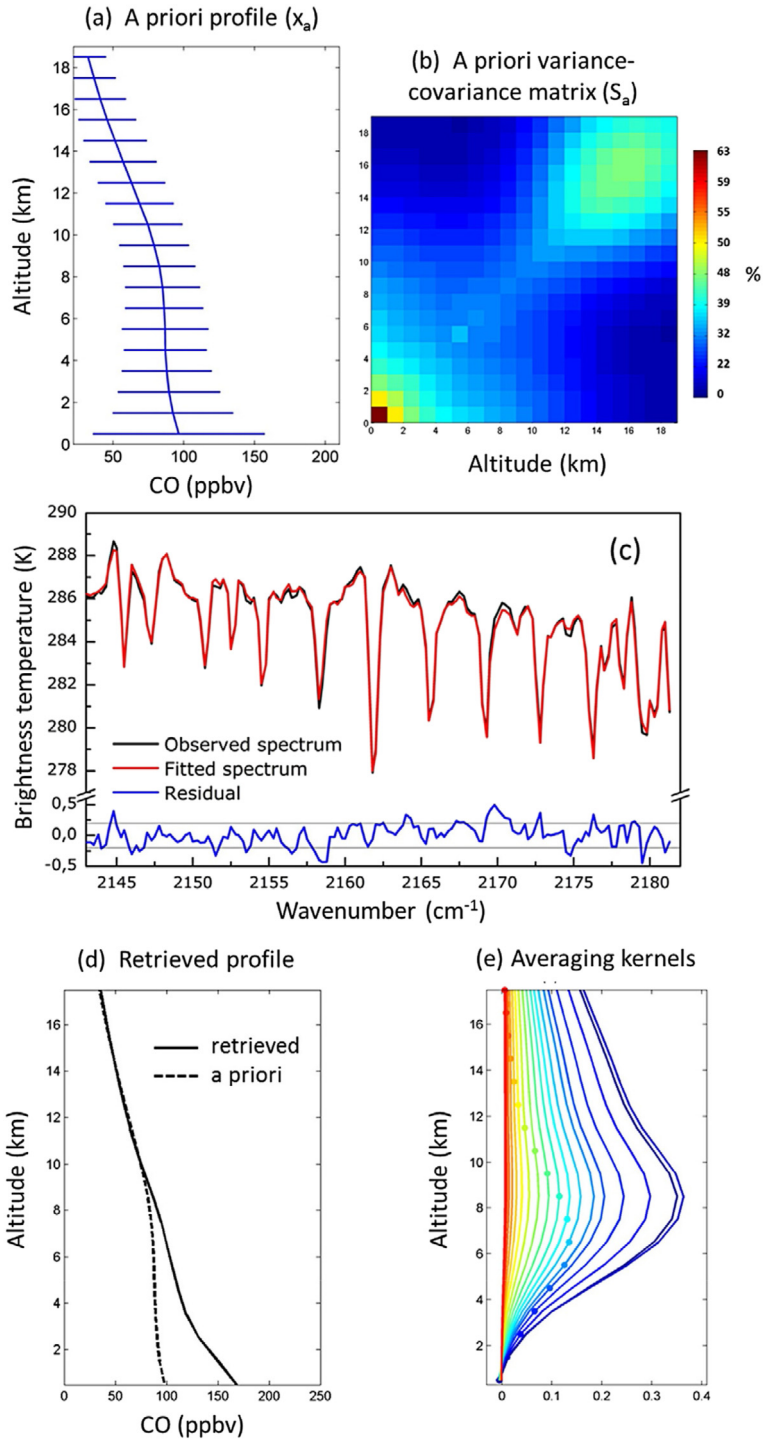

Fig. 21 Retrieval of CO from IASI observations using the FORLI code which is based on the optimal estimation method. See text for details. Courtesy of M. George.

The instrument noise is usually well characterized and provided by space agencies in charge of calibration activities of the instruments. It results from the contribution of several sources, which can either be purely random (i.e., if one were to be able to measure exactly the same scene twice, there would be a small random difference in the measurement) or be pseudorandom (e.g., they depend upon the atmospheric state).

Errors in radiative transfer forward modeling are often hard to estimate directly. They usually include: (i) errors that result from insufficient knowledge of spectroscopy; (ii) errors in the line-by-line modeling; (iii) if a fast model is used, errors introduced by the

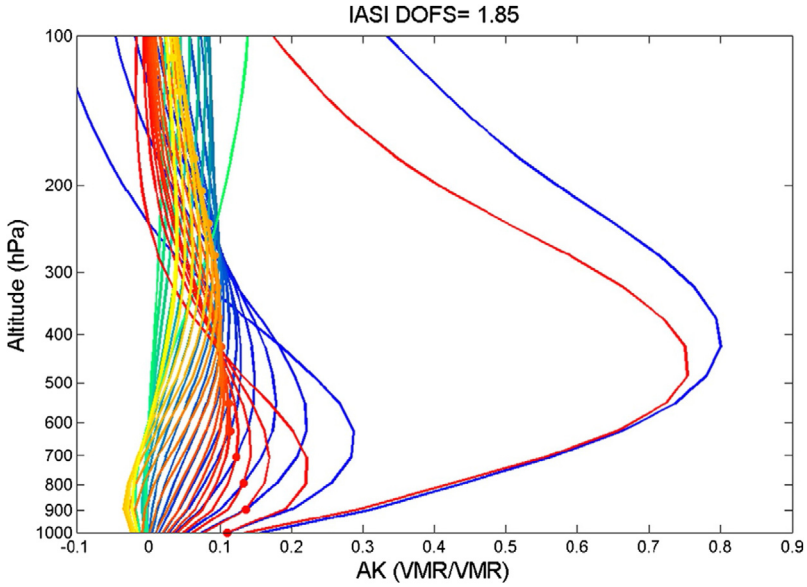

Fig. 22 Example of a representative averaging kernel matrix obtained for the retrieval of CO from IASI (M. George, pers. comm.) when profiles are computed in molecules cm^{-2} (*green-blue colors*) or when profiles are computed in ppb (*yellow-red colors*). The averaging kernel corresponding to the total column (sum of the rows of A) is plotted in blue for the first case and in red for the second case.

parameterization of the line-by-line models the fast model relies on. Intercomparisons of line-by-line models can provide insight into the likely magnitude of spectroscopic errors for certain parts of the spectrum. Overall, forward model errors can be represented by a bias and corrected by a bias correction (see "Radiative bias correction" section). However, the remaining error after bias correction needs to be treated as a random component of the observation error covariance matrix.

Sometimes, the observation error also includes uncertainties related to other parameters, such as interfering species or other atmospheric variables. In that case, use is made of a generalized noise covariance matrix and the state vector is restricted to the species of interest. Rodgers (2000) and von Clarmann et al. (2001) have shown that in a linear optimal estimation, it is equivalent to include all these variables in the state vector. This technique has been applied to the qualitative retrievals of weak absorbers such as NH_3, SO_2, or aerosols (Clarisse et al., 2013; Carboni et al., 2012). The general noise covariance matrix in this case can be built directly from spectra uncontaminated by the species of interest and in this way includes knowledge of uncertain parameters.

7.11.4.4 Nonlinear Inference Schemes Based on Neural Networks

To avoid the linearization of the radiative transfer equation and to deal with signal of the order or lower than the radiometric noise, neural networks (NN) provide a powerful tool to interpret hyperspectral infrared observations in terms of trace gas atmospheric concentrations. They allow the statistical modeling of complex, nonlinear, transfer functions using a probabilistic Bayesian approach, are easily adaptable, and very efficient in terms of computing time in the operational phase. Another advantage of the NN approach is that the error covariances of the training data do not need to be provided explicitly, and thus nonlinear relations can be represented within the NN. A popular type of NN is the Multilayer Perceptron (MLP) neural network (Rumelhart and McClelland, 1986). Several studies have demonstrated that MLP with one or two hidden layers as a class of universal approximators: they can approximate any continuous function uniformly on any compact set provided that sufficient degrees of freedom (equivalent to the number of neurons) are available in the neural architecture (Hornik et al., 1989; Blum and Li, 1991). MLPs have shown to provide good performance in solving problems with geophysical variables (Chéruy et al., 1996; Aires et al., 2001; Chédin et al., 2003b; Crevoisier et al., 2004, 2009a,b; Turquety et al., 2004).

7.11.4.4.1 Neural architecture

A Multilayer Perceptron network is a nonlinear mapping model composed of parallel processors called neurons, which are organized in distinct layers (**Fig. 23**). The first layer represents the input of the mapping. The intermediate layers are called the hidden layers. These layers are connected via neural links: two neurons i and j between two consecutive layers have synaptic connections associated with a synaptic weight $\omega_{i,j}$. Each neuron j executes two simple operations. First it makes a weighted sum of its Nx_i inputs; this sum is then transported through a so-called transfer function, from which the nonlinearity comes from in the model. The classical sigmoidal function is defined as

$$\sigma(x) = \tanh(x) \tag{13}$$

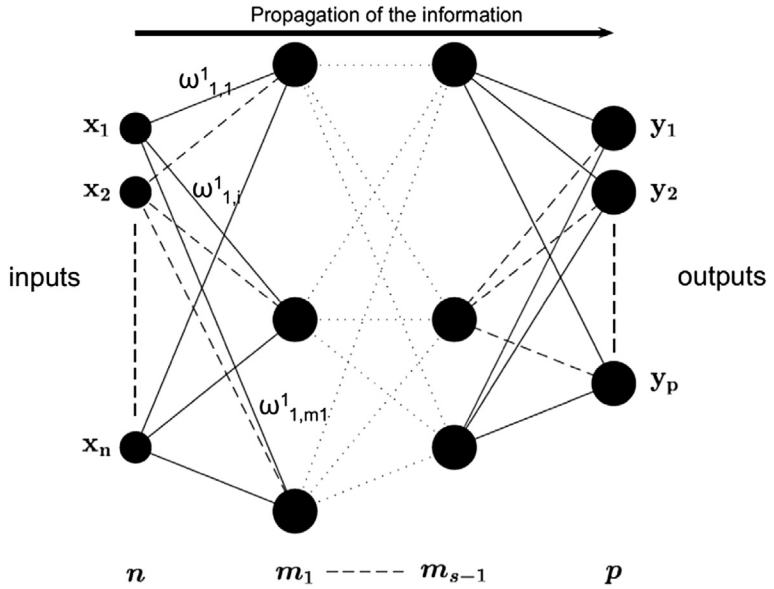

Fig. 23 Multilayer Perceptron with s hidden layers, n inputs, and p outputs. The ith hidden layer is composed of m_i neurons. The link between the kth neuron of the m_i hidden layer and lth neuron of the m_{i+1} layer is denoted by $\omega^{m_i}_{k,l}$.

The output z_j of neuron j in the hidden layer is thus given by

$$z_j = \sigma\left(\sum_{i=1}^{N} \omega_{i,j} x_i\right) \tag{14}$$

Given a neural architecture, all the information of the network is contained in the overall set W of synaptic weights $\omega_{i,j}$. The first step building an efficient neural network is thus to define its architecture, which is defined by a specified number of layers, neurons, and connections. This is done on the basis of empirical considerations, which depend on the complexity of the function associated with the physical problem to solve (Bishop, 1995).

It has to be noted that NN techniques allow computing analytically the gain function (given by Eq. 12) by derivation of the transfer function, from which the averaging kernels can be computed.

7.11.4.4.2 Learning algorithm

The learning algorithm is the optimization technique that estimates the optimal network parameters W (weights and biases) by minimizing a positive-definite cost function which measures, for a set of representative situations (the learning set) for which inputs (e.g., radiances or brightness temperatures) and outputs (e.g., gas column or profile) are known, the mismatch between the neural network outputs and the desired outputs. This is done by modifying the parameter weights and bias values. The weights and biases are first initialized to random values. Then the square of the differences between the desired and the calculated outputs over the whole training dataset is minimized through an iterative gradient descent procedure, and the parameter matrix W is modified accordingly. This requires a long computation time because of the minimization process.

To minimize the cost function, use is often made of the Error Back-Propagation algorithm (Rumelhart and McClelland, 1986). It is a gradient descent algorithm well adapted to the MLP hierarchical architecture because the computational cost is linearly related to the number of parameters. To avoid being trapped in local minima during the minimization of the cost function, stochastic steepest descent can be used. In that case, the learning phase is made sample by sample, chosen iteratively and stochastically in the learning data set.

Once the network is trained, the weights and biases are held fixed and the network is ready to operate.

7.11.4.4.3 Training and evaluation datasets

Neural techniques allow an approximation of the transfer function F of Eq. (6) which links the inputs to the outputs of the problem. This approximation, based on statistical theory, requires a comprehensive dataset of known examples, representative of the behavior of the function to be estimated. This dataset summarizes the physics of the problem to be solved, which include the forward modeling and the a priori known realistic variation range of the state to be retrieved. This training dataset is used for the fitting of the NN parameters W, during the training phase.

In addition, a validation dataset is needed in order to check the generalization capacities of the NN during the training phase and evaluate the performance of the inversion. In particular, too many iterations could induce an overfitting situation, which would result in a NN estimation reproducing perfectly the known situations of the training database but with no generalization capacity.

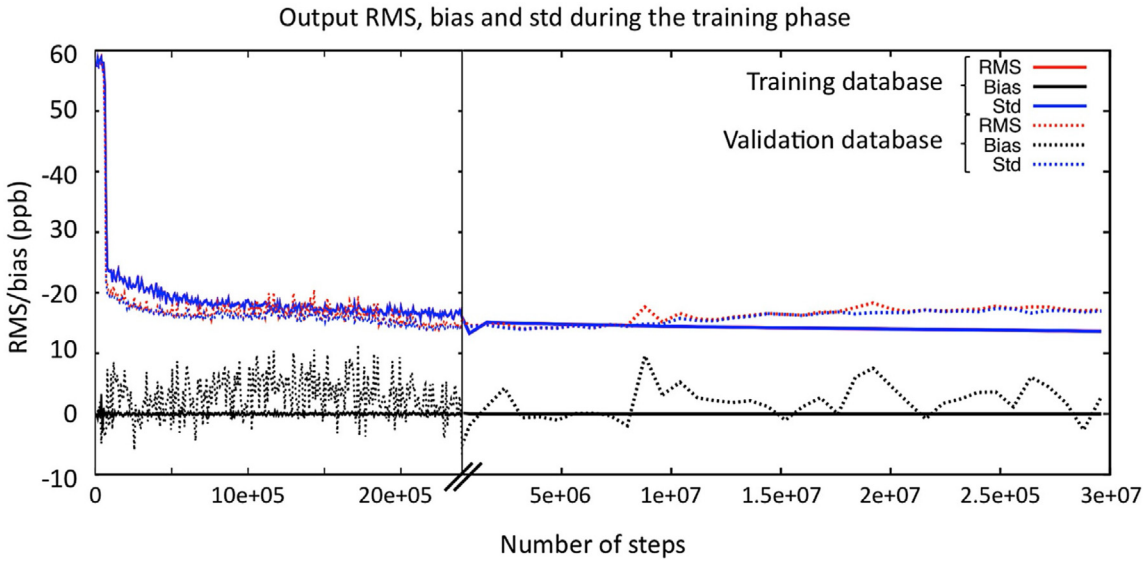

Fig. 24 Evolution, as a function of iteration steps, of the RMS (*red*), bias (*black*), and standard deviation (*blue*) of the difference between the known and estimated state vector (here CH_4 mid-tropospheric column in ppb) computed over the training database (*full lines*) and the validation database (*dashed lines*) used to retrieve CH_4 columns from IASI observations as described in Crevoisier et al. (2009b).

Fig. 24 illustrates this for the retrieval of CH_4 from IASI, which is based on a neural inference scheme (Crevoisier et al., 2009b). It shows the evolution of the RMS (red), bias (black), and standard deviation (blue) of the difference between the known CH_4 mixing ratio from the training database (full lines) and the validation database (dashed lines), during the training phase. At each step, the weights and biases are updated. The beginning of the training phase is characterized by large RMS values, which then rapidly decrease. At one point, around 5e+06 steps, it can be seen that, while the RMS keeps decreasing and the bias remains null when computed over the training dataset, the RMS and bias computed on the validation dataset start increasing, which is typical of an overfitting situation. In this example, the training phase is stopped at 5e+06 steps.

7.11.4.5 Radiative Bias Correction

Retrieval schemes always rely on the combination of simulated radiances, computed by a forward radiative transfer code, and observed radiances. In the case of optimal estimation, the difference between simulated and observed radiances is minimized though an iterative optimization method. In the case of NN, the networks are usually trained with simulated radiances from the learning dataset, and then applied to observations.

Therefore, any radiative biases between observed and simulated radiances that are not only due to the difference between the assumed state of the atmosphere (a priori, learning database) and the real one could impact the retrieval performance. Such biases could result from improper characterization of the instrument or from the forward modeling. Since the underlying assumption of any OEM/NN scheme is that there is no bias between the observation and the prior information, any remaining bias will result in a retrieval that does not provide the best representation of the true atmospheric state. Removing the systematic radiative biases between observation and simulations is thus required. However, this crucial step is particularly challenging since the major source of uncertainty concerning bias correction is the lack of information about the source of the bias.

For standalone retrieval schemes, particularly the ones using climatological a priori, it is possible to include the bias in the state vector; however, the problem is usually significantly underdetermined.

To determine more precisely these biases, observations can be compared with simulations from a forward model over an extended set of known observations. This is the approach chosen for the Spectroscopic Parameter and Radiative Transfer Evaluation (SPARTE) chain (Armante et al., 2016), which relies on hundred of comparisons between clear sky calculated and observed radiances, so-called calculated–observed spectra residuals. The first step consists in colocating in time and space (based on given criteria) observed radiance spectra with well-described atmospheric situations. For each radiance–atmosphere pair, the atmospheric state, which typically includes atmospheric profiles of temperature, water vapor, and several trace gases, as well as surface characteristics (surface temperature, pressure, emissivity), is used as input to a radiative transfer code to compute simulated radiances. The last step consists in computing the mean and standard deviation of the difference between calculated and observed radiances, the "calculated–observed" residuals, over the hundreds of situations contained in the collocation database. Averaging hundreds of situations together minimizes the simulation errors linked to the nonperfect description of the atmospheric state and enables the detection of spectral signatures that are related either to systematic errors in the spectral line calculation (spectroscopic parameters, line shape, line mixing, continua, etc.) or to improper characterization of the instrument.

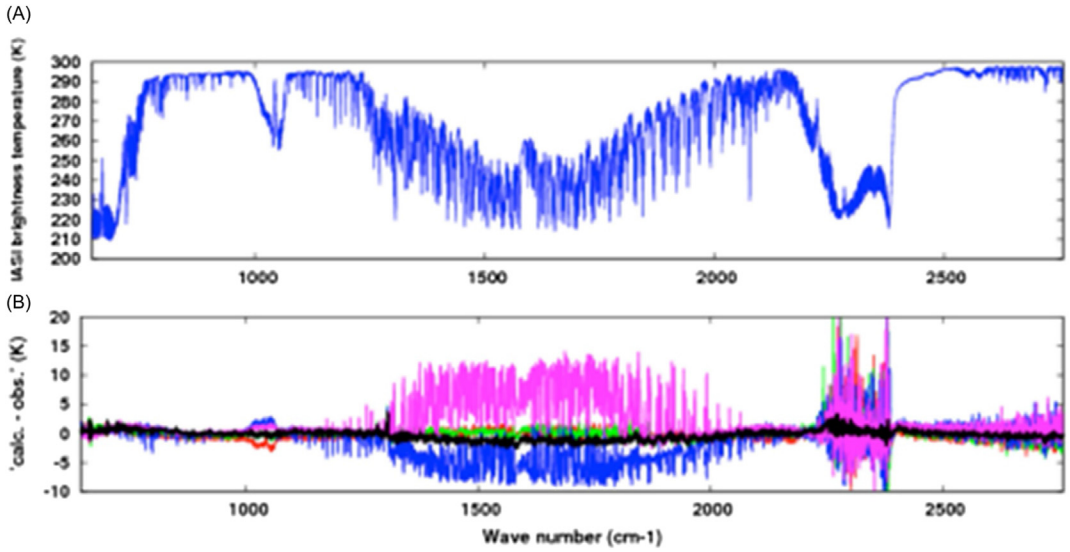

Fig. 25 (A) IASI spectrum averaged over the July 2007–June 2015 for every ARSA tropical situations over sea at night (~12,000 collocations). (B) calculated–observed residuals for five "IASI observation–ARSA situations" pairs randomly taken (*colored lines*) and averaged over the whole period (*black curve*) (Armante et al., 2016).

Fig. 25B shows the "calculated–observed" residuals, expressed in terms of brightness temperatures, obtained for five "IASI observation–atmospheric situation" pairs (colored lines) that can be compared with the corresponding IASI spectra (Fig. 25A). Simulations are performed with the 4A model, while the atmospheric situations come from the ARSA database. Also shown in black is the averaged residual computed over thousands of pairs covering the period July 2007–June 2015 (8 years). The individual residuals corresponding to each collocation are strongly affected by two noises: the radiometric noise of the instrument and the "noise" coming from an incomplete characterization of the atmospheric situations. This is particularly well seen between 2200 and 2400 cm^{-1}, which is a region where IASI is characterized by a particularly large radiometric noise: averaging a sufficient number of situations cancels out the radiometric noise (black line); between 1300 and 2100 cm^{-1}, which is a region dominated by H_2O absorption, averaging the residuals cancels out the improper characterization of water vapor profiles stemming from the large variability of atmospheric humidity and the large collocation criteria used in the chain. All together, averaging hundreds of residuals enables extracting significant features much smaller than the instrumental noise itself, and not affected by the incomplete characterization of the atmosphere.

This approach can be used to evaluate biases coming either from the forward modeling or from the improper characterization of the instrument for a given instrument and a given forward model. However, it does not ultimately provide the part of the bias due to the observation and the part due to the forward model. It can thus be combined with another approach which is based on the intercomparison of observed radiances between various instruments. Such a methodology can enable the detection of deviation from one instrument to another and can help separate the bias coming from each instrument, from the one coming from the forward model. These biases are then used in the retrieval process to "correct" the observations.

7.11.4.6 Other Techniques

Apart from the widely used OEM and NN techniques, over approaches have been developed in recent years to exploit the specificities of hyperspectral observations in the thermal infrared.

The high spectral resolution available from the new generation of infrared sounders can be exploited to extract the specific signatures of trace gases. For instance, Thonat et al. (2012) have designed a double-difference approach to retrieve a total column of CO from IASI. The approach relied on the study of differences between two channels presenting similar sensitivities to atmospheric variables but CO. Such a method is particularly well adapted to the 1–0 absorption band of this gas at 2100 cm^{-1} (Fig. 26).

Over techniques exploiting mathematically the instrument concept have been developed, such as the technique of partially scanned interferograms (Grieco et al., 2013). Designed for interpreting observations made by FTIR interferometers, it consists in transforming the radiance spectra back to the interferogram domain where small regions that are mostly sensitive to a single gas can be identified. The retrieval is then performed by directly applying least squares estimation to these small segments of interferometric radiances. One of the main advantages of the technique is that it allows the efficient use of the information contained in all the channels that are available in the absorption bands of a specific gas species. It has been applied to the retrieval of CO, CO_2, CH_4, and N_2O from IASI (Grieco et al., 2013).

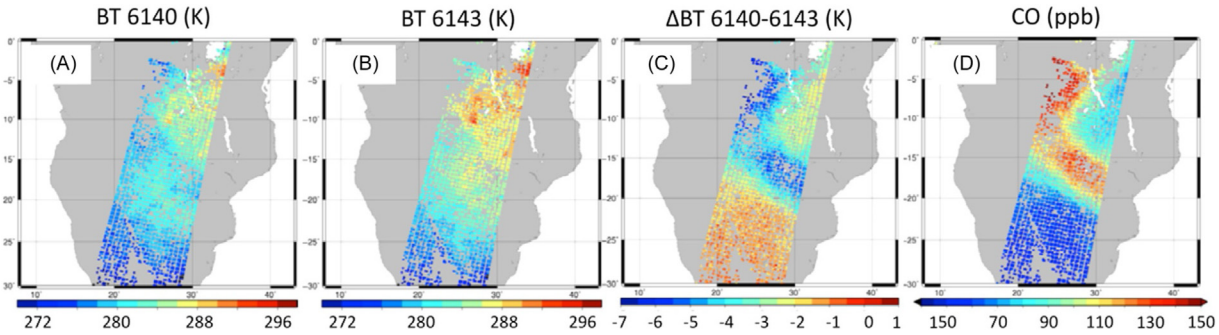

Fig. 26 Retrieval of CO over South Africa using a spectral difference approach. (A) Brightness temperature of IASI channel 6140 (2179.75 cm^{-1}) sensitive to CO and other gases. (B) Same as (A) but for IASI channel 6143 (2180.50 cm^{-1}) presenting the same sensitivities to the atmospheric species and surface characteristics than channel 6140 but with no sensitivity to CO. (C) Difference between both channels: only the CO signal remains. (D) Tropospheric column of CO retrieved from the difference of both channels: a high value of CO corresponds to a negative difference in terms of brightness temperature between the channels (strong absorption for channel 6140, no absorption for channel 6143). Adapted from Thonat, T., Crevoisier, C., Scott, N. A., et al. (2012). Retrieval of tropospheric CO column from hyperspectral infrared sounders—Application to four years of Aqua/AIRS and MetOp-A/IASI. *Atmospheric Measurement Techniques* **5**, 2413–2429. http://dx.doi.org/10.5194/amt-5-2413-2012.

7.11.5 Gas Retrieval Accuracy

The accuracy at which the concentration of a gas can be retrieved from its spectral signature depends on the intensity of the absorption, the location of the absorption (interferences with other gases), and the number of channels available with useful information. It also depends on the instrument specifications, through the spectral resolution and noise level.

7.11.5.1 Impact of Spectral and Radiometric Specifications

7.11.5.1.1 An example: The retrieval of CO columns from infrared sounders

In order to illustrate the impact of spectral resolution and radiometric noise on the retrieval of trace gases, we focus here on the retrieval of CO from two hyperspectral infrared sounders: IASI (resolution of 0.5 cm^{-1}) and IASI-NG (resolution of 0.25 cm^{-1}). Fig. 27 shows a typical spectrum of brightness temperature computed at the resolution of both instruments in the 2143–2181.25 cm^{-1} spectral range, which offers the best compromise between information content and interferences with other gases (De Wachter et al., 2012). By increasing the spectral resolution, the lines are better resolved, yielding an increased information content for CO.

This is confirmed by the study of the sensitivities of the observation to a typical variation of 10 ppb of CO (black line), as shown in Fig. 28. Also shown are the sensitivities of the channels to atmospheric and surface temperature, as well as interfering species (H_2O, N_2O). At the 0.5 cm^{-1} spectral resolution of IASI, the highest sensitivities are of the order of 0.4 K, while they come to

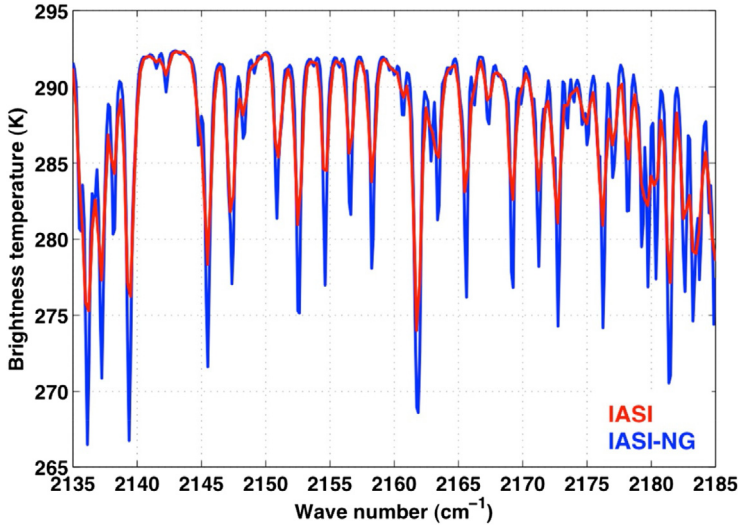

Fig. 27 IASI (*red*) and IASI-NG (*blue*) spectra of brightness temperatures simulated by 4A for a typical tropical situation highlighting the impact of spectral resolution on the CO lines in the 2135–2185 cm^{-1} spectral range.

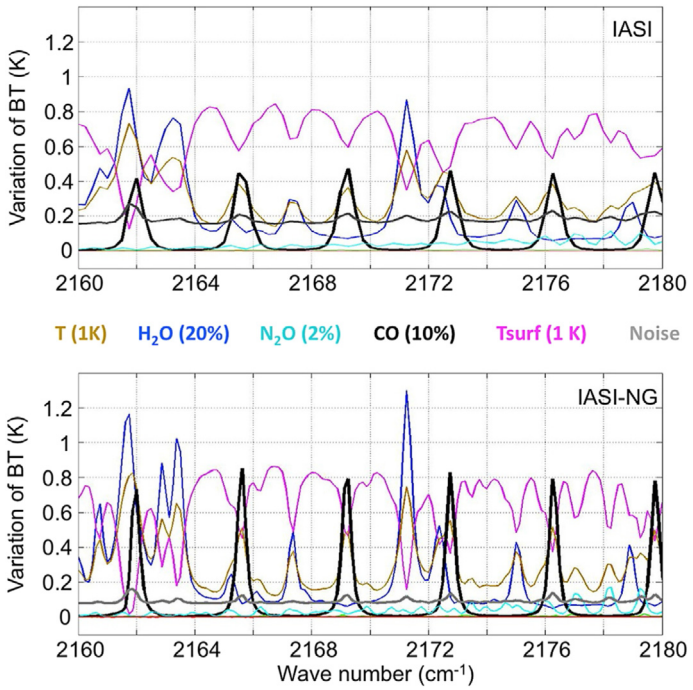

Fig. 28 Variation of brightness temperatures for IASI (*top*) and IASI-NG (*bottom*) due to variation of 1 K of atmospheric temperature (*brown*), 20% of water vapor (*blue*), 2% of nitrous oxide (*cyan*), 10% of carbon monoxide (*black*), 1 K of surface temperature (*pink*). Also shown is the radiometric noise (*grey*).

0.8 K at the IASI-NG resolution of 0.25 cm^{-1}. Combined with a radiometric noise (grey line) divided by about 2 (from 0.2 to 0.1 cm^{-1}) in this spectral range, the signal-to-noise ratio is increased by at least a factor 4 between the instruments.

By applying an OEM retrieval algorithm, with a single parameter (the abundance of CO) being fitted at a time and all the other variables being kept to their known values, it has been shown (Crevoisier et al., 2014) that this increase in the signal-to-noise ratio leads to the improvement of the two major characteristics of the retrieval: (i) DOFs increases from 1.8 for IASI to 2.6 for IASI-NG, on average; (ii) reduction in total column error of ~39% for IASI-NG as compared to IASI. The major improvement concerns the 0–6 km column with a major impact of spectral resolution: the reduction of the error between the two configurations is ~50%.

Fig. 29 shows a generalization of this result: for various configurations of spectral resolution and radiometric noise, DOFs and reduction of the uncertainty in the retrieved CO column (either the 0–12 km tropospheric column or the 0–2 km column

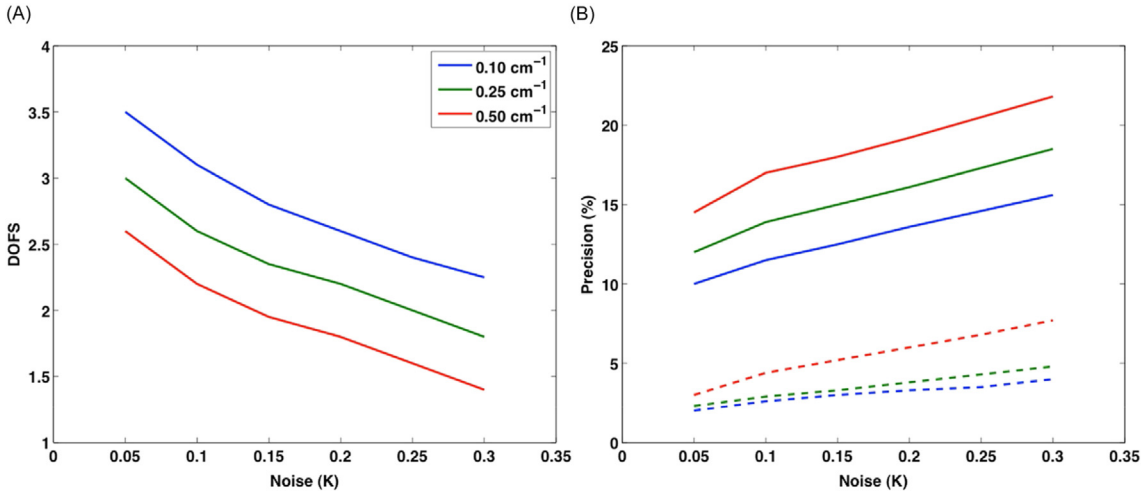

Fig. 29 Impact of spectral resolution and radiometric noise on the retrieval of CO from a nadir-viewing hyperspectral resolution. (A) Evolution of degrees of freedom (DOFS) of the retrieval with the radiometric noise for three spectral resolutions: 0.10 cm^{-1} (*blue*), 0.25 cm^{-1} (*green*), and 0.5 cm^{-1} (*red*). (B) Same as (A) but for the precision of the boundary layer 0–2 km column (*full lines*) and of the free tropospheric 0–12 km column (*dashed lines*).

corresponding to the boundary layer) have been computed. It is important to stress that this results has been obtained with a single parameter (either the CO 0–2 km column or the CO 0–12 km column), being retrieved while all the other variables were kept to their known values. Therefore, the possible effect of an imperfect knowledge in the temperature or interfering gas profile has not been investigated, and the reported errors in the retrieval of columns are solely due to the assumed instrumental specifications.

As seen in Fig. 29, both the improved spectral resolution and the better signal-to-noise lead to better resolved profiles. The impact of spectral resolution is higher than that of radiometric noise for CO. For instance, the reduction of the error is ~30% when improving the spectral resolution by a factor of 2 and keeping the noise at the same level, whereas it is only 25% when the spectral resolution is kept and the noise is reduced by a factor of 2. It can also be noticed that the boundary layer is better sounded when spectral resolution and radiometric noise are improved. However, the precision still remains more than four times higher than the precision on the tropospheric column whatever the configuration is. These theoretical computations are in good agreement with several comparisons that have been made on the capability of AIRS and IASI instruments to retrieve CO (George et al., 2009; Thonat et al., 2012; Gambacorta et al., 2014).

7.11.5.1.2 Retrieval of strong and weak absorbers

Improving both the spectral resolution and the radiometric noise leads to improvement of vertical resolution, accuracy, and detection threshold for all atmospheric species. In particular, any accuracy can be reached for several combinations of noise level and spectral resolution. The specific impact and importance of both improvements depends on the retrieved variable.

On the one hand, increasing the spectral resolution particularly matters when absorption lines of various gases located in the same spectral range interfere with each other (e.g., H_2O for the retrieval of CO and CH_4). Reducing the interferences thus leads to better accuracy. This is well illustrated by Fig. 30, which shows the typical channel sensitivities to CH_4 at the IASI or IASI-NG spectral resolution. In the ν_4 absorption band, water vapor absorption largely dominates, with mean sensitivities of 1 K for a 20% variation of its mixing ratio. The CH_4 signature for a 10% variation of the gas mixing ratio is similar for both instruments, even if a bit higher (0.2 K) for the latter, with values as high as 1.6 K. However, having a better spectral resolution is a real asset since it allows finding spectral intervals where the CH_4 signal comes out of the H_2O signal: near 1300 cm^{-1}, as for IASI, but also near 1275 cm^{-1} (with a slight contamination by N_2O), 1247 cm^{-1} (with a slight contamination by the surface), or near 1340 cm^{-1}. In these regions, temperature signal is about 0.8–0.9 K, and the radiometric noise, which is much lower than the CH_4 signal, does not greatly impact the retrieval. A higher spectral resolution also induces a better vertical resolution thanks to thinner weighting functions and Jacobians (e.g., temperature, CO).

On the other hand, reducing the noise particularly matters for variables for which typical variations of brightness temperatures are of the level or much lower than the radiometric noise (CO_2, N_2O, weak absorbers such as SO_2 and NH_3). Improving the radiometric noise thus yields improved signal-to-noise ratio and translates into more accuracy for the retrieved variables, and more sensitivity lower in the atmosphere (e.g., T, H_2O, O_3). It could also lead to the detection of new "unexpected" species hidden in the noise, especially in intense pollution plumes.

For instance, ammonia (NH_3) absorbs infrared radiation in the ν_2 vibrational band around 950 cm^{-1} (750–1200 cm^{-1}), from which concentrations can be retrieved using inverse methods, as done with TES (Shephard et al., 2011) or IASI (Clarisse et al., 2010). Although daily observations are possible near the largest sources, the absorption signature of NH_3 in the infrared spectra is often of the same magnitude as the noise and the signal only emerges over other regions when averaged over monthly time scales. Since the ammonia absorption is quite broad-band, the key factor for improving the detection capability of an infrared sounder is

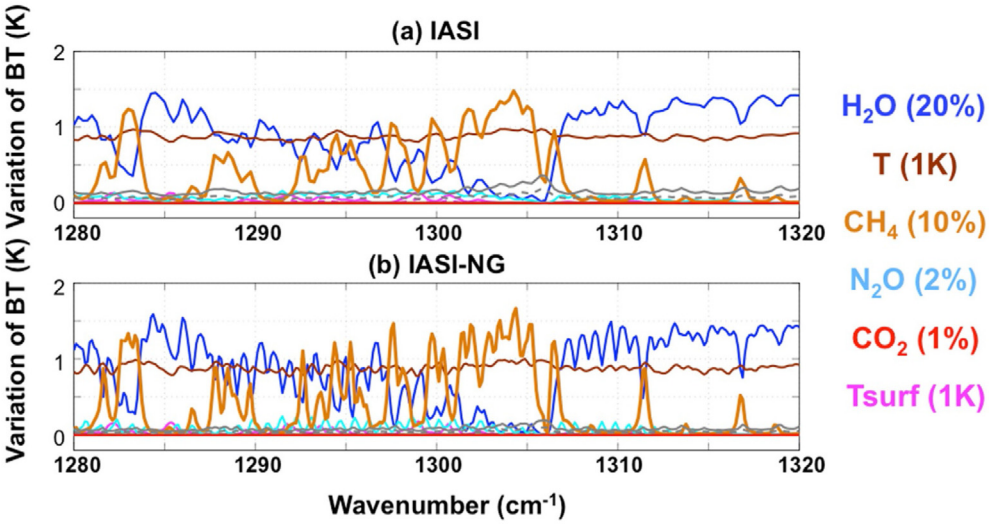

Fig. 30 Impact of spectral resolution on the sensibilities of IASI (resolution of 0.5 cm^{-1}) and IASI-NG (resolution of 0.25 cm^{-1}) channels to perturbation of CH_4 and other atmospheric variable (same as in Fig. 2) in the ν_4 absorption band.

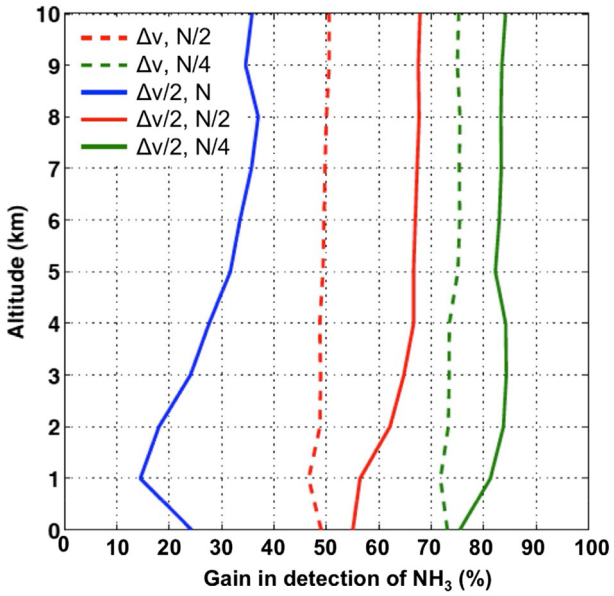

Fig. 31 Relative difference ratio (%) between the detection limit of NH_3 of each instrument configuration compared to the current spectral ($\Delta\nu = 0.5\ cm^{-1}$) and noise ($N = 0.2$ K in the 967.3 cm^{-1} band) of IASI, as a function of altitude, for a case representative of a tropical atmospheric situation. Improvement of the spectral resolution by a factor of 2 compared to IASI is shown in full lines. Adapted from Crevoisier, C., Clerbaux, C., Guidard, V., et al. (2014). Towards IASI-new generation (IASI-NG): Impact of improved spectral resolution and radiometric noise on the retrieval of thermodynamic, chemistry and climate variables. *Atmospheric Measurement Techniques* **7**, 4367–4385. http://dx.doi.org/10.5194/amt-7-4367-2014.

more the noise level than the spectral resolution. This is illustrated by Fig. 31. Simulations were performed using the intense NH_3 feature around 967.3 cm^{-1} (Clarisse et al., 2010) and using increments of concentration for NH_3, with different spectral and radiometric characteristics.

It is well seen in Fig. 31 that an improvement of radiometric noise has a much higher impact than an improvement in the spectral resolution. For instance, a factor of 2 improvement in the spectral resolution leads to a 25% gain in detection sensitivity at the surface level (blue line), whereas a factor of 2 improvement in the radiometric noise leads to an improvement of 50% (red dashed line). As NH_3 is only emitted at surface level and rapidly destroyed, most of the improvement is usually found between 0 and 2 km. It has to be stressed that these simulations were made with a thermal contrast equal to zero. Large positive or negative thermal contrasts will improve the conditions of NH_3 detection at near-surface level (see "Retrievals in the boundary layer" section).

7.11.5.2 Retrievals in the Boundary Layer

For a long time, thermal infrared sounders were considered inadequate for near-surface measurements. However, in agreement with the result found in Fig. 19, it has been shown that sensitivity to trace gases (in particular CO, NH_3, and SO_2) (Bauduin et al., 2016, 2017) of thermal nadir measurements near the surface where local pollution occurs is intimately related to the thermal contrast between the surface and the first atmospheric layers (boundary layer).

Bauduin et al. (2017) have shown that increasing thermal contrast values favor the sensitivity to surface CO. This is illustrated by Fig. 32, which plots the total and 0–1 km DOFS values obtained for the retrieval of CO from IASI using an OEM 1D-Var retrieval scheme for various thermal contrast conditions. For large absolute values of thermal contrast, the total DOFS is close to 2, which means that two independent pieces of information are extracted from the radiances in the CO vertical profile.

Thermal contrast determines to what extent one can detect species near the surface, and thus has a direct influence on DOFs. Therefore, the capability of an infrared nadir sounder to probe the lower atmospheric layers strongly depends on the location of the sounding, the temperature of the surface and of the first atmospheric layers, the type of surface (characterized by its emissivity), and also the time of the day. Indeed, the Earth surface either heats up or cools down faster than the atmosphere, which results in a larger diurnal variation for the surface than for the atmosphere: thermal contrast is thus more pronounced during day than night. Thermal contrasts are generally highest over land during the day and lowest over water at night. This, along with the instrumental characteristics (spectral resolution and radiometric noise), determines the amount of vertical information that can be retrieved for a given species in the nadir geometry.

7.11.5.3 Validation

Validation is an important step to assess the reliability of the gas distribution retrieved from spaceborne instruments. Several sources of data can be used to evaluate the retrieved profiles or columns: concentration products from other spaceborne instruments, in-situ profiles measured by aircraft or balloons, remote-sensing products from ground-based instruments, or model simulations.

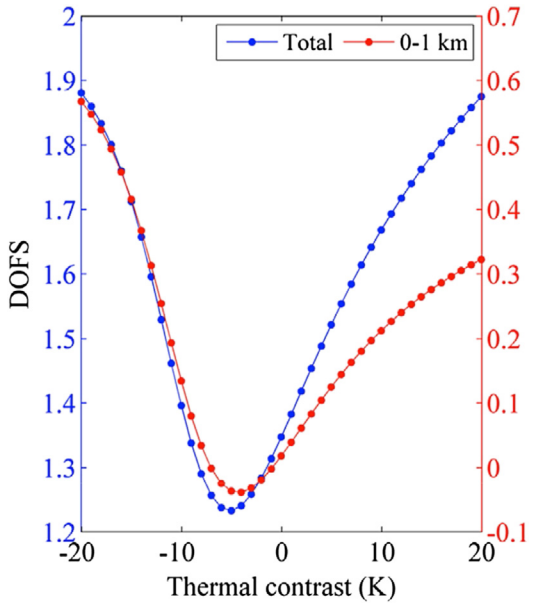

Fig. 32 Evolution of DOFS for the retrieval of a total column (*blue*) and 0–1 km column (*red*) as a function of thermal contrast obtained during a theoretical characterization of CO retrievals from IASI at near-surface level. Adapted from Bauduin, S., Clarisse, L., Theunissen, M., et al. (2017). IASI's sensitivity to near-surface carbon monoxide (CO): Theoretical analyses and retrievals on test cases. *Journal of Quantitative Spectroscopy and Radiative Transfer*, **189**, 428–440. http://dx.doi.org/10.1016/j.jqsrt.2016.12.022

7.11.5.3.1 Intercomparison of concentration products

Comparing two concentration products (profiles on a given pressure grid, partial, or total columns) from two datasets requires taking into account several differences that can originate from: (i) the measurement techniques; (ii) the different vertical sensitivities of the instruments; (iii) the time of the measurements; (iv) the geometry of the measurements (field of view size, grid resolution, etc.); (v) the underlying assumption of the retrieval algorithms (in particular the a priori assumptions); (vi) the inputs used in the retrieval process (such as auxiliary temperature, humidity, surface emissivity, etc.).

The formalism of the Optimal Estimation Method (see "Optimal Estimation Method" section) provides a way to perform this comparison (Rodgers, 2000). The profile retrieved from the instrument with the higher profiling capability, denoted $\hat{x}^{high}$, has to be smoothed to the vertical resolution of the profile retrieved from the instrument with the lowest vertical sensibility, by convoluting it with the averaging kernel functions of the latter, denoted by A^{low}, according to:

$$\hat{x}^{high}_{smoothed} = x_a^{low} + A^{low}\left(\hat{x}^{high} - x_a^{low}\right) \tag{15}$$

where $\hat{x}^{high}_{smoothed}$ is the smoothed high-resolution profile, and $x_a{}^{low}$ is the a priori profile used for the retrieval of the low-resolution profile.

Eq. (15) can be used in various intercomparison exercises: in addition to intercomparing two profiles retrieved from two different instruments (space-borne (George et al., 2015), air-borne or ground-based) or by an instrument and a model simulation, the high-resolution profile can be an in situ profile measured by an airborne instrument or a profile simulated by a model, the low profile being then the one retrieved from the infrared sounder.

7.11.5.3.2 Validation using auxiliary datasets

It has to be stressed that direct validation of gas retrievals is difficult due to the lack of measurements of several species. This is particularly true for reactive gases active in the stratosphere, for which only few stratospheric balloons equipped with measurement devices are sporadically available for validation purposes. Commonly used techniques include Fourier Transform spectrometer (FTS) measurements such as the balloon-borne version of MIPAS (Oelhaf et al., 1991), cryogenic samplers (e.g., Schmidt and Khedim, 1991; Engel et al., 2009) to capture air in flasks at different altitudes along the balloon flight to be analyzed at a later stage, and laser diode spectrometers such as the Spectromètre Infra Rouge pour l'Etude de l'Atmosphère par Diode Laser Embarquées (SPIRALE) (Moreau et al., 2005) or Pico-SDLA instruments (Durry et al., 2004; Ghysels et al., 2011; Joly et al., 2007). All these instruments require to be flown on heavy balloon-borne platforms. They can thus not be flown on regular basis.

Most tropospheric gases are monitored by ground-based measurements of surface mixing ratios, such as the Global Greenhouse Gas Reference Network or the WMO Global Atmospheric Watch program. Although the current surface atmospheric measurement networks allow monitoring the average evolution of atmospheric gases, the measured mixing ratios are only representative of what happens at the surface, and they lack sensitivity in the free and upper troposphere where hyperspectral infrared sounders show highest sensitivities to atmospheric gases. Therefore a direct comparison between the measurement made at the surface and the

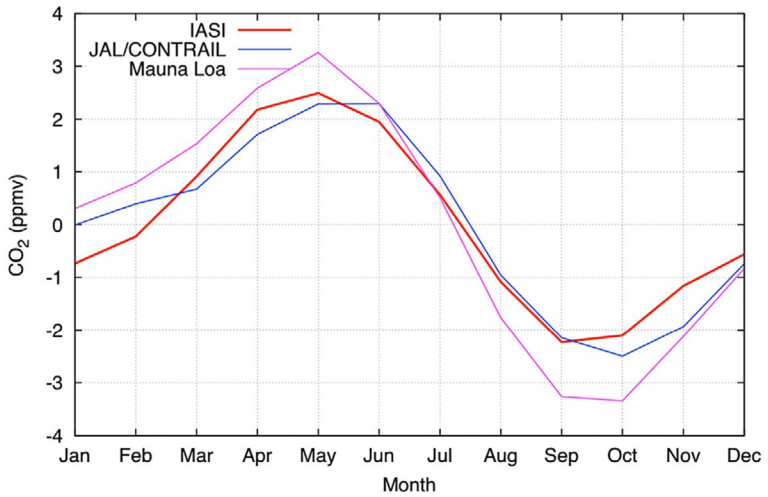

Fig. 33 Detrended CO_2 seasonal cycle as retrieved from IASI/Metop-A (*red*) (Crevoisier et al., 2009a), as measured at ~10 km by aircraft as part of the CONTRAIL program (*blue*) (Machida et al., 2008) and as measured at the surface station of Mauna Loa, Hawaï (*pink*) at ~4 km. Average over 2008–2015.

retrieved gas product is not possible. This is illustrated by **Fig. 33**, which shows the detrended CO_2 seasonal cycle retrieved from IASI (Crevoisier et al., 2009a) and measured at the Mauna Loa station in Hawaï. The cycle measured at the surface is characterized by a larger amplitude and is slightly shifted compared to the cycle retrieved from IASI which is more representative of the mid-troposphere. For species mostly located in the boundary layer (e.g., HNO_3, SO_2), it might be possible to validate the retrieved column in the first atmospheric layers above ground with surface measurements. Other ground-based measurements include remote-sensing techniques such as Brewer–Dobson spectrophotometers (Fioletov et al., 2008) for Total column measurements of O_3, FTIR (Cortesi et al., 2007; Dammers et al., 2016; Pommier et al., 2016), and UV–Vis spectrometer from the Network for the Detection of Atmospheric Composition Change (NDACC, http://www.ndsc.ncep.noaa.gov/) (Dammers et al., 2016; Kerzenmacher et al., 2012).

Ground-based measurements are completed by aircraft measurements that contribute to provide vertical information with regular measurements along commercial airlines. Two programs have particularly been used to evaluate retrieved gas column from hyperspectral infrared sounders: the CONTRAIL project (Machida et al., 2008) that has been used to validate CO_2 and CH_4 columns retrieved from AIRS (Crevoisier et al., 2009a), IASI (Crevoisier et al., 2009a, 2013, 2017; Xiong et al., 2013), and TANSO-FTS (Saitoh et al., 2016) and the CARIBIC project (Schuck et al., 2009) that has been used to evaluate reactive gases (e.g., Thonat et al., 2012). Measurements are performed mostly at an altitude of 10–12 km along the flight track, close to the maximum sensitivity of infrared sounders to greenhouse gases. This explains in particular the good agreement between IASI and CONTRAIL CO_2 seasonality show in **Fig. 33**. Although they can provide information on local gradients and background values, they nonetheless lack information on the vertical to fully validate total or partial columns retrieved from spaceborne missions.

Other less regular aircraft campaigns are also dedicated to study trace gases, and mostly greenhouse gases, at a local scale, by providing vertical profiles of gas mixing ratios (Zhang et al., 2014; Chen et al., 2010; Karion et al., 2013; Crevoisier et al., 2006, 2010; Sweeney et al., 2015) or from pole to pole such as the HIPPO project (Wofsy, 2011). Such vertical profiles are usually limited to 12 km, but they have been used to evaluate gas columns retrieved from space (Maddy and Barnet, 2008; Xiong et al., 2008, 2013; Kulawik et al., 2013; Crevoisier et al., 2017).

In such an exercise, use is made of the approach detailed in "Intercomparison of concentration products" section: the high-resolution profile is the profile measured by an air-borne instrument and the low-resolution profile is the one retrieved from the infrared sounder. However, since aircraft profiles are generally available up to 10–12 km, it is required to extrapolate the upper part of the profile in order to cover the full extent of the averaging kernels. Use is usually made of either climatological knowledge or profiles simulated by atmospheric transport models. However, this step can impact the comparison since any error in the extrapolated profile can lead to biases in the comparison and thus invalidate the comparison. This is illustrated by **Fig. 34** which shows several CH_4 profiles either measured by air-borne instruments or simulated by atmospheric transport models. **Fig. 34C** shows the typical averaging kernel associated to the retrieval of mid-tropospheric columns from IASI in the northern hemisphere (Crevoisier et al., 2017). The aircraft profiles, acquired during the first HIPPO campaign in January 2009 (red in **Fig. 34A**) extends from the surface to about 10 km and does not cover the whole part of the atmosphere seen by IASI (**Fig. 34C**). The aircraft profiles can be extended with profiles simulated by atmospheric transport models at the time and place of the measurement. However, as seen in **Fig. 34B**, there are some differences between the profiles simulated by the available models, such as LMDz (P. Bousquet, pers. comm.) or TM5 (S. Houweling, pers. comm.). The uncertainty associated to the higher part of the simutaled profiles induces an uncertainty in the comparison between the simulated (based on the extrapolated profile) and retrieved column of CH_4.

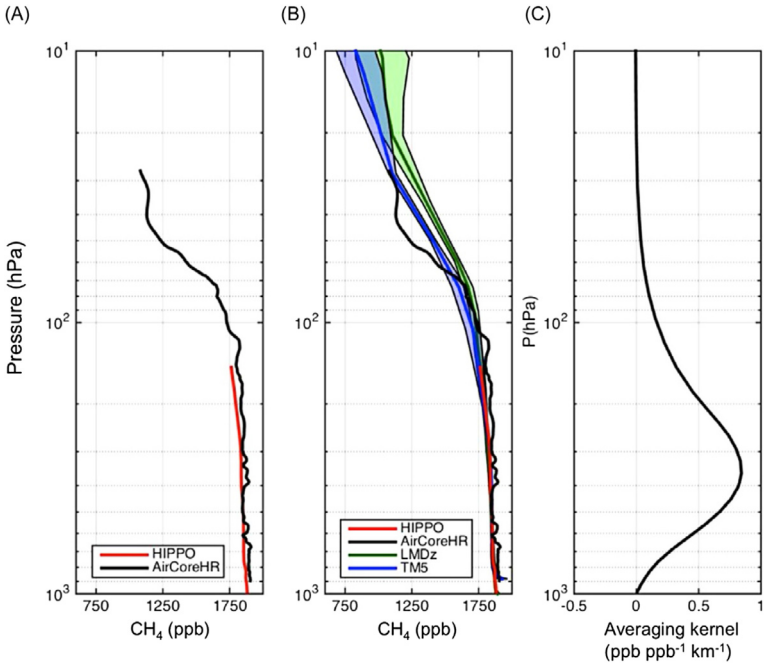

Fig. 34 (A) CH_4 profile measured by the AirCore-HR (Membrive et al., 2017) balloon-borne instrument at Timmins Ontario in August 2014 (*black*) and average profile measured in the northern Pacific during the HIPPO-1 aircraft campaign in January 2009. (B) Same as (A) but with simulated profiles from the LMDz (*green*) and the TM5 (*blue*) atmospheric transport models. (C) IASI CH_4 averaging kernel associated with the retrieval of a mid-tropospheric column.

Ultimately, extended measurements of vertical profiles are needed in order to perform a full validation of profiles or columns retrieved from hyperspectral infrared instruments. Ozonesondes have been extensively used to validate ozone columns retrieved from spaceborne observations (e.g. Boynard et al., 2016). For other trace gases, new systems are being developed. For instance, the AirCore atmospheric sampler (Karion et al., 2010; Membrive et al., 2017) allows balloon measurements of gas vertical profiles from the surface up to approximately 30 km (**Fig. 34A**) and can be used to validate columns retrieved from nadir-viewing

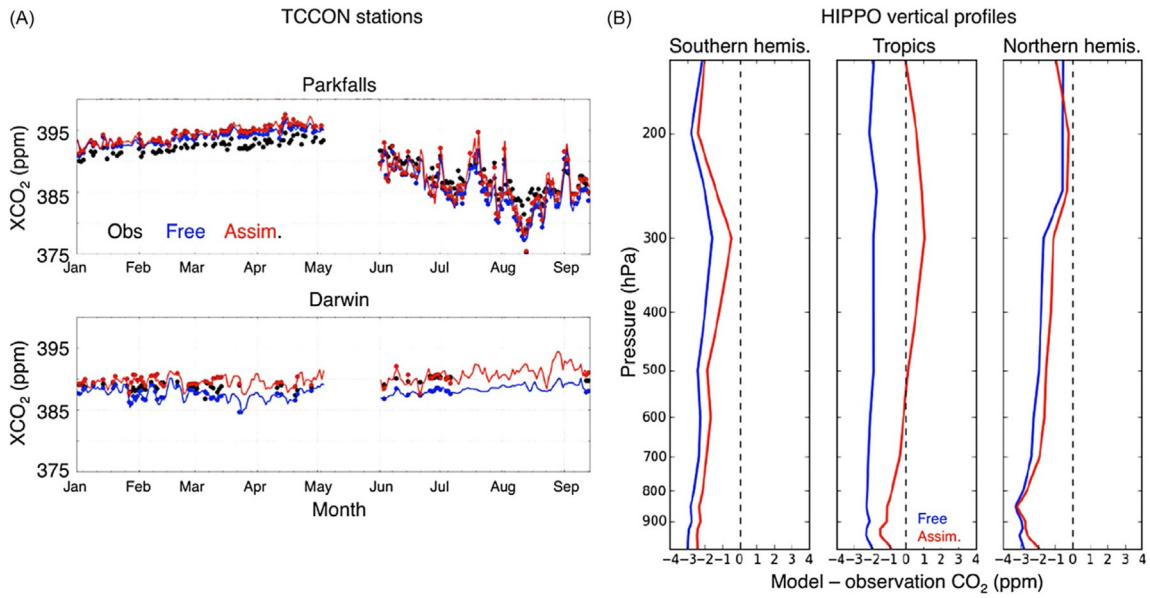

Fig. 35 Evaluation of the assimilation of IASI CO_2 mid-tropospheric columns within the CAMS C-IFS model by comparing two configurations of the model: one for which IASI CO_2 fields have been assimilated (*red*) and the other without assimilation (*blue*). (A) Evaluation of the two configurations against CO_2 total columns (*black dots*) measured at 2 TCCON stations in Park Falls and Darwin from January to September 2010. (B) Evaluation of the two configurations against CO_2 vertical profiles measured during the HIPPO 5 campaign. In both cases, the assimilation of IASI CO_2 improves the comparison with the ground-based or aircraft measurements.

instruments, or profiles retrieved from limb-viewing instruments. Such atmospheric samplers that can be flown from weather balloons could be deployed at various locations to complete an effective system together with ground stations and regular aircraft campaigns. The spatial and temporal resolution requirements necessary to evaluate the satellite retrievals efficiently need to be assessed.

Indirect validation can also be performed using data assimilation, which is a powerful tool for analysis of observations provided by instruments that have different spatial, temporal, and vertical resolutions (e.g., Clerbaux et al., 2003; Massart et al., 2014). In this approach, the gas distribution simulated by a given atmospheric transport and chemistry model is compared to in-situ observations of the gas at specific locations and times, in two configurations: for a reference configuration, based on up-to-date knowledge of the gas sources and sinks, and for an assimilation run, for which the retrieved gas concentration are assimilated by the model. **Fig. 35** shows the evaluation of the assimilation of CO_2 mid-tropospheric columns retrieved from IASI (Crevoisier et al., 2009a,b) within the CAMS C-IFS model (Massart et al., 2014), using measurements of CO_2 total columns at 2 TCCON stations and CO_2 vertical profiles measured during the HIPPO campaign. The improvement of the comparison between the model outputs and the in-situ measurements is an indirect evaluation of the performance of the retrieval process.

Acknowledgments

The author warmly thanks Virginie Capelle and Raymond Armante (LMD) for fruitful discussions and useful comments on the paper. The author is also grateful to Maya Gorge (LATMOS), Pierre Coheur and Sophie Baudoin (ULB), Tom Pagano and Joao Teixer (NASA/JPL), Antonia Gambacorta and Flavio Iturbide Sanchez (NOAA/NESDIS/STAR), Frédéric Bernard (CNES), Agnès Perrin and Marco Ridolfi, and Sébastien Massart (ECMWF) for providing materials for the several figures presented in this paper.

See also: 7.04. Atmospheric Soundings From Hyperspectral Satellite Observations.

References

Aires, F., Prigent, C., Rossow, W. B., et al. (2001). A new neural network approach including first guess for retrieval of atmospheric water vapor, cloud liquid water path, surface temperature, and emissivities over land from satellite microwave observations. *Journal of Geophysical Research. Atmospheres, 106*, 14887–14907. http://dx.doi.org/10.1029/2001JD900085.

Amato, U., Masiello, G., Serio, C., et al. (2002). The σ-IASI code for the calculation of infrared atmospheric radiance and its derivatives. *Environmental Modelling and Software, 17*, 651–667. http://dx.doi.org/10.1016/S1364-8152(02)00027-0.

Armante, R., Scott, N., Crevoisier, C., et al. (2016). Evaluation of spectroscopic databases through radiative transfer simulations compared to observations. Application to the validation of GEISA 2015 with IASI and TCCON. *Journal of Molecular Spectroscopy, 327*, 180–192. http://dx.doi.org/10.1016/j.jms.2016.04.004.

Aumann, H. H., Chahine, M. T., Gautier, C., et al. (2003). AIRS/AMSU/HSB on the aqua mission: Design, science objectives, data products, and processing systems. *IEEE Transactions on Geoscience and Remote Sensing, 41*, 253–264. http://dx.doi.org/10.1109/TGRS.2002.808356.

Bauduin, S., Clarisse, L., Hadji-Lazaro, J., et al. (2016). Retrieval of near-surface sulfur dioxide (SO_2) concentrations at a global scale using IASI satellite observations. *Atmospheric Measurement Techniques, 9*, 721–740. http://dx.doi.org/10.5194/amt-9-721-2016.

Bauduin, S., Clarisse, L., Theunissen, M., et al. (2017). IASI's sensitivity to near-surface carbon monoxide (CO): Theoretical analyses and retrievals on test cases. *Journal of Quantitative Spectroscopy and Radiative Transfer, 189*, 428–440. http://dx.doi.org/10.1016/j.jqsrt.2016.12.022.

Beer, R., Glavich, T. A., & Rider, D. M. (2001). Tropospheric emission spectrometer for the Earth Observing System's Aura satellite. *Applied Optics, 40*, 2356–2367. http://dx.doi.org/10.1364/AO.40.002356.

Bernath, P. F. (2006). Atmospheric chemistry experiment (ACE): Analytical chemistry from orbit. *TrAC Trends in Analytical Chemistry, 25*, 647–654. http://dx.doi.org/10.1016/j.trac.2006.05.001.

Bernath, P. F. (2017). The atmospheric chemistry experiment (ACE). *Journal of Quantitative Spectroscopy and Radiative Transfer, 186*, 3–16. http://dx.doi.org/10.1016/j.jqsrt.2016.04.006.

Bernath, P. F., McElroy, C. T., Abrams, M. C., et al. (2005). Atmospheric chemistry experiment (ace): Mission overview. *Geophysical Research Letters, 32*, L15S01. http://dx.doi.org/10.1029/2005GL022386.

Bishop, C. M. (1995). *Neural networks for pattern recognition*. New York: Clarendon Press.

Blum, E. K., & Li, L. K. (1991). Approximation theory and feedforward networks. *Neural Networks, 4*, 511–515. http://dx.doi.org/10.1016/0893-6080(91)90047-9.

Boone, C. D., Nassar, R., Walker, K. A., et al. (2005). Retrievals for the atmospheric chemistry experiment Fourier-transform spectrometer. *Applied Optics, 44*, 7218–7231.

Bowman, K. W., Rodgers, C. D., Kulawik, S. S., et al. (2006). Tropospheric emission spectrometer: Retrieval method and error analysis. *IEEE Transactions on Geoscience and Remote Sensing, 44*, 1297–1307. http://dx.doi.org/10.1109/TGRS.2006.871234.

Boynard, A., Clerbaux, C., Coheur, P.-F., et al. (2009). Measurements of total and tropospheric ozone from IASI: Comparison with correlative satellite, ground-based and ozonesonde observations. *Atmospheric Chemistry and Physics, 9*, 6255–6271. http://dx.doi.org/10.5194/acp-9-6255-2009.

Boynard, A., Hurtmans, D., Koukouli, M. E., et al. (2016). Seven years of IASI ozone retrievals from FORLI: Validation with independent total column and vertical profile measurements. *Atmospheric Measurement Techniques, 9*, 4327–4353. http://dx.doi.org/10.5194/amt-9-4327-2016.

Brown, L. R., Chris Benner, D., Malathy Devi, V., et al. (2005). Line mixing in self- and foreign-broadened water vapor at 6 μm. *Journal of Molecular Structure, 742*, 111–122. http://dx.doi.org/10.1016/j.molstruc.2004.12.059.

Capelle, V., Chédin, A., Siméon, M., et al. (2014). Evaluation of IASI-derived dust aerosol characteristics over the tropical belt. *Atmospheric Chemistry and Physics, 14*, 9343–9362. http://dx.doi.org/10.5194/acp-14-9343-2014.

Carboni, E., Thomas, G. E., Sayer, A. M., et al. (2012). Intercomparison of desert dust optical depth from satellite measurements. *Atmospheric Measurement Techniques, 5*, 1973–2002. http://dx.doi.org/10.5194/amt-5-1973-2012.

Carli, B., Ceccherini, S., Gignoli, A., et al. (2004). *Development of an optimised algorithm for routine p,T and VMR retrieval from MIPAS limb emission spectra.*

Chahine, M. T., Chen, L., Dimotakis, P., et al. (2008). Satellite remote sounding of mid-tropospheric CO_2. *Geophysical Research Letters, 35*, L17807. http://dx.doi.org/10.1029/2008GL035022.

Chédin, A., Scott, N. A., Wahiche, C., et al. (1985). The improved initialisation inversion method: A high-resolution physical method for temperature retrievals from the TIROS-N series. *Journal of Climate and Applied Meteorology*. http://dx.doi.org/10.1175/1520-0450(1985)024<0128:TIIIMA>2.0.CO;2.

Chédin, A., Hollingsworth, A., Scott, N. A., et al. (2002). Annual and seasonal variations of atmospheric CO_2, N_2O and CO concentrations retrieved from NOAA/TOVS satellite observations. *Geophysical Research Letters, 29*, 110-1–110-4. http://dx.doi.org/10.1029/2001GL014082.

Chédin, A., Saunders, R., Hollingsworth, A., et al. (2003a). The feasibility of monitoring CO_2 from high-resolution infrared sounders. *Journal of Geophysical Research, 108*, 4064. http://dx.doi.org/10.1029/2001JD001443.

Chédin, A., Serrar, S., Scott, N. A., et al. (2003b). First global measurement of midtropospheric CO_2 from NOAA polar satellites: Tropical zone. *Journal of Geophysical Research, 108*, 4581. http://dx.doi.org/10.1029/2003JD003439.

Chen, H., Winderlich, J., Gerbig, C., et al. (2010). High-accuracy continuous airborne measurements of greenhouse gases CO_2 and CH_4 using the cavity ring-down spectroscopy (CRDS) technique. *Atmospheric Measurement Techniques, 3*, 375–386. http://dx.doi.org/10.5194/amt-3-375-2010.

Chéruy, F., Chevallier, F., Morcrette, J.-J., et al. (1996). A fast method using neural networks for computing the vertical distribution of the thermal component of the Earth radiative budget (in French). *Comptes Rendus de l'Académie des Sciences, 322*.

Chevallier, F. C., Chéruy, F., Scott, N. A., et al. (1998). A neural network approach for a fast and accurate computation of a longwave radiative budget. *Journal of Applied Meteorology, 37*, 1385–1397. http://dx.doi.org/10.1175/1520-0450(1998)037<1385:annafa>2.0.co;2.

Clarisse, L., Clerbaux, C., Dentener, F., et al. (2009). Global ammonia distribution derived from infrared satellite observations. *Nature Geoscience, 2*, 479–483. http://dx.doi.org/10.1038/ngeo551.

Clarisse, L., Hurtmans, D., Prata, A. J., et al. (2010). Retrieving radius, concentration, optical depth, and mass of different types of aerosols from high-resolution infrared nadir spectra. *Applied Optics, 49*, 3713–3722. http://dx.doi.org/10.1364/AO.49.003713.

Clarisse, L., R'Honi, Y., Coheur, P.-F., et al. (2011). Thermal infrared nadir observations of 24 atmospheric gases. *Geophysical Research Letters, 38*. http://dx.doi.org/10.1029/2011GL047271.

Clarisse, L., Coheur, P. F., Prata, F., et al. (2013). A unified approach to infrared aerosol remote sensing and type specification. *Atmospheric Chemistry and Physics, 13*, 2195–2221. http://dx.doi.org/10.5194/acp-13-2195-2013.

Clerbaux, C., & Crevoisier, C. (2013). New directions: Infrared remote sensing of the troposphere from satellite: Less, but better. *Atmospheric Environment*. http://dx.doi.org/10.1016/j.atmosenv.2013.01.057.

Clerbaux, C., Hadji-Lazaro, J., Turquety, S., et al. (2003). Trace gas measurements from infrared satellite for chemistry and climate applications. *Atmospheric Chemistry and Physics, 3*, 1495–1508. http://dx.doi.org/10.5194/acp-3-1495-2003.

Clerbaux, C., Boynard, A., Clarisse, L., et al. (2009). Monitoring of atmospheric composition using the thermal infrared IASI/MetOp sounder. *European Geosciences Union, 9*, 6041–6054.

Clerbaux, C., Hadji-Lazaro, J., Turquety, S., et al. (2015). Tracking pollutants from space: Eight years of IASI satellite observation. *Comptes Rendus Geoscience, 347*, 134–144. http://dx.doi.org/10.1016/j.crte.2015.06.001.

Clough, S. A., Shephard, M. W., Mlawer, E. J., et al. (2005). Atmospheric radiative transfer modeling: A summary of the AER codes. *Journal of Quantitative Spectroscopy and Radiative Transfer*. http://dx.doi.org/10.1016/j.jqsrt.2004.05.058.

Collard, A. D. (2007). Selection of IASI channels for use in numerical weather prediction. *133*, 1977–1991. http://dx.doi.org/10.1002/qj.178.

Cortesi, U., Lambert, J. C., De Clercq, C., et al. (2007). Geophysical validation of MIPAS-ENVISAT operational ozone data. *Atmospheric Chemistry and Physics, 7*, 4807–4867.

Crevoisier, C., Chedin, A., & Scott, N. A. (2003). AIRS channel selection for CO_2 and other trace-gas retrievals. *129*, 2719–2740. http://dx.doi.org/10.1256/qj.02.180.

Crevoisier, C., Heilliette, S., Chédin, A., et al. (2004). Midtropospheric CO_2 concentration retrieval from AIRS observations in the tropics. *Geophysical Research Letters, 31*. http://dx.doi.org/10.1029/2004GL020141.

Crevoisier, C., Chédin, A., Matsueda, A., et al. (2009a). First year of upper tropospheric integrated content of CO_2 from IASI hyperspectral infrared observations. *Atmospheric Chemistry and Physics, 9*, 4797–4810.

Crevoisier, C., Nobileau, D., Fiore, A., et al. (2009b). Tropospheric methane in the tropics—First year from IASI hyperspectral infrared observations. *Atmospheric Chemistry and Physics, 9*, 6337–6350.

Crevoisier, C., Sweeney, C., Gloor, M., et al. (2010). Insight on regional US carbon sinks from three-dimensional atmospheric CO_2 sampling. *Proceedings of the National Academy of Sciences of the United States of America, 107*, 18348–18353. http://dx.doi.org/10.1073/pnas.0900062107.

Crevoisier, C., Nobileau, D., Armante, R., et al. (2013). The 2007–2011 evolution of tropical methane in the mid-troposphere as seen from space by MetOp-A/IASI. *Atmospheric Chemistry and Physics, 13*, 4279–4289. http://dx.doi.org/10.5194/acp-13-4279-2013.

Crevoisier, C., Clerbaux, C., Guidard, V., et al. (2014). Towards IASI-new generation (IASI-NG): Impact of improved spectral resolution and radiometric noise on the retrieval of thermodynamic, chemistry and climate variables. *Atmospheric Measurement Techniques, 7*, 4367–4385. http://dx.doi.org/10.5194/amt-7-4367-2014.

Crevoisier, C., Meilhac, N., Membrive, O., et al. (2017). Establishing long time series of global mid-tropospheric columns of CH_4 with IASI and AMSU onboard successive Metop platforms. *Remote Sensing of Environment*.

Dammers, E., et al. (2016). An evaluation of IASI-NH_3 with ground-based Fourier transform infrared spectroscopy measurements. *Atmospheric Chemistry and Physics, 16*, 10351–10368. http://dx.doi.org/10.5194/acp-16-10351-2016.

De Maziere, M., Hennen, O., Van Roozendael, M., et al. (1999). Daily ozone vertical profile model built on geophysical grounds, for column retrieval from atmospheric high-resolution infrared spectra. *Journal of Geophysical Research. Atmospheres, 104*, 23855–23869. http://dx.doi.org/10.1029/1999JD900347.

De Wachter, E., Barret, B., Le Flochmoën, E., et al. (2012). Retrieval of MetOp-A/IASI CO profiles and validation with MOZAIC data. *Atmospheric Measurement Techniques, 5*, 2843–2857. http://dx.doi.org/10.5194/amt-5-2843-2012.

Deeter, M. N., Edwards, D. P., Gille, J. C., et al. (2007). Sensitivity of MOPITT observations to carbon monoxide in the lower troposphere. *Journal of Geophysical Research, 112*, D24306. http://dx.doi.org/10.1029/2007JD008929.

DeSouza-Machado, S., Strow, L. L., & Hannon, S. E. (1997). kCompressed atmospheric radiative transfer algorithm (kCARTA). In J. D. Haigh (Ed.)*Proc. SPIE 3220* (p. 156). http://dx.doi.org/10.1117/12.301147. International Society for Optics and Photonics.

Doicu, A., Schreier, F., & Hess, M. (2004). Iterative regularization methods for atmospheric remote sensing. *Journal of Quantitative Spectroscopy and Radiative Transfer, 83*, 47–61. http://dx.doi.org/10.1016/S0022-4073(02)00292-3.

Dudhia, A. (1997). *RFM v3 software user's manual, technical report*. Oxford: Dep. of Atmos, Oceanic and Planet. Phys., Univ. of Oxford. ESA Doc. PO-MA-OXF-GS-0003.

Dudhia, A., Jay, V. L., & Rodgers, C. D. (2002). Microwindow selection for high-spectral-resolution sounders. *Applied Optics, 41*, 3665–3673.

Duflot, V., Hurtmans, D., Clarisse, L., et al. (2013). Measurements of hydrogen cyanide (HCN) and acetylene (C_2H_2) from the infrared atmospheric sounding interferometer (IASI). *Atmospheric Measurement Techniques, 6*, 917–925. http://dx.doi.org/10.5194/amt-6-917-2013.

Dufour, G., Eremenko, M., Griesfeller, A., et al. (2012). Validation of three different scientific ozone products retrieved from IASI spectra using ozonesondes. *Atmospheric Measurement Techniques, 5*, 611–630. http://dx.doi.org/10.5194/amt-5-611-2012.

Durry, G., Amarouche, N., Zéninari, V., et al. (2004). In situ sensing of the middle atmosphere with balloonborne near-infrared laser diodes. *Spectrochimica Acta Part A: Molecular Spectroscopy, 60*, 3371–3379. http://dx.doi.org/10.1016/j.saa.2003.11.050.

Edwards, D. (1992). *GENLN2: A general line-by-line atmospheric transmittance and radiance model. Version 3.0 description and users guide*. Boulder, CO: Amospheric Chemistry Division, National Center for Atmospheric Research. http://dx.doi.org/10.5065/D6W37T86.

Engel, A., Möbius, T., Bönisch, H., et al. (2009). Age of stratospheric air unchanged within uncertainties over the past 30 years. *Nature Geoscience, 2*, 28–31. http://dx.doi.org/10.1038/ngeo388.

Eremenko, M., Dufour, G., Foret, G., et al. (2008). Tropospheric ozone distributions over Europe during the heat wave in July 2007 observed from infrared nadir spectra recorded by IASI. *Geophysical Research Letters, 35*, L18805. http://dx.doi.org/10.1029/2008GL034803.

Eresmaa, R., Benedetti, A., & McNally, A. (2012). *Diverse profile database of aerosol and trace gas concentrations from the monitoring atmospheric composition and climate short-range forecasts*.

Fioletov, V. E., Labow, G., Evans, R., et al. (2008). Performance of the ground-based total ozone network assessed using satellite data. *Journal of Geophysical Research, 113*, D14313. http://dx.doi.org/10.1029/2008JD009809.

Fischer, H., & Oelhaf, H. (1996). Remote sensing of vertical profiles of atmospheric trace constituents with MIPAS limb-emission spectrometers. *Applied Optics, 35*, 2787–2796.

Fischer, H., Birk, M., Blom, C., et al. (2008). MIPAS: An instrument for atmospheric and climate research. *Atmospheric Chemistry and Physics, 8*, 2151–2188. http://dx.doi.org/10.5194/acp-8-2151-2008.

Foucher, P. Y., Chédin, A., Armante, R., et al. (2011). Carbon dioxide atmospheric vertical profiles retrieved from space observation using ACE-FTS solar occultation instrument. *Atmospheric Chemistry and Physics, 11*, 2455–2470. http://dx.doi.org/10.5194/acp-11-2455-2011.

Gambacorta, A., Barnet, C., Wolf, W., et al. (2014). An experiment using high spectral resolution CrIS measurements for atmospheric trace gases: Carbon monoxide retrieval impact study. *IEEE Geoscience and Remote Sensing Letters, 11*, 1639–1643. http://dx.doi.org/10.1109/LGRS.2014.2303641.

George, M., Clerbaux, C., Hurtmans, D., et al. (2009). Carbon monoxide distributions from the IASI/METOP mission: Evaluation with other space-borne remote sensors. *Atmospheric Chemistry and Physics, 9*, 8317–8330. http://dx.doi.org/10.5194/acp-9-8317-2009.

George, M., Clerbaux, C., Bouarar, I., et al. (2015). An examination of the long-term CO records from MOPITT and IASI: Comparison of retrieval methodology. *Atmospheric Measurement Techniques: European Geosciences Union, 8*, 4313–4328.

Ghysels, M., Gomez, L., Cousin, J., et al. (2011). Spectroscopy of CH_4 with a difference-frequency generation laser at 3.3 micron for atmospheric applications. *Applied Physics B, 104*, 989–1000. http://dx.doi.org/10.1007/s00340-011-4665-2.

Goldberg, M. D., Kilcoyne, H., Cikanek, H., et al. (2013). Joint polar satellite system: The United States next generation civilian polar-orbiting environmental satellite system. *Journal of Geophysical Research. Atmospheres, 118*, 13,463–13,475. http://dx.doi.org/10.1002/2013JD020389.

Grieco, G., Masiello, G., Matricardi, M., et al. (2013). Partially scanned interferogram methodology applied to IASI for the retrieval of CO, CO_2, CH_4 and N_2O. *Optics Express, 21*, 24753. http://dx.doi.org/10.1364/OE.21.024753.

Hamazaki, T., Kaneko, Y., Kuze, A., et al. (2005). Fourier transform spectrometer for greenhouse gases observing satellite (GOSAT). In G. J. Komar, J. Wang, & T. Kimura (Eds.) *Enabling Sensor and Platform Technologies for Spaceborne Remote Sensing* (p. p. 73). http://dx.doi.org/10.1117/12.581198.

Hilton, F., Armante, R., August, T., et al. (2012). Hyperspectral earth observation from IASI: Five years of accomplishments. *Bulletin of the American Meteorological Society, 93*, 347–370. http://dx.doi.org/10.1175/BAMS-D-11-00027.1.

Hornik, K., Stinchcombe, M., & White, H. (1989). Multilayer feedforward networks are universal approximators. *Neural Networks, 2*, 359–366. http://dx.doi.org/10.1016/0893-6080(89)90020-8.

Hurtmans, D., Coheur, P.-F., Wespes, C., et al. (2012). FORLI radiative transfer and retrieval code for IASI. *Journal of Quantitative Spectroscopy and Radiative Transfer, 113*, 1391–1408. http://dx.doi.org/10.1016/j.jqsrt.2012.02.036.

Jacquinet-Husson, N., Crepeau, L., Armante, R., et al. (2011). The 2009 edition of the GEISA spectroscopic database. *Journal of Quantitative Spectroscopy and Radiative Transfer, 112*, 2395–2445. http://dx.doi.org/10.1016/j.jqsrt.2011.06.004.

Jacquinet-Husson, N., Armante, R., Scott, N. A., et al. (2016). The 2015 edition of the GEISA spectroscopic database. *Journal of Molecular Spectroscopy, 327*, 31–72. http://dx.doi.org/10.1016/j.jms.2016.06.007.

Joly, L., Parvitte, B., Zeninari, V., et al. (2007). Development of a compact CO_2 sensor open to the atmosphere and based on near-infrared laser technology at 2.68 μm. *Applied Physics B, 86*, 743–748. http://dx.doi.org/10.1007/s00340-006-2568-4.

Karion, A., Sweeney, C., Tans, P., et al. (2010). AirCore: An innovative atmospheric sampling system. *Journal of Atmospheric and Oceanic Technology, 27*, 1839–1853. http://dx.doi.org/10.1175/2010JTECHA1448.1.

Karion, A., Sweeney, C., Pétron, G., et al. (2013). Methane emissions estimate from airborne measurements over a western United States natural gas field. *Geophysical Research Letters, 40*, 4393–4397. http://dx.doi.org/10.1002/grl.50811.

Keith, D. W., Anderson, J. G., Keith, D. W., et al. (2001). Accurate spectrally resolved infrared radiance observation from space: Implications for the detection of decade-to-century–scale climatic change. *Journal of Climate, 14*, 979–990. http://dx.doi.org/10.1175/1520-0442(2001)014<0979:ASRIRO>2.0.CO;2.

Kobayashi, H., Shimota, A., Kondo, K., et al. (1999a). Development and evaluation of the interferometric monitor for greenhouse gases: A high-throughput fourier-transform infrared radiometer for nadir earth observation. *Applied Optics, 38*, 6801–6807.

Kerzenmacher, et al. (2012). Validation of IASI FORLI carbon monoxide retrievals using FTIR data from NDACC. *Atmospheric Measurement Techniques, 5*, 2751–2761. http://dx.doi.org/10.5194/amt-5-2751-2012.

Kobayashi, H., Shimota, A., Yoshigahara, C., et al. (1999b). Satellite-borne high-resolution FTIR for lower atmosphere sounding and its evaluation. *IEEE Transactions on Geoscience and Remote Sensing, 37*, 1496–1507. http://dx.doi.org/10.1109/36.763262.

Kulawik, S. S., Osterman, G., Jones, D. B. A., et al. (2006). Calculation of altitude-dependent tikhonov constraints for TES nadir retrievals. *IEEE Transactions on Geoscience and Remote Sensing, 44*, 1334–1342. http://dx.doi.org/10.1109/TGRS.2006.871206.

Kulawik, S. S., Worden, J. R., Wofsy, S. C., et al. (2013). Comparison of improved aura tropospheric emission spectrometer CO_2 with HIPPO and SGP aircraft profile measurements. *Atmospheric Chemistry and Physics, 13*, 3205–3225. http://dx.doi.org/10.5194/acp-13-3205-2013.

Kuze, A., Suto, H., Nakajima, M., et al. (2009). Thermal and near infrared sensor for carbon observation Fourier-transform spectrometer on the Greenhouse Gases Observing Satellite for greenhouse gases monitoring. *Applied Optics, 48*, 6716. http://dx.doi.org/10.1364/AO.48.006716.

Kuze, A., Suto, H., Shiomi, K., et al. (2012). Level 1 algorithms for TANSO on GOSAT: Processing and on-orbit calibrations. *Atmospheric Measurement Techniques, 5*, 2447–2467. http://dx.doi.org/10.5194/amt-5-2447-2012.

Luitot, C., Boyadjian, J., Buil, C., et al. (2013). Optical architecture of the new generation infrared atmospheric sounder interferometer (IASI-NG). In R. B. Johnson, V. N. Mahajan, & S. Thibault (Eds.)*Proc. SPIE 88410 M.* http://dx.doi.org/10.1117/12.202523. International Society for Optics and Photonics.

Machida, T., Matsueda, H., Sawa, Y., et al. (2008). Worldwide measurements of atmospheric CO_2 and other trace gas species using commercial airlines. *Journal of Atmospheric and Oceanic Technology, 25*, 1744–1754. http://dx.doi.org/10.1175/2008JTECHA1082.1.

Maddy, E. S., & Barnet, C. D. (2008). Vertical resolution estimates in version 5 of AIRS operational retrievals. *IEEE Transactions on Geoscience and Remote Sensing, 46*. http://dx.doi.org/10.1109/TGRS.2008.917498.

Masiello, G., Serio, C., & Antonelli, P. (2012). Inversion for atmospheric thermodynamical parameters of IASI data in the principal components space. *Quarterly Journal of the Royal Meteorological Society, 138*, 103–117. http://dx.doi.org/10.1002/qj.909.

Massart, S., Agusti-Panareda, A., Aben, I., et al. (2014). Assimilation of atmospheric methane products into the MACC-II system: From SCIAMACHY to TANSO and IASI. *Atmospheric Chemistry and Physics, 14*, 6139–6158. http://dx.doi.org/10.5194/acp-14-6139-2014.

Matricardi, M., Chevallier, F., Kelly, G., et al. (2004). An improved general fast radiative transfer model for the assimilation of radiance observations. *Quarterly Journal of the Royal Meteorological Society, 130*, 153–173. http://dx.doi.org/10.1256/qj.02.181.

McMillan, W. W., Barnet, C., Strow, L., et al. (2005). Daily global maps of carbon monoxide from NASA's Atmospheric Infrared Sounder. *Geophysical Research Letters, 32*, L11801. http://dx.doi.org/10.1029/2004GL021821.

McMillin, L. M., Crone, L. J., Goldberg, M. D., et al. (1995). Atmospheric transmittance of an absorbing gas 4 OPTRAN: A computationally fast and accurate transmittance model for absorbing gases with fixed and with variable mixing ratios at variable viewing angles. *Applied Optics, 34*, 6269. http://dx.doi.org/10.1364/AO.34.006269.

Membrive, O., Crevoisier, C., Sweeney, C., et al. (2017). AirCore-HR: A high resolution column sampling to enhance the vertical description of CH_4 and CO_2. *Atmospheric Measurement Techniques Discussions, 5194*, 2016–2236. http://dx.doi.org/10.5194/amt-2016-236.

Moreau, G., Robert, C., Catoire, V., et al. (2005). SPIRALE: A multispecies in situ balloonborne instrument with six tunable diode laser spectrometers. *Applied Optics, 44*, 5972–5989.

Ngo, N. H., Landsheere, X., Pangui, E., et al. (2014). Self-broadening and -shifting of very intense lines of the 1 ← 0 band of 12C16O. *Journal of Quantitative Spectroscopy and Radiative Transfer, 149*, 285–290. http://dx.doi.org/10.1016/j.jqsrt.2014.08.021.

Niro, F., Jucks, K., & Hartmann, J.-M. (2005). Spectra calculations in central and wing regions of CO_2 IR bands. IV: Software and database for the computation of atmospheric spectra. *Journal of Quantitative Spectroscopy and Radiative Transfer, 95*, 469–481. http://dx.doi.org/10.1016/j.jqsrt.2004.11.011.

Oelhaf, H., Clarmann, T. V., Fergg, F., et al. (1991). Remote sensing of trace gases with a balloon borne version of the Michelson interferometer for passive atmospheric sounding (MIPAS). In B. Kaldeich (Ed.)*Proceeeding sof 10th ESA Symposium*. ESA Special Publication.

Perrin, A., Flaud, J.-M., Ridolfi, M., et al. (2016). MIPAS database: New HNO_3 line parameters at 7.6 μm validated with MIPAS satellite measurements. *Atmospheric Measurement Techniques, 9*, 2067–2076. http://dx.doi.org/10.5194/amt-9-2067-2016.

Phillips, D. L. (1962). A technique for the numerical solution of certain integral equations of the first kind. *Journal of the ACM, 9*, 84–97. http://dx.doi.org/10.1145/321105.321114.

Pommier, M., Clerbaux, C., Coheur, P.-F., et al. (2016). HCOOH distributions from IASI for 2008–2014: Comparison with ground-based FTIR measurements and a global chemistry-transport model. *Atmospheric Chemistry and Physics, 16*, 8963–8981. http://dx.doi.org/10.5194/acp-16-8963-2016.

Raspollini, P., Belotti, C., Burgess, A., et al. (2006). MIPAS level 2 operational analysis. *Atmospheric Chemistry and Physics, 6*, 5605–5630.

Razavi, A., Clerbaux, C., Wespes, C., et al. (2009). Characterization of methane retrievals from the IASI space-borne sounder. *Atmospheric Chemistry and Physics, 9*, 7889–7899. http://dx.doi.org/10.5194/acp-9-7889-2009.

Razavi, A., Karagulian, F., Clarisse, L., et al. (2011). Global distributions of methanol and formic acid retrieved for the first time from the IASI/MetOp thermal infrared sounder. *Atmospheric Chemistry and Physics, 11*, 857–872. http://dx.doi.org/10.5194/acp-11-857-2011.

Rodgers, C. D. (2000). *Inverse methods for atmospheric sounding*. Singapore: World Scientific. http://dx.doi.org/10.1142/3171.

Rothman, L. S., Gordon, I. E., Barbe, A., et al. (2009). The HITRAN 2008 molecular spectroscopic database. *Journal of Quantitative Spectroscopy and Radiative Transfer, 110*, 533–572. http://dx.doi.org/10.1016/j.jqsrt.2009.02.013.

Rothman, L. S., Gordon, I. E., Babikov, Y., et al. (2013). The HITRAN2012 molecular spectroscopic database. *Journal of Quantitative Spectroscopy & Radiative Transfer, 130*, 4–50. http://dx.doi.org/10.1016/j.jqsrt.2013.07.002.

Rumelhart, D. E., & McClelland, J. L. (1986). *Parallel distributed processing: Explorations in the microstructure of cognition: Foundations* (vol. 1). Cambridge, MA: MIT Press.

Saitoh, N., Imasu, R., Ota, Y., et al. (2009). CO_2 retrieval algorithm for the thermal infrared spectra of the Greenhouse Gases Observing Satellite: Potential of retrieving CO_2 vertical profile from high-resolution FTS sensor. *Journal of Geophysical Research, 114*, D17305. http://dx.doi.org/10.1029/2008JD011500.

Saitoh, N., Kimoto, S., Sugimura, R., et al. (2016). Algorithm update of the GOSAT/TANSO-FTS thermal infrared CO_2 product (version 1) and validation of the UTLS CO_2 data using CONTRAIL measurements. *Atmospheric Measurement Techniques, 9*, 2119–2134. http://dx.doi.org/10.5194/amt-9-2119-2016.

Schmidt, U., & Khedim, A. (1991). In situ measurements of carbon dioxide in the winter Arctic vortex and at midlatitudes: An indicator of the 'age' of stratopheric air. *Geophysical Research Letters, 18*, 763–766. http://dx.doi.org/10.1029/91GL00022.

Schuck, T. J., Brenninkmeijer, C. A. M., Slemr, F., et al. (2009). Greenhouse gas analysis of air samples collected onboard the CARIBIC passenger aircraft. *Atmospheric Measurement Techniques, 2*, 449–464. http://dx.doi.org/10.5194/amt-2-449-2009.

Scott, N. A. (1974). A direct method of computation of the transmission function of an inhomogeneous gaseous medium—I: Description of the method. *Journal of Quantitative Spectroscopy and Radiative Transfer, 14*, 691–704. http://dx.doi.org/10.1016/0022-4073(74)90116-2.

Scott, N. A., & Chédin, A. (1981). A fast line-by-line method for atmospheric absorption computations: The automatized atmospheric absorption atlas. *Journal of Applied Meteorology, 20*, 802–812. http://dx.doi.org/10.1175/1520-0450(1981)020<0802:AFLBLM>2.0.CO;2.

Shephard, M. W., Cady-Pereira, K. E., Luo, M., et al. (2011). TES ammonia retrieval strategy and global observations of the spatial and seasonal variability of ammonia. *Atmospheric Chemistry and Physics, 11*, 10743–10763. http://dx.doi.org/10.5194/acp-11-10743-2011.

Shephard, M. W., McLinden, C. A., Cady-Pereira, K. E., et al. (2015). Tropospheric emission spectrometer (TES) satellite observations of ammonia, methanol, formic acid, and carbon monoxide over the Canadian oil sands: Validation and model evaluation. *Atmospheric Measurement Techniques, 8*, 5189–5211. http://dx.doi.org/10.5194/amt-8-5189-2015.

Smith, W. L., Woolf, H. M., & Revercomb, H. E. (1991). Linear simultaneous solution for temperature and absorbing constituent profiles from radiance spectra. *Applied Optics, 30*, 1117. http://dx.doi.org/10.1364/AO.30.001117.

Stiller, G. P. (2001). *The karlsruhe optimized and precise radiative transfer algorithm (KOPRA), FZKA 6487*. Forsch: Karlsruhe University. Technical report.

Strow, L. L., & Reuter, D. (1988). Effect of line mixing on atmospheric brightness temperatures near 15 micron. *Applied Optics, 27*, 872–878. http://dx.doi.org/10.1364/AO.27.000872.

Strow, L. L., Hannon, S. E., De Souza-Machado, S., et al. (2003). An overview of the AIRS radiative transfer model. *IEEE Transactions on Geoscience and Remote Sensing, 41*. http://dx.doi.org/10.1109/TGRS.2002.808244.

Sweeney, C., Karion, A., Wolter, S., et al. (2015). Seasonal climatology of CO_2 across North America from aircraft measurements in the NOAA/ESRL Global Greenhouse Gas Reference Network. *Journal of Geophysical Research. Atmospheres, 120*, 5155–5190. http://dx.doi.org/10.1002/2014JD022591.

Té, Y., Jeseck, P., Camy-Peyret, C., Payan, S., et al. (2002). Balloonborne calibrated spectroradiometer for atmospheric nadir sounding. *Applied Optics, 41*, 6431–6441.

Tennyson, J., Bernath, P. F., Campargue, A., et al. (2014). Recommended isolated-line profile for representing high-resolution spectroscopic transitions (IUPAC Technical Report). *Atmospheric Measurement Techniques, 86*, 1931–1943. http://dx.doi.org/10.1515/pac-2014-0208.

Thonat, T., Crevoisier, C., Scott, N. A., et al. (2012). Retrieval of tropospheric CO column from hyperspectral infrared sounders—application to four years of Aqua/AIRS and MetOp-A/IASI. *Atmospheric Measurement Techniques, 5*, 2413–2429. http://dx.doi.org/10.5194/amt-5-2413-2012.

Tikhonov, A. N. (1963). Solution of incorrectly formulated problems and the regularization method. *Soviet Mathematics—Doklady, 4*, 1035–1038.

Tjemkes, S. (2016). Mtg-irs: The instrument, its products and current user readiness activities. In *Light, energy and the environment* (p. JTu1A.2). Washington, D.C: OSA. http://dx.doi.org/10.1364/FTS.2016.JTu1A.2.

Tran, H., Flaud, P.-M., Gabard, T., et al. (2006). Model, software and database for line-mixing effects in the ν_3 and ν_4 bands of CH_4 and tests using laboratory and planetary measurements—I: N2 (and air) broadenings and the earth atmosphere. *Journal of Quantitative Spectroscopy and Radiative Transfer, 101*, 284–305. http://dx.doi.org/10.1016/j.jqsrt.2005.11.020.

Tran, H., Ngo, N. H., & Hartmann, J.-M. (2013). Efficient computation of some speed-dependent isolated line profiles. *Journal of Quantitative Spectroscopy and Radiative Transfer, 129*, 199–203. http://dx.doi.org/10.1016/j.jqsrt.2013.06.015.

von Clarmann, T., Grabowski, U., & Kiefer, M. (2001). On the role of non-random errors in inverse problems in radiative transfer and other applications. *Journal of Quantitative Spectroscopy and Radiative Transfer, 71*, 39–46. http://dx.doi.org/10.1016/S0022-4073(01)00010-3.

Wetzel, G., Fischer, H., & Oelhaf, H. (1995). Remote sensing of trace gases in the midinfrared spectral region from a nadir view. *Applied Optics, 34*, 467. http://dx.doi.org/10.1364/AO.34.000467.

Wofsy, S. C. (2011). HIAPER pole-to-pole observations (HIPPO): Fine-grained, global-scale measurements of climatically important atmospheric gases and aerosols. *Philosophical Transactions of the Royal Society of London A: Mathematical, Physical and Engineering Sciences, 369*.

Worden, H., Beer, R., & Rinsland, C. P. (1997). Airborne infrared spectroscopy of 1994 western wildfires. *Journal of Geophysical Research. Atmospheres, 102*, 1287–1299. http://dx.doi.org/10.1029/96JD02982.

Worden, H. M., Logan, J. A., Worden, J. R., et al. (2007). Comparisons of tropospheric emission spectrometer (TES) ozone profiles to ozonesondes: Methods and initial results. *Journal of Geophysical Research, 112*, D03309. http://dx.doi.org/10.1029/2006JD007258.

Wright, R., Carn, S. A., & Flynn, L. P. (2005). A satellite chronology of the May–June 2003 eruption of Anatahan volcano. *Journal of Volcanology and Geothermal Research, 146*, 102–116. http://dx.doi.org/10.1016/j.jvolgeores.2004.10.021.

Xiong, X., Barnet, C., Maddy, E., et al. (2008). Characterization and validation of methane products from the atmospheric infrared sounder (AIRS). *Journal of Geophysical Research, 113*, G00A01. http://dx.doi.org/10.1029/2007JG000500.

Xiong, X., Barnet, C., Maddy, E. S., et al. (2013). Mid-upper tropospheric methane retrieval from IASI and its validation. *Atmospheric Measurement Techniques, 6*, 2255–2265. http://dx.doi.org/10.5194/amt-6-2255-2013.

Yokota, T., Yoshida, Y., & Eguchi, N. (2009). Global concentrations of CO_2 and CH_4 retrieved from GOSAT: First preliminary results. *Sola, 5*, 160–163. http://dx.doi.org/10.2151/sola.2009041.

Zhang, H. F., Chen, B. Z., Machida, T., et al. (2014). Estimating Asian terrestrial carbon fluxes from CONTRAIL aircraft and surface CO_2 observations for the period 2006–2010. *Atmospheric Chemistry and Physics, 14*, 5807–5824. http://dx.doi.org/10.5194/acp-14-5807-2014.

Further Reading

Clerbaux, C., George, M., Turquety, S., et al. (2008). CO measurements from the ACE-FTS satellite instrument: Data analysis and validation using ground-based, airborne and spaceborne observations. *Atmospheric Chemistry and Physics, 8*, 2569–2594.